

1993

Remote robot manipulator coupled with remote-controlled guide vehicle for soil sampling in hazardous waste sites

Kiho Kim

Iowa State University

Follow this and additional works at: <https://lib.dr.iastate.edu/rtd>

 Part of the [Civil and Environmental Engineering Commons](#), and the [Mechanical Engineering Commons](#)

Recommended Citation

Kim, Kiho, "Remote robot manipulator coupled with remote-controlled guide vehicle for soil sampling in hazardous waste sites " (1993). *Retrospective Theses and Dissertations*. 10463.
<https://lib.dr.iastate.edu/rtd/10463>

This Dissertation is brought to you for free and open access by the Iowa State University Capstones, Theses and Dissertations at Iowa State University Digital Repository. It has been accepted for inclusion in Retrospective Theses and Dissertations by an authorized administrator of Iowa State University Digital Repository. For more information, please contact digirep@iastate.edu.

INFORMATION TO USERS

This manuscript has been reproduced from the microfilm master. UMI films the text directly from the original or copy submitted. Thus, some thesis and dissertation copies are in typewriter face, while others may be from any type of computer printer.

The quality of this reproduction is dependent upon the quality of the copy submitted. Broken or indistinct print, colored or poor quality illustrations and photographs, print bleedthrough, substandard margins, and improper alignment can adversely affect reproduction.

In the unlikely event that the author did not send UMI a complete manuscript and there are missing pages, these will be noted. Also, if unauthorized copyright material had to be removed, a note will indicate the deletion.

Oversize materials (e.g., maps, drawings, charts) are reproduced by sectioning the original, beginning at the upper left-hand corner and continuing from left to right in equal sections with small overlaps. Each original is also photographed in one exposure and is included in reduced form at the back of the book.

Photographs included in the original manuscript have been reproduced xerographically in this copy. Higher quality 6" x 9" black and white photographic prints are available for any photographs or illustrations appearing in this copy for an additional charge. Contact UMI directly to order.

U·M·I

University Microfilms International
A Bell & Howell Information Company
300 North Zeeb Road, Ann Arbor, MI 48106-1346 USA
313/761-4700 800/521-0600

Order Number 9321180

**Remote robot manipulator coupled with remote-controlled guide
vehicle for soil sampling in hazardous waste sites**

Kim, Kiho, Ph.D.

Iowa State University, 1993

Copyright ©1993 by Kim, Kiho. All rights reserved.

U·M·I

**300 N. Zeeb Rd.
Ann Arbor, MI 48106**

**Remote robot manipulator coupled with remote-controlled guide vehicle
for soil sampling in hazardous waste sites**

by

Kiho Kim

A Dissertation Submitted to the
Graduate Faculty in Partial Fulfillment of the
Requirements for the Degree of
DOCTOR OF PHILOSOPHY

Department: Mechanical Engineering
Major: Mechanical Engineering

Approved:

Signature was redacted for privacy.

In Charge of Major Work

Signature was redacted for privacy.

For the Major Department

Signature was redacted for privacy.

For the Graduate College

Iowa State University
Ames, Iowa
1993

Copyright © Kiho Kim, 1993. All rights reserved.

TABLE OF CONTENTS

ACKNOWLEDGMENTS	ix
1. INTRODUCTION	1
2 LITERATURE REVIEW	5
2.1 Robotic applications in hazardous environment	5
2.2 Non-linearities in robot manipulator	6
2.3 Friction modeling and compensation	7
2.4 Mechanical components of non-direct drive manipulator	12
3. DESIGN OF GUIDE VEHICLE	14
3.1 Overview of robotic surface sampling system	14
3.2 Design considerations and specifications	15
3.3 Configuration of guide vehicle	17
4. REMOTE CONTROL OF GUIDE VEHICLE	21
4.1 Teleoperated control system	21
4.1.1 Mechanism	22
4.1.2 System integration	24
4.1.3 Selection of linear actuator	24
4.2 Radio control system	26
4.2.1 Servo mechanism	26
4.2.2 System integration	27

4.3 Field test	31
5. REMOTE ROBOT MANIPULATOR	32
5.1 Problems associated with sampling tasks	32
5.2 Overview of remote manipulator	33
5.3 Kinematics of remote manipulator	36
5.3.1 Coordinate frame assignment	37
5.3.2 Forward kinematics	37
5.3.3 Inverse kinematics	41
5.3.4 Manipulator Jacobian matrix	43
6. DYNAMICS OF REMOTE ROBOT MANIPULATOR	45
6.1 Dynamics of manipulator	45
6.2 Motor dynamics	47
6.3 Dynamics of actuator-transmission-load system	49
6.3.1 Actuator-transmission-load system	49
6.3.2 Dynamic model with friction	52
6.3.3 Integrated dynamic model	54
7. PARAMETER IDENTIFICATION OF MANIPULATOR DYNAMICS	55
7.1 Experimental description	55
7.1.1 Experimental setup	55
7.1.2 Experimental procedures	56
7.2 Experimental results	58
7.3 Mathematical model for identification	62
7.4 Identification results	66
8. MOBILE ROBOTIC SAMPLING SYSTEM	68
8.1 Design considerations and specifications	68

8.2 Mechanical structure	70
8.2.1 Robotic arm on remote-controlled guide vehicle	70
8.2.2 Sampling tool and soil recovery fixture	75
8.3 Analysis of robotic arm on remote-controlled guide vehicle	75
8.3.1 Coordinate frame assignment	75
8.3.2 Forward kinematics	75
8.3.3 Inverse kinematics	79
8.3.4 Jacobians	80
8.3.5 Dynamics	80
8.4 Integrated dynamic model	81
8.4.1 Dynamics of actuator-transmission-load system	81
8.4.2 Integrated dynamics	83
8.5 Summary	83
9. CONCLUSIONS AND FUTURE WORK	84
9.1 Conclusions	84
9.2 Recommendations for future work	86
BIBLIOGRAPHY	88
APPENDIX A. KINEMATIC DESCRIPTION OF MANIPULATOR	93
APPENDIX B. DERIVATION OF DYNAMIC MODEL BASED ON NEWTON-EULER FORMULATION	98
B.1 Recursive Newton-Euler formulation	98
B.2 Dynamic model of remote manipulator	101
APPENDIX C. DERIVATION OF DYNAMIC MODEL BASED ON LAGRANGIAN FORMULATION	105
APPENDIX D. DESCRIPTION OF HARDWARE	109

D.1 Remote-controlled guide vehicle	109
D.2 Remote manipulator located on trailer	112
APPENDIX E. ROBOTIC ARM ON GUIDE VEHICLE	114
E.1 Motion axis	115
E.2 Mechanical components for motion assembly	117

LIST OF TABLES

Table 5.1: D-H parameters for the manipulator located on the trailer	39
Table 7.1: Friction and gravity torque parameters for the manipulator located on the trailer	67
Table 8.1: D-H parameters for the manipulator on the guide vehicle	78
Table D.1: Linear actuator specifications for the guide vehicle	109
Table D.2: Servo specifications for the guide vehicle	110
Table D.3: Motor specifications for the manipulator located on the trailer	113
Table E.1: List of mechanical components for the manipulator on the guide vehicle	118

LIST OF FIGURES

Figure 2.1: Characteristic curves of non-linearities	6
Figure 2.2: Characteristics of various types of friction	8
Figure 3.1: Robotic surface sampling system with the remote-controlled guide vehicle	16
Figure 3.2: Schematic representation of the remote-controlled guide vehicle coupled with the remote manipulator located on the trailer	16
Figure 3.3: Four-wheeled guide vehicle	18
Figure 3.4: Configuration of the guide vehicle	20
Figure 4.1: Mechanism to be controlled with linear actuator	23
Figure 4.2: Block diagram of the teleoperated control system	25
Figure 4.3: Schematic of servo mechanism for the radio control system	28
Figure 4.4: Control mechanism mounted on the guide vehicle	29
Figure 4.5: Block diagram of the radio control system	30
Figure 5.1: Remote manipulator located on the trailer	34
Figure 5.2: Workspace of the manipulator located on the trailer	35
Figure 5.3: Schematic of the three DOF manipulator located on the trailer	38
Figure 5.4: Link coordinate frame assignments of the manipulator located on the trailer	39
Figure 6.1: Armature circuit model of a dc servomotor	48
Figure 6.2: Schematic of actuator-transmission-load for link 1	50
Figure 6.3: Schematic of motor-harmonic drive joint $i, (i = 2, 3)$	52

Figure 7.1: Schematic of measurement system for the three DOF manipulator located on the trailer	57
Figure 7.2: Steady state velocity vs. input voltage for joint of forearm	59
Figure 7.3: Steady state velocity vs. input voltage for joint of upper arm	60
Figure 7.4: Steady state velocity vs. input voltage for joint of shoulder	61
Figure 7.5: Block diagram of system model for parameter identification	63
Figure 8.1: Manipulator on the guide vehicle	71
Figure 8.2: Workspace of the manipulator on the guide vehicle	73
Figure 8.3: Major mechanical components of the manipulator on the guide vehicle	74
Figure 8.4: Sampling tool and soil recovery fixture	76
Figure 8.5: Schematic of the three DOF manipulator on the guide vehicle	77
Figure 8.6: Link coordinate frame assignments of the manipulator on the guide vehicle	77
Figure A.1: Numbering of links and joints for n – link manipulator	94
Figure A.2: Link parameters and coordinate frames for link with revolute joints	95
Figure B.1: Schematic of the remote manipulator located on the trailer	102
Figure D.1: Circuit diagram of controlling a motor of linear actuator	111
Figure D.2: Schematic of links of the manipulator located on the trailer	112
Figure E.1: Horizontal axis of the manipulator on the guide vehicle	115
Figure E.2: Vertical and rotational axes of the manipulator on the guide vehicle	116
Figure E.3: Mechanical components for motion assembly of the manipulator on the guide vehicle	117

ACKNOWLEDGMENTS

I wish to express my gratitude to Dr. Jerry Hall for his valuable guidance throughout my graduate studies. I would like to particularly thank him for his constant encouragement and support. It was a privilege to work with him.

I wish to thank Dr. Patrick Kavanagh for his suggestions and discussions in the area of robotics. I also wish to thank Dr. Donald Flugrad, Dr. Edwin Jones, Dr. Palaniappa Molian, and Dr. Loren Zachary, who served on my doctoral committee and reviewed the dissertation.

I would like to thank my fellow graduate student, Reza Bashirzadeh for his friendship and encouragement. I also wish to thank Mrs. Nancy Hall for her encouragement and kindness.

Equipment donated by the John Deere Corporation, Motion Systems Corporation and J. L. Hall Engineering was used toward completion of the remote-controlled guide vehicle and is gratefully acknowledged. The assistantship and facilities provided by Engel Laboratory and Mechanical Engineering Department as well as the assistantship support of the Power Affiliate Program were very much appreciated.

I would like to dedicate this work to my parents for their support, sacrifice, and dreams. Finally, I owe more than I can say to my wife, Yeonseon, who has lovingly supported and encouraged me in many way through both the joys and frustrations of our time in Ames, Iowa, and provided more than her share of the care and nurture of our lovely daughter, Nyeon.

1. INTRODUCTION

The concern for environmental safety has been significantly increased in recent years. At the present time there are 1,189 hazardous sites that are on the Superfund list of the U.S. Environmental Protection Agency [1]. This is a list of hazardous waste sites with a high priority for remediation. Cleanup of these hazardous waste sites is an expensive and time consuming process with existing methods. The important initial step is contaminant analysis because cleanup operations can not begin until contaminants in the soil have been clearly identified. Currently, a sample of soil is retrieved either by human or mechanical means, and the sample is stored until it can be analyzed in the laboratory. Based on the efforts required for the remediation of thirteen of the 1,777 uncontrolled sites, the Office of Technology Assessment (OTA) has estimated it will take 50 years and \$300 billion to complete the cleanup operations on approximately 28,000 hazardous waste sites identified in the United States [2]. The figures may be underestimated because the complete assessment of the problem is not yet made. However, the cost for cleanup of all the hazardous waste sites in the United States is estimated to be billions of dollars.

A remote sampling technique was developed in the Ames Laboratory at Iowa State University (ISU), one of the U.S. Department of Energy (DOE) sites, by using a Laser Ablation-Inductively Coupled Plasma-Atomic Emission Spectrometry (LA-ICP-AES) [3]. A sampling analysis system that will provide a real-time soil analysis in situ was also developed to go into a contaminated field to collect the soil samples with the aid of a laser. The

sampling analysis system was comprised of a truck carrying the necessary soil analysis equipment, and a trailer carrying a robot with the necessary sampling equipment.

Sampling an area in a field, however, is limited because the trailer carrying the robotic sampling device is pulled and guided only by the truck. The sampling process required at different locations might not be suitable due to the inaccessibility of the truck. Hence, it was necessary to develop a lighter and more agile guide vehicle to pull the trailer into the desired sampling location, leaving the truck at the protected area. In addition, the development of the guide vehicle requires a remote control means for operation to remove the human from the hostile working environment. An additional need was to place a light weight robotic sampler on the guide vehicle so that a sample could be retrieved by the guide vehicle without having to pull the trailer with the heavy robotic sampler into a sampling site.

The manipulator [4] located on the trailer was designed to position the soil sampler (end effector) to the sampling spot specified by the operator and to make an ablation cell (tool) mounted on the end of the soil sampler be properly sealed from the surroundings. Soil sampling in situ takes place in an argon gas environment with the aid of laser ablation. The soil is ablated by a laser transmitted through an optical fiber mounted on the soil sampler. The ablated soil samples are then transported through the transfer tube in the argon gas environment to ICP-AES [5] for contaminant analysis. In this process, the manipulator is required to perform complex tasks involving both the ablation cell positioning, and compliant contact between the ablation cell and the soil to be sampled. These problems must be solved to successfully accomplish the sampling task in face of the uncertainties of the remote and unstructured sampling environment. Thus, the development of an adequate dynamic model for the manipulator is necessary to control the compliant motion of the manipulator. In addition, the analysis of the dynamic characteristics of the manipulator is necessary for simulating and controlling, as well as evaluating and improving its performance.

This research focuses on the design and construction of the remote-controlled guide vehicle [6,7], the development of the integrated dynamic model of the trailer mounted remote manipulator, and the design and analysis of a mobile robotic sampling system placed on the guide vehicle. The major objectives of this research are:

1. To design and construct a remote-controlled guide vehicle capable of carrying a robotic sampling unit for soil sampling, or pulling a trailer carrying a remote manipulator into a contaminated field to obtain the soil samples at desired locations.
2. To design and analyze a robotic arm, a sampling tool, and a soil recovery fixture for a mobile robotic sampling system to be mounted on the remote-controlled guide vehicle.
3. To develop an integrated dynamic model for the trailer mounted remote manipulator and its drive system so that modeling error can be minimized.
4. To develop an identification method of determining dynamic parameters in the integrated dynamic model.

This dissertation is organized as follows: Chapter 2 presents a literature review on robotic applications in hazardous environments, mechanical components of non-direct drive robot manipulators, and non-linearities, friction modeling and friction compensation of robot manipulator joints. Chapter 3 presents the design and construction of the guide vehicle and the overview of the robotic sampling system. Chapter 4 presents the vehicle's remote control system including teleoperation and radio control. Selection of linear actuators for the drive brake, transmission, throttle and steering linkages is given based on experimental results. In addition, field test results of the remote-controlled vehicle are provided. Chapter 5 presents the overall structure and kinematics of the trailer mounted remote manipulator. Problems associated with the sampling task of the manipulator in a hazardous waste site are briefly discussed. The closed form solutions for the forward kinematics and inverse kinematics of the manipulator are provided. The Jacobians of the manipulator are also provided. Chapter 6

presents the dynamic model of the sampling manipulator. Closed form dynamic equations of motion are derived by both the Newton-Euler method and the Lagrangian method. The motor dynamics are also derived and included in the model. Finally, the integrated dynamic model for the manipulator and its drive system is developed for a controller design. Chapter 7 presents the identification method of dynamic parameters for the integrated dynamic equations of motion of the manipulator developed in Chapter 6. The velocity-dependent friction coefficients, and gravity effect on torque are identified based on experimental results. Chapter 8 presents the design of a robotic arm, a sampling tool, a soil recovery fixture for a mobile robotic sampling system to be mounted on the guide vehicle. The kinematic and dynamic analyses of the robotic arm are also provided. Finally, Chapter 9 gives the conclusions of this study and includes recommendations for future work.

2. LITERATURE REVIEW

2.1 Robotic applications in hazardous environment

Use of robots has been extended to hostile environments unfit for human habitation such as those with nuclear and space applications. In particular, robotic applications have been significantly promoted in the area of automated hazardous waste handling to eliminate human operations in hazardous environments. The primary rationale for using robots is to eliminate or significantly reduce human exposure to hazardous environments.

A vehicle manufactured by 21st Century Robotics Incorporation (WASP) with a six DOF manipulator coupled to a Kelly spray/vacuum decontamination system is being developed to remotely decontaminate the alpha-contaminated process room at the DOE's Savannah River Site (SRS) [8]. A teleoperated vehicle with a five DOF manipulator was used to relocate a 55-curie cesium source which was located in a well at SRS [9]. This mobile teleoperator (OAO-150) was made by the OAO Corporation and operated by either radio control or tether cable. Video surveillance in sand filters and inspection to locate cave-ins of the gravel and sand layers can be performed by a commercially available radio controlled vehicle. The contaminated soil surrounding waste storage tanks can be removed by a radio controlled vehicle (BOBCAT) originally used to excavate soil. This vehicle is controlled by joysticks. Several teleoperated robots have been developed for use in emergency situations at SRS.

A remote manipulator [10] utilizing a master/slave controller was used in the area of the electrical distribution line maintenance. The robot was used to trim branches of trees near

live electrical lines so that no one would be exposed to this danger. The system had a six DOF manipulator to cut trees and a three DOF aerial device to lift the manipulator. A ten DOF master/slave telerobotic manipulator [11] with a three DOF end effector was developed for use in the hazardous environments .

2.2 Non-linearities in robot manipulator

Existence of non-linearities in the robot control system degrades system performance and makes the design of control laws difficult. Such unavoidable non-linearities include friction, backlash, deadband (dead zone), and saturation. Effects of these non-linearities are illustrated in Figure 2.1. The friction effect is described in next section.

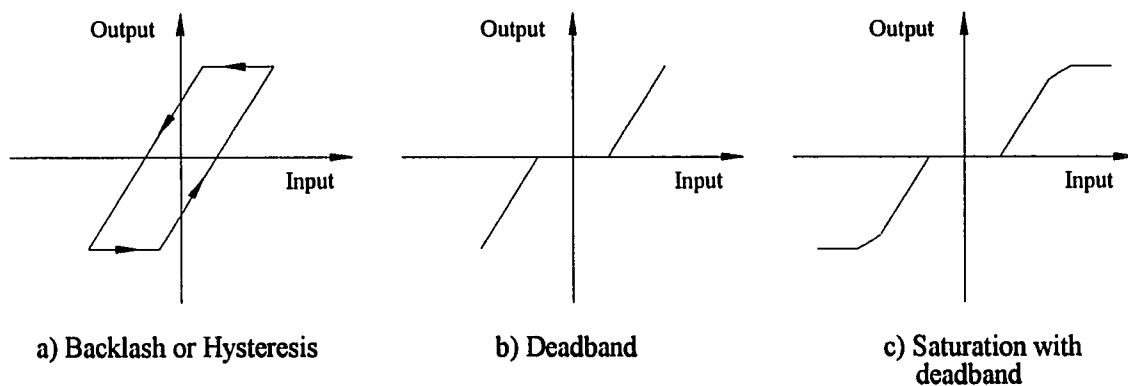


Figure 2.1: Characteristic curves of non-linearities

Backlash occurs from imperfectly meshed gearing. Backlash is the angular free motion in both the clockwise and the counterclockwise direction of the output shaft when the input shaft is held stationary. Figure 2.1(a) shows the input-output characteristic of backlash. Backlash is considered as mechanical deadband caused by slip in connection between two mechanical

members such as belt drives, gears, keyways, screws, and couplers. It can cause discontinuities in velocity and acceleration of motion.

Deadband is described as a small range of input variations near zero to which the motor output is insensitive due to static friction. As is shown in Figure 2.1 (b), the deadband width is defined as the amount of voltage required to move the motor initially at rest. Deadband causes positional inaccuracy, and poor stability at low velocities.

For any servomechanism, the output is linearly proportional to the input over a small range of the input signal. As the input signal increases, the output may no longer increase in proportion to the input. When the output reaches a constant value with a further increase of the input, the phenomenon is called saturation. This is shown in Figure 2.1 (c) and exists in electromechanical systems, hydraulic systems, and pneumatic systems.

2.3 Friction modeling and compensation

All mechanisms are affected by friction forces due to sliding, rolling, and rubbing of various mechanical parts. Most non-direct drive manipulator joints in use today constitute gears, screws, harmonic drives, bearings and electrical motors which experience friction during operation. About 25% of motor torque is needed to overcome the joint frictional force [12]. In manipulator mechanisms friction forces are a combination of static friction, viscous friction, coulomb friction (dry friction), static friction (stiction) shown in Figure 2.2. Static friction is the force which must be overcome to start motion at rest (Figure 2.2 (a)). Viscous friction is linearly proportional to the angular velocity (Figure 2.2 (b)). Coulomb friction is independent of the velocity and has a constant amplitude (Figure 2.2 (c)). It acts opposite to the direction of motion. A combination of viscous friction, Coulomb friction, and stiction is shown in Figure 2.2 (d). The friction force, which is a complex non-linear phenomenon, is the major source of internal disturbances occurring in the manipulator joints. The presence of

non-linear friction in a D. C. motor driven robot arm may generate serious problems during operation by the degradation of positional accuracy, performance and robot life. From the viewpoint of robot control, it may create a steady-state error, undesired oscillation and tracking lags, and make the design of control law difficult. Modeling of friction is important in developing the dynamic equations to describe the manipulator as accurately as possible. Appropriate friction modeling is of particular importance in developing the dynamic equations to describe the manipulator and in improving robot performance.

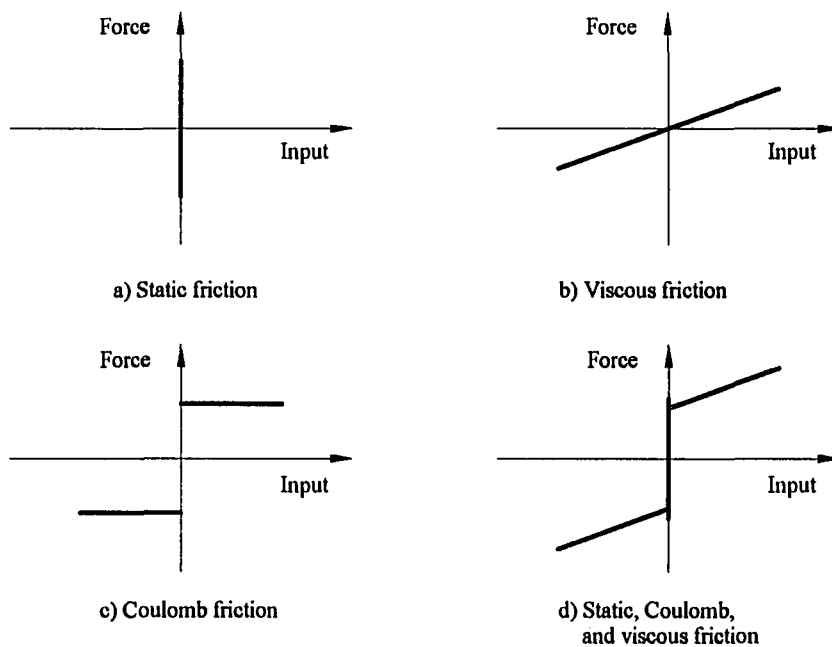


Figure 2.2: Characteristics of various types of friction

A number of researchers have developed models of friction forces in DC. motor driven robot arms. A combined friction model for static, Coulomb, and viscous friction was developed based on experimental results with joints of a two degree of freedom manipulator [13]. The experiments were performed on a quasi-rigid arm with a harmonic drive.

Measurements included the rotor angular velocity, the load angular position, the load output torque, and the load angular velocity. The friction model was expressed as a function of angular position (sinusoidal function) and velocity (polynomial equation). A velocity dependent Coulomb friction model was used to compensate for the non-linear friction. The result showed the dependence of the step response on the magnitude of the reference input. They suggested using a variable viscous friction model for the discrete time implementation for gain scheduling control. They presented the significance of velocity dependent friction to position dependent friction.

The phenomenon of stick-slip motion occurring at low velocities plays an important role in a manipulator's precise position and force control. Stick-slip behavior was examined by Armstrong-Helouvry [14] considering Stribeck friction through dimensional analysis. They investigated the minimum velocity for stick-slip during the stick-slip motion. In their consecutive work [15], Coulomb friction was considered along with viscous friction and Stribeck friction (non-linear, low velocity friction) with frictional lag in the friction model. They investigated stick-slip behavior through dimensional and perturbation analysis techniques. They noted that the onset of stick-slip motion can be predicted through perturbation analysis. They also demonstrated the reduction of input parameters to four in accurately modeling the nonlinear system through dimensional analysis. Theoretical results were verified through experiments conducted on a PUMA robot.

Little research has been done on the effect of coulomb friction near zero velocity. This has been referred to as the stick-slip phenomenon which makes the precise position and force control difficult and leads to overshoot and limit cycling. In Dupont's model [16] the Coulomb type friction force was expressed as a function of joint position, velocity and acceleration. Incorporation of this model in robot dynamic equations causes instability due to discontinuities in the highest derivative terms (acceleration). In addition, Dupont addressed

the implicitness of the forward governing equation of the manipulator caused by the load-dependent friction and the difficulty of obtaining the forward dynamic solutions of the robot arm in simulation. As a special case for load-dependent friction, he showed the explicitness of a forward dynamic equation for a screw driven manipulator with a combined model of static and Coulomb friction. For control he suggested the use of an appropriate friction model which describes the friction characteristics of a particular manipulator as closely as possible.

The importance of position feedback for anti-stick-slip behavior was stressed by Dupont [17] because of the better accuracy of position data compared with that of the velocity data. He used the state variable friction model developed for rock friction to avoid stick-slip phenomenon at low velocities. He reported that the state variable friction laws including the transient friction effects can be used to achieve the steady, low velocity motion through position feedback control.

An investigation was given to the existence and uniqueness of the forward solution of the rigid body dynamic equations combined with Coulomb friction. Rajan et al. [18] considered the dynamics of a rigid two-dimensional body in frictional contact with rigid walls in the context of the peg-in-hole problem. Multiplicity of the dynamic solution was discussed. The inconsistency of the solution for a slender rigid rod with Coulomb friction sliding along a horizontal surface was considered by Mason and Wang [19]. They derived the conditions under which an inconsistent solution arises. Dupont [20] reported the possibility of uniqueness and an existence problem in the forward dynamic equations even for a single degree of freedom system. He also derived the necessary and sufficient condition for existence and uniqueness of the forward dynamic solution and presented this condition for a screw transmission drive used in the manipulator's joint drive mechanism.

For velocities above a minimum critical value, a combined friction model of viscous and Coulomb friction was developed by Armstrong [21]. This was based on experimental data for

a joint on a PUMA 560 manipulator. His experiment for measuring friction included acceleration measurement using a rotational accelerometer, off-line velocity estimation based on position and torque data, and break-away torque measurement. He reported friction repeatability and position dependent friction. He also presented negative velocity dependent friction (negative viscous damping) at low velocities, which is significant for force control. He suggested that a friction correction table constructed from the breakaway torque experiment be used to compensate the position dependent friction without feedback correction.

Kubo et al. [22] developed a combined friction model of static, viscous and Coulomb friction based on the experimental data such as the steady state velocity to the input voltage applied. The experiment was performed for one joint of a Toshiba TSR-500V robot with a harmonic drive gear. They showed the dependence of the system step response and stability on the magnitude of the reference input. In their friction model, the value of static friction was considered to be the same value as the Coulomb friction. Coulomb friction compensation was used to linearize the system and implement a digital tracking controller.

The effect of Coulomb friction in a harmonic drive and bearing, which are the major joint components of non-direct drive manipulator arms, was qualitatively investigated by Gogoussis and Donath [23]. By introducing the mechanical efficiency of the gear they developed a Coulomb friction model in the harmonic drive gear which is applicable for forward and back drive operation. In addition, a Coulomb friction model for bearings was expressed as a function of net force and moment components at a joint depending on the type of bearings including radially-loaded revolute bearings, axially-loaded revolute bearings and prismatic bearings. Their analytical result showed that Coulomb friction is dependent on the joint interaction. They suggested the rearrangement of manipulator dynamics with a friction term for the solution to the inverse and forward dynamics.

The effect of Coulomb friction and stiction on force control was investigated analytically by Townsend [24] through dimensional analysis and simulation. The sinusoidal-input-describing function technique was used to examine the system instabilities and limit cycles. He reported the dependence of stability on the input magnitude due to Coulomb friction. He also presented that Coulomb friction leads to slow system response caused by the time delay and possibly causes limit cycling during slow motion when the steady state error approaches zero.

Gogoussis and Donath [25] qualitatively investigated Coulomb friction effects in the performance of manipulator mechanism and dealt with the robot mechanism design issues with a recognition of Coulomb friction. They illustrated that Coulomb friction is highly dependent on the location of load bearing supports. They also identified that Coulomb friction can lead to limit cycling due to elastic effects in motion of the robotic arm with gears or harmonic drives, and results in the critical positional error of step response which can not be remedied by linear feedback control.

2.4 Mechanical components of non-direct drive manipulator

Harmonic drive gears are commonly used transmission elements for transmitting rotary motion into rotary motion. The three concentric components of the harmonic drive gear are an inner elliptical wave generator, a nonrigid flexspline and an outer rigid circular spline. The harmonic drive gear utilizes the relative motion between the flexspline and circular spline. The relative motion occurs because the flexspline has two less teeth than the circular spline. At 0 degree of the wave generator's major axis the teeth are fully engaged. At 90 degree of rotation of the wave generator's major axis in a clockwise direction the teeth are disengaged. At one revolution of the major axis the flexspline moves in a counterclockwise direction with the two teeth advancement. The harmonic drive gear has the advantages of low or zero

backlash, mechanical advantage as high as 90%, high gear ratios, high positional accuracy, high repeatability, high reliability, compact packages, and simple support requirements. The components of the harmonic drive gear can have different configurations for the use as a speed reducer/increaser/and differential.

A coupler is a mechanical device to connect shafts so that it transfers the mechanical energy from the motor to the coupled system. An Oldham coupling is mainly used to connect collinearly a motor shaft to the input wave generator of the harmonic drive. A flexible coupling is often used to minimize the load force on the motor bearing caused by the misalignment between the two shafts coupled.

A bearing is used to aid in the rotational motion of shafts and to help provide for the linear motion of joints. Both linear and radial bearings are typically used in the joint mechanism of the robot manipulator for prismatic and revolute joints, respectively.

A screw is used to convert rotational motion generated by the motor into linear motion. As the screw rotates, the nut engaged with the screw and attached to the payload translates. A ball screw drive is typically used in the joint drive mechanism of the manipulator because of the high efficiency of transferring power and because of the driving and backdriving capacity.

3. DESIGN OF GUIDE VEHICLE

A trailer carrying a robotic sampling system is guided into the contaminated field by a truck with the necessary equipment. The limited soil sampling area due to the inaccessibility of the truck and possible danger to operators inside the truck due to the nature of the hazardous environment motivated the design of a separate guide vehicle. The guide vehicle, leaving the truck at a protected area, was designed and constructed to be capable of carrying a robotic sampling unit for surface sampling, or alternatively to pull the trailer carrying a remote manipulator into the contaminated field to obtain the soil samples at the desired locations.

In Section 3.1, the overall robotic surface sampling system in the contaminated field is presented. The design considerations and specifications of the remote-controlled guide vehicle are presented in Section 3.2. Section 3.3 demonstrates the capacity and construction of the guide vehicle. The overall configuration of the guide vehicle is also presented.

3.1 Overview of robotic surface sampling system

The first prototype of the overall robotic sampling system for real-time soil analysis in a contaminated field mainly constitutes a truck and a trailer shown in Figure 3.1. The remote-controlled guide vehicle is included in the second prototype of the sampling system as a guiding means of the trailer. The truck carries the computer equipment, pulsed Nd:Yag laser, spectrometer, and necessary equipment. The trailer is guided by the truck and carries the

remote robot manipulator with the surface soil sampler, Inductively Coupled Plasma (ICP) hardware, sensor equipment, and cleaning unit.

The trailer mounted remote manipulator consists of a shoulder, an upper arm, and a forearm. The soil sampler as an end effector is mounted on the end of the forearm of the manipulator. The soil sampler consists of a stepper-driven raster positioning system, probe laser optical system, ablation cell, and argon cell for ablating the soil samples by laser and transporting the ablated soil to the analysis devices. The ablation cell is mounted on the end of the sampling probe.

Figure 3.2 shows the functional diagram of the overall robotic surface soil sampling system with a remote-controlled guide vehicle. The manipulator is controlled by the Masters/Slave controller from the protected area. To move the trailer carrying the manipulator, the guide vehicle is controlled by either teleoperated control or radio control which is described in Chapter 4. The operator is included in the control loop of the system to make decisions.

3.2 Design considerations and specifications

The design considerations involve three main areas for the guide vehicle. These areas include the mechanical characteristics, the dynamic analysis, and the control aspects of the vehicle.

The mechanical requirements of the guide vehicle include payload capability and the horsepower to carry or pull the load up a specified incline. The design requirements of the guide vehicle were to be able to traverse an off-load (field) terrain and to be able to carry 500 lbs of equipment, a robotic sampling unit, or both, up a grade of 20 % at a speed of at least 5 mph. Likewise, the guide vehicle must be capable of pulling a trailer carrying a robotic sampling device at a speed of 5 mph. In addition, the guide vehicle should be able to make a

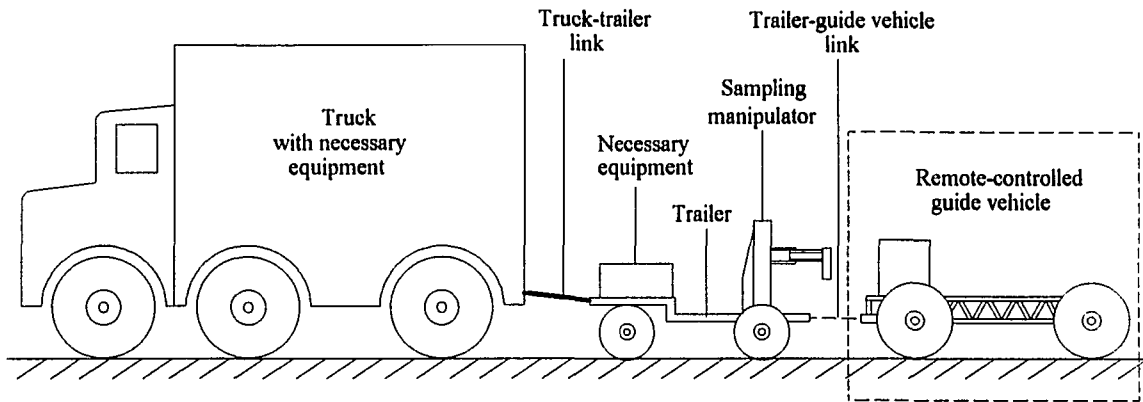


Figure 3.1: Robotic surface sampling system with the remote-controlled guide vehicle

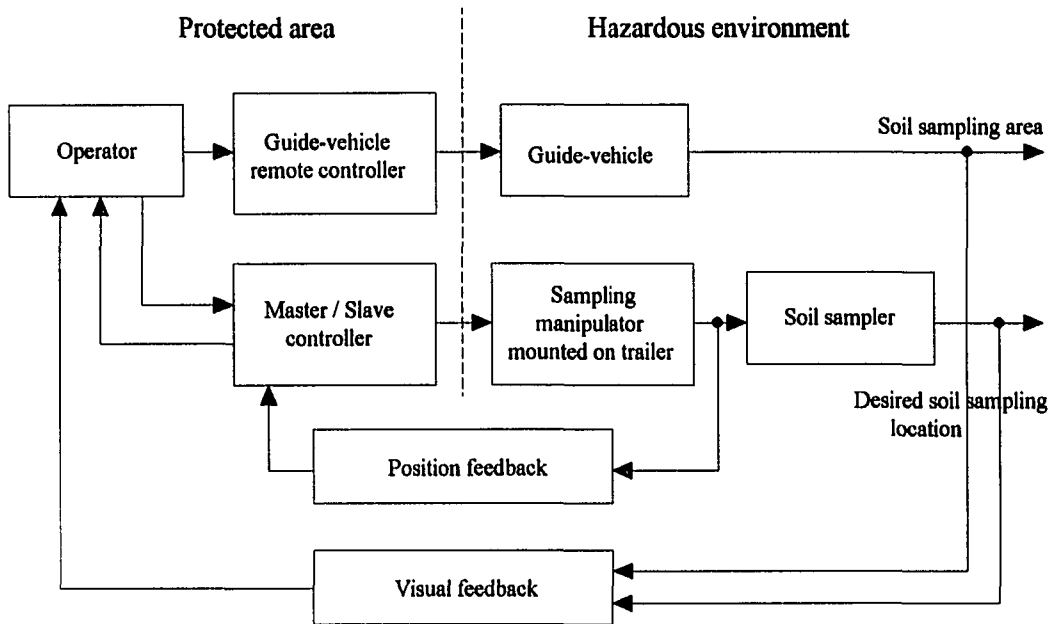


Figure 3.2: Schematic representation of the remote-controlled guide vehicle coupled with the remote manipulator located on the trailer

typical 90° turn at a typical 90° turn at a roadway intersection. Otherwise no special turning requirements were needed. The guide vehicle should also have platform space sufficient to carry a payload as well as its own control equipment and mechanisms including a 115 V motor generator power supply.

The guide vehicle is anticipated to travel over a rough surface due to the nature of the operation environment and is subject to forced excitation. This excitation might be undesirable to the guide vehicle pulling the trailer into the field if a large vibration amplitude develops. The analysis of dynamic characteristics of the guide vehicle is necessary to avoid resonance and to control it with an onboard computer system

Control of the guide vehicle is needed so that, without a driver onboard, the guide vehicle tows the trailer carrying the manipulator into the desired position in the contaminated field. To achieve autonomous control of the guide vehicle, the remote control techniques employed are teleoperated control and radio control.

3.3 Configuration of guide vehicle

The construction of the guide vehicle started from the two rear wheels, drive axle, engine, brake, and transmission which were donated by the John Deere Corporation of Moline, Illinois. From there, the body frame of the vehicle was built out of 1 inch square tubing with a thickness of 0.125 in. The platform on the guide vehicle was made out of aluminum with a thickness of 0.25 in. The first prototype, a three-wheeled guide vehicle with two rear wheels was built. Since this prototype had turning instability [26, 27], redesign to a four-wheeled guide vehicle was accomplished. Figure 3.3 shows the four-wheeled version of the guide vehicle.

The guide vehicle concept and the specifications required that a stretched version of a three- or four-wheeled motorcycle or all-terrain vehicle be developed with an equipment-

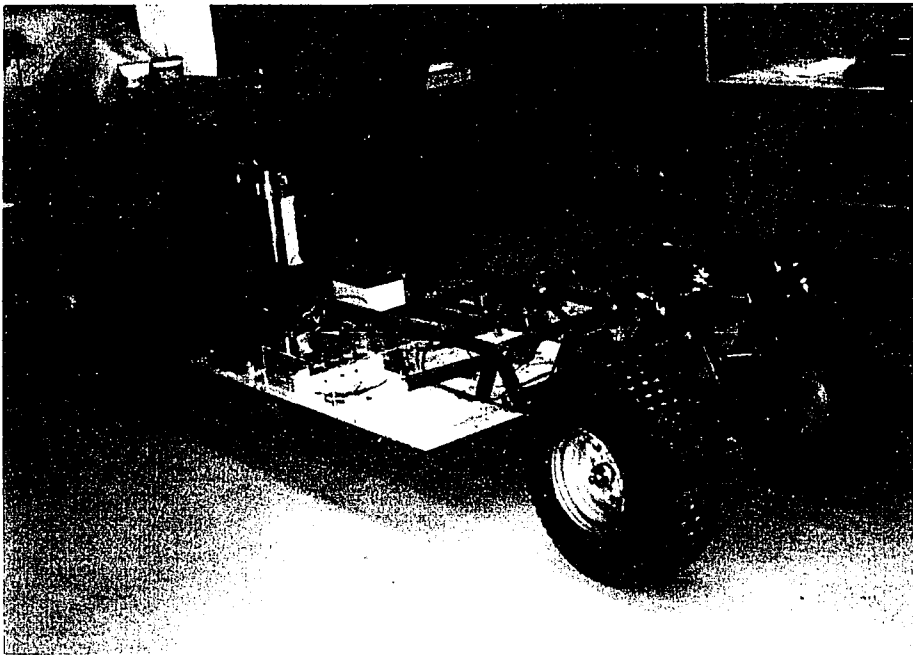
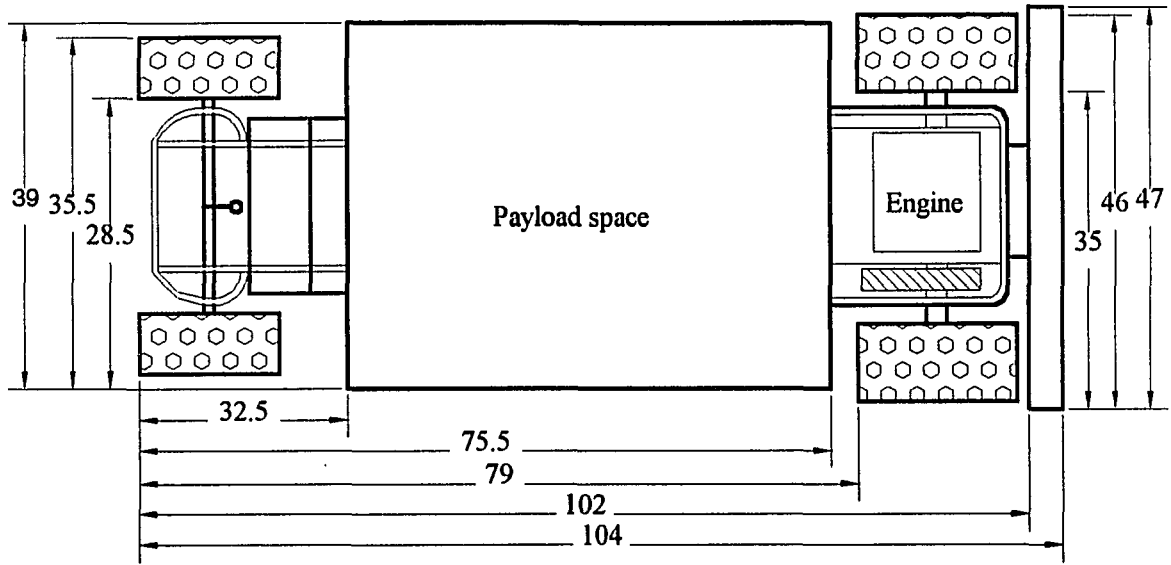


Figure 3.3: Four-wheeled guide vehicle

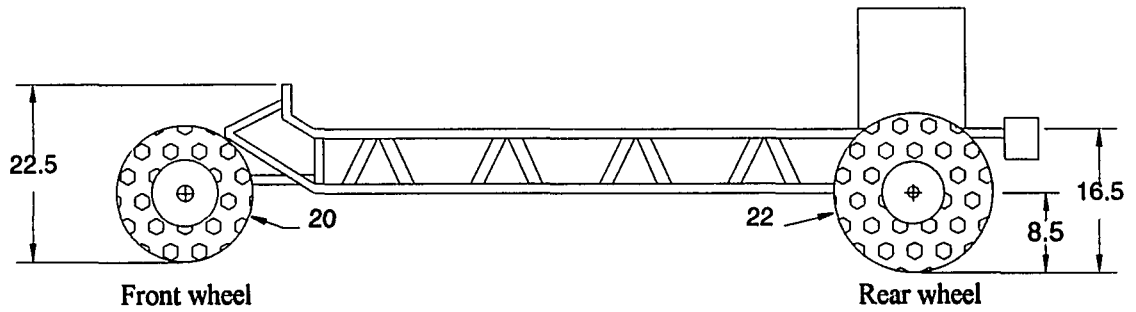
carrying platform. The space between the front and rear wheels was designed to contain an equipment and robot platform placed at axle height to give the vehicle a relatively low center of gravity. The resulting guide vehicle configuration is shown in Figure 3.4. The guide vehicle has an overall length of 104 in., width of 39 in., wheel base of 78 in., and a curb weight of about 300 lbs. The two front wheels have a diameter of 20 in. and a width of 7 in. each, while the two rear wheels have a diameter of 22 in. and a width of 11 in. each. The steering on the vehicle has a maximum rotation of 45°.

The platform space available for carrying payload has rectangular dimensions of 43 in. by 39 in. The platform on the guide vehicle was made in two layers such that the controls, some actuators, battery, and ballast for helping maintain vehicle stability could be placed on the lower platform. The upper platform was designed to be able to carry a motor-generator set as well as a vision system and other auxiliary equipment that would be necessary for the operation of the guide vehicle. This platform is also capable of carrying a robotic arm for obtaining soil samples. Design and construction of such an onboard robotic arm is a future effort.

The engine mounted on the guide vehicle is a single cylinder, four-stroke cycle engine with a piston displacement of 341 cm^3 . The maximum power developed by the engine is 8.4 horsepower. The engine is coupled to the transmission by means of a friction belt drive. The transmission on the guide vehicle is a hydrostatic type with forward, neutral, and reverse positions.



a) Top view



b) Front view

Figure 3.4: Configuration of the guide vehicle

4. REMOTE CONTROL OF GUIDE VEHICLE

Workers should have an extremely limited accessibility to the contaminated soil sampling area due to its dangerous nature without the aid of special equipment. A truck-guided-robotic sampling system might not be suitable for the sampling process at the desired sampling locations caused by inaccessibility of the truck. Therefore, it was necessary to design a remote controlled means for guiding the vehicle and trailer with the manipulator to the sampling site as well as to remove human operators from the hazardous environment.

The first phase study of the remote control system for the vehicle utilized teleoperated control from a long umbilical cord. The second phase study of the remote control system utilized radio control from a close-by site. A vision system such as video camera installed on the vehicle would provide the operator with good driving sense of the vehicle. In Section 4.1, the teleoperated control system, its mechanism, and linear actuator selection are presented. The radio control system and its servo mechanisms are presented in Section 4.2. The results of the field test are presented in Section 4.3.

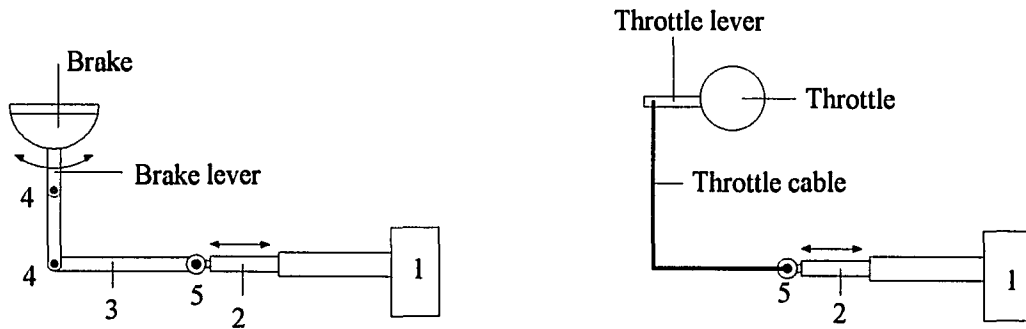
4.1 Teleoperated control system

The purpose of the teleoperated control is to make it possible for an operator to be located in another vehicle or at a safe, nonhazardous location nearby. In this manner, the guide vehicle can be controlled with a joy stick device through a suitable length of wiring or umbilical cord connected to the vehicle controls.

4.1.1 Mechanism

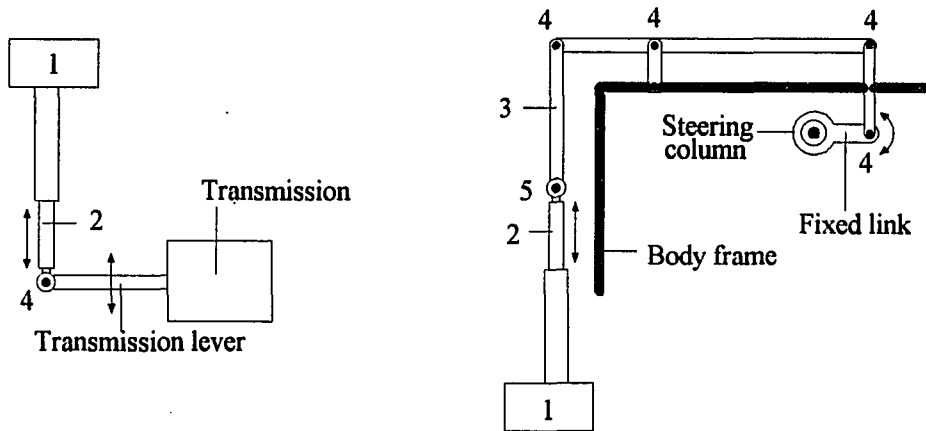
The control aspects of the design requires that the steering direction be controlled, that the engine speed or throttle be controlled, that the forward or reverse direction of the guide vehicle be controlled, and that the guide vehicle be able to stopped by a braking action. The control linkages are necessary so that linear movement of an actuator will provide the appropriate motion to move the throttle lever, the gear shift lever, the steering column, and the brake lever. Linear motion of the controls is desired so that linear actuators which convert rotational into translational motion, can be incorporated into the automatic or remote control of the vehicle.

Figure 4.1 shows the mechanisms used to control the brake, throttle, steering, and transmission system with the linear actuators. To achieve quick response in the control system, a one degree of freedom mechanism is used for the brake and steering system. In the brake mechanism, as shown in Figure 4.1 (a), the input link is connected directly to the linear actuator that is the power source. The output link is securely connected to the brake lever. The linear movement in the forward or backward direction of the telescopic member of the linear actuator causes a clockwise or counter clockwise pull of the brake lever, resulting in the brake operation. The throttle cable that is connected to the linear actuator is used to control the throttle lever as shown in Figure 4.1 (b). The retracting movement of the telescopic member of the linear actuator increases the engine speed. The rod end of the telescopic member of the linear actuator for the transmission system shown in Figure 4.1 (c) is directly connected to the gear shift lever for the forward, neutral, and reverse directions of the vehicle. In the steering mechanism, as shown in Fig 4.1 (d), a link is fixed to the steering column. The forward or backward movement of the linear actuator causes a clockwise or counter clockwise rotation of the input link about the pin joint, resulting in the rotation of the steering



a) Brake system.

b) Throttle system



c) Transmission system

d) Steering system

- 1: Linear actuator
- 2: Telescopic member of linear actuator
- 3: Input link
- 4: Pin joint
- 5: Fixed joint

Figure 4.1: Mechanism to be controlled with linear actuator

in the right or left direction. The steering on the vehicle has a maximum rotation of 45° in both the left and right directions.

4.1.2 System integration

The teleoperated control of the guide vehicle was accomplished by means of 100 ft long umbilical cord attached to a joy stick. The control panel was designed to control the linear actuators mounted on the guide vehicle. Figure 4.2 shows the overall block diagram of the teleoperated control system of the guide vehicle. The control panel consists of four double pole double throw switches with center-off positions. Each switch controls independently either the brake, the steering, the transmission, or the throttle system. Each item controlled required two 100 ft umbilical wires and two electrical relays. One end of the umbilical cord was connected to the switch and the other end to the relay. A relay was used in the control so that low voltage can be used for relay activation, while high current can pass through the relay contacts to supply the electrical energy for the linear actuators. Only one relay is turned on when the switch is activated. Both relays are turned off when the switch is turned off. A 12 V DC auto battery was used as a power source. The telescopic member of the linear actuator moves in the forward or backward direction with + 12 V DC or - 12 V DC supply, respectively, such that the related mechanism is activated.

4.1.3 Selection of linear actuator

The experiment performed on the guide vehicle after the manual controls were designed and installed on the guide vehicle included measuring forces and torques required for operation of the brake, steering, transmission, and throttle of the vehicle. The force necessary

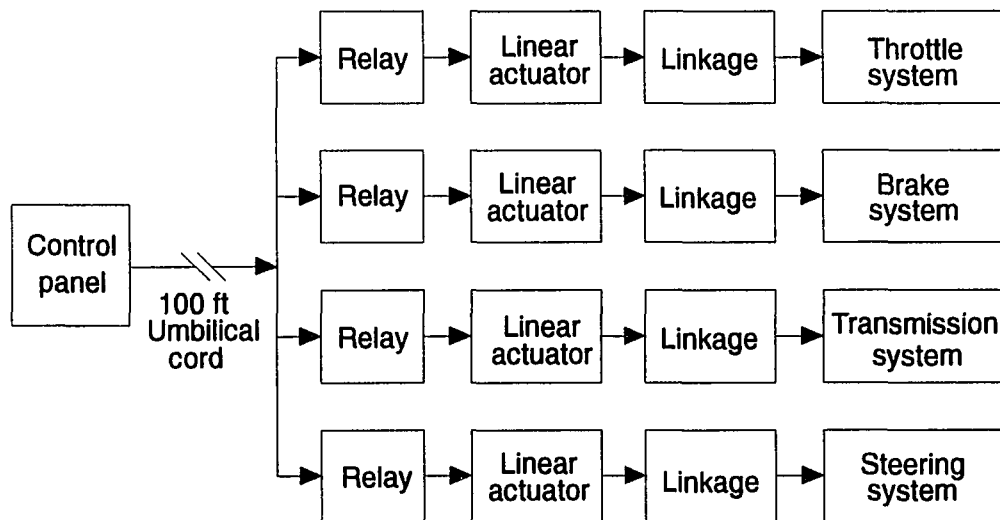


Figure 4. 2: Block diagram of the teleoperated control system

to activate the brake with the linkage designed was 12 lbs. For the linkages installed for manual control, the force necessary to activate the throttle control was 7 lbs and the transmission shift lever movement requires 12 lbs of force. The static torque needed to initiate the steering with the linkages on flat concrete pavement was 110 ft lbs of torque. Thus, linear actuators installed on the guide vehicle would have to be capable of achieving these loads or torques in order to activate the various controls. Such linear actuators that operate with a 12 V DC supply have been selected on the basis of the experimental results to give the required stroke along with the necessary force or torque. The ball screw drive linear actuators (Appendix D) selected have a feature of freewheeling to prevent overtravel at the end of stroke, and reduce a burden of externally mounting limit switches.

4.2 Radio control system

The radio control applies radio-controlled model technology such as is typically used with model airplanes, boats, and other scale-model vehicles. This type of control was selected so that the Federal Communication Commission (FCC) regulations would not be violated. The low force or torque actuation devices of the model controls are used to activate switches or relays in electrical circuits with sufficient power to activate the linear actuators for the throttle, transmission, brake, and steering controls on the mobile vehicle.

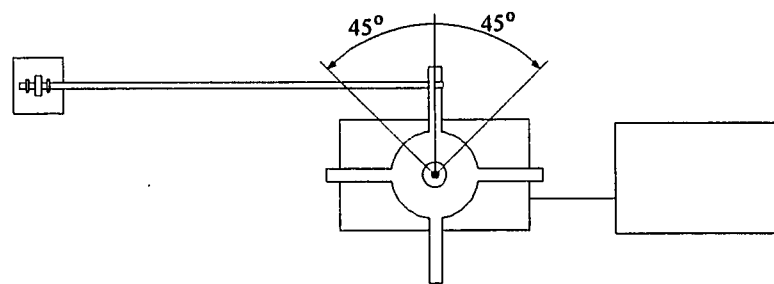
4.2.1 Servo mechanism

The radio control system (Airtronics Inc., Vanguard PCM 6H) used to remotely control the guide vehicle consists of a transmitter, receiver, servo mechanism, and battery. The 500 milliwatt transmitter has a capability to reverse the direction of servo rotation, and a capability of selection of *FM/PPM* (Pulse Position Modulation) or *FM/PCM* (Pulse Code

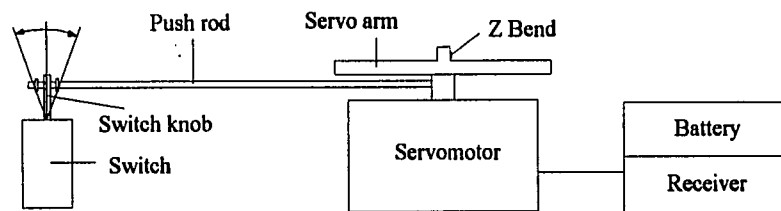
Modulation). The receiver has a capability of dual conversion for 6 channels with the *PCM* narrow band. The servomotors (Appendix D) have high torque capacity to activate the switches through push rods that are connected to the servo arms. Figure 4.3 shows the radio control mechanism used to remotely control the vehicle. The spline shaft output of the servomotor has 23 teeth. The cross shaped servo arm is connected to the servo motor through the spline shaft. A switch (double-pole double-throw switch with center-off) is connected to the servo arm with the straight slender push rod. The push rod was made out of stiff material so as to prevent the flexing and whipping due to the vibration of the vehicle during the operation. One end of the push rod is bent in a 'Z' shape in order to prevent the push rod from becoming disconnected from the servo arm. The other end is threaded and connected to the switch with the nuts on both sides, leaving a free space between the nuts, because excessive tightening may result in misalignment that may cause high current drain on the battery, change the operating time, or cause loss of control and damage the vehicle and the robotic sampling system. Each servo arm has a maximum rotation of 90° (45° for each rotation sense).

4.2.2 System integration

The long umbilical wires employed for the teleoperated control described in Section 4.1 were removed. Circuit wiring was used to connect the switches and relays which are mounted on the guide vehicle. The control panel was designed to control the linear actuators mounted on the guide vehicle. Figure 4.4 shows the control mechanism installed on the lower platform of the guide vehicle. The low force or torque actuation devices of the controls were used to activate switches or relays in electrical circuits with sufficient power to drive the linear actuators. Figure 4.5 shows the overall remote control system of the vehicle: brake, throttle, transmission, and steering system. When the command signal from the transmitter (by a



a) Top view



b) Side view

Figure 4.3: Schematic of servo mechanism for the radio control system

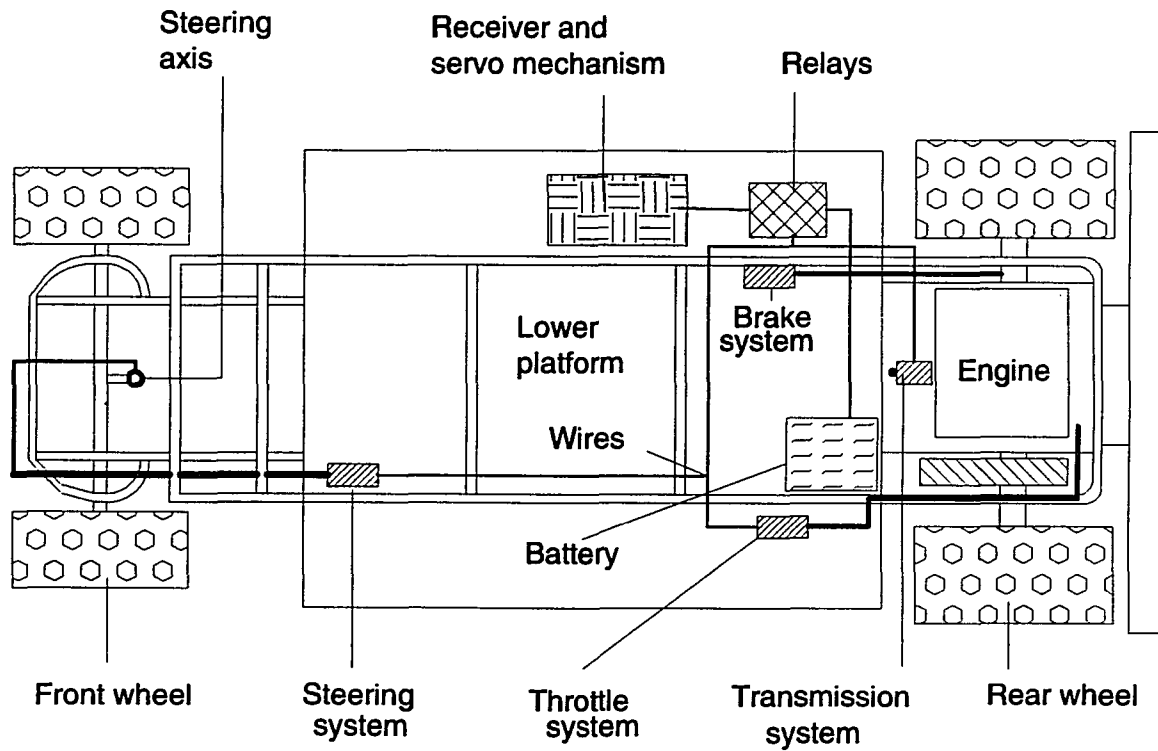


Figure 4.4: Control mechanism mounted on the guide vehicle

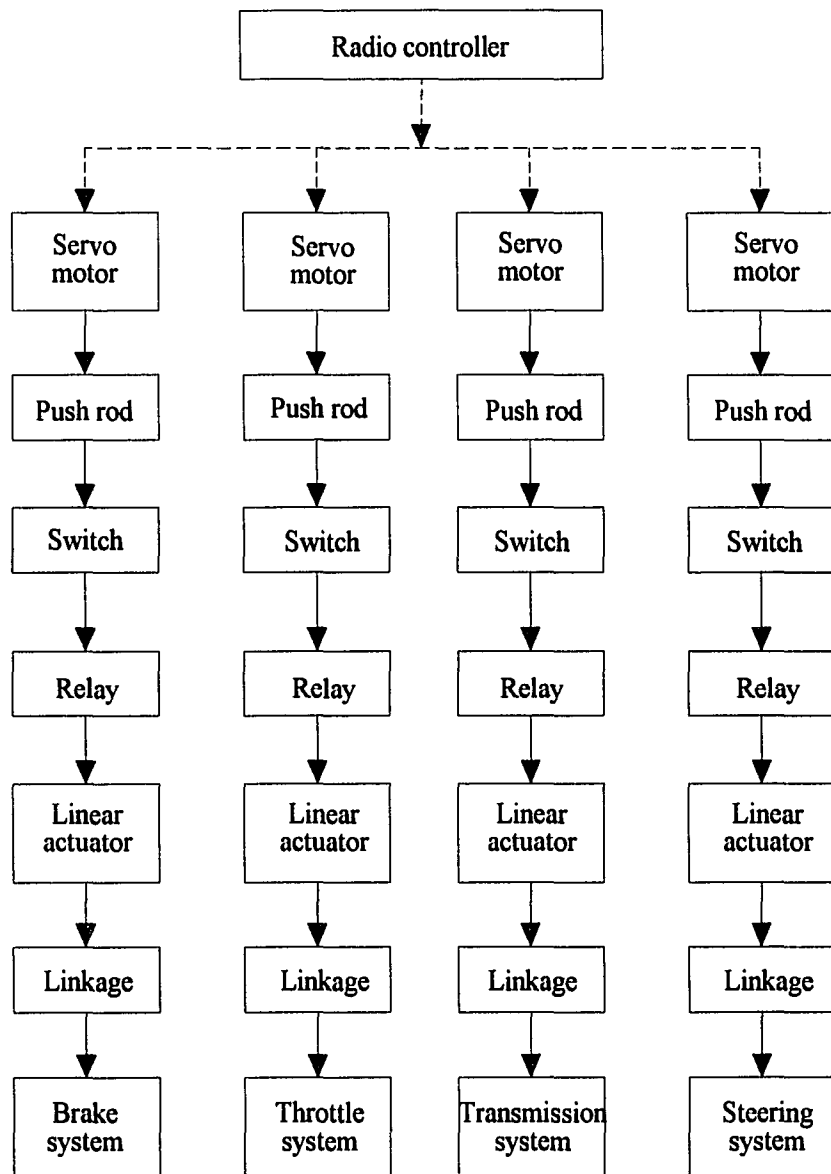


Figure 4.5: Block diagram of the radio control system

human operator) is sent to the receiver through the antenna, the servomotor connected to the receiver is activated. The rotation of the servo arm makes the push rod activate a relay switch, resulting in the linear movement in a forward or backward direction of the telescopic member of the linear actuator.

4.3 Field test

The first prototype test of the four-wheeled guide vehicle was performed manually in the field. The second stage of testing of the guide vehicle was performed outdoors from a 100-ft long umbilical cord. The final stage of testing the guide vehicle was remotely tested in the field by radio control without aid of the umbilical cord.

When operated on level ground by means of a manual, teleoperated, and radio control, the vehicle performed satisfactorily, meeting all the design requirements. It achieved speeds of 15 mph carrying a payload of over 700 lbs. On a 22° slope the guide vehicle could achieve speeds of 6 mph carrying a payload of over 500 lbs. The vehicle made a 90° turn at a roadway intersection with a turning radius of 32 ft. By radio control, the guide vehicle can be controlled within an operating range of up to 1 mile depending on the local FCC regulations. Thus, the mechanical configuration and operation of the guide vehicle met or exceeded the original design requirements. One difficulty that may be encountered when controlling the guide vehicle by the teleoperated control is that the long cables may become entangled.

5. REMOTE ROBOT MANIPULATOR

In this chapter, the trailer mounted remote manipulator for the robotic contaminant surface soil analysis system is described. In Section 5.1, the problems associated with the sampling task of the manipulator as constructed are presented. The control system for the manipulator to perform complex sampling tasks in hazardous waste sites is also proposed. The overall structure of the manipulator is presented in Section 5.2. The assignment of the link coordinate frames, the forward and inverse kinematics solutions, and the Jacobian matrices of the manipulator are presented in Section 5.3.

5.1 Problems associated with sampling tasks

A remote robot manipulator [4] was developed in the Ames National at ISU to assist in the automation of surface contaminant analysis in nearly real-time fashion in hazardous waste sites. After the trailer carrying the remote manipulator is guided into the sampling site by the remote-controlled guide vehicle described in the previous chapter, the operator controls the manipulator to position the soil sampler (end effector) to the sampling spot specified using visual feedback from the video camera. If the operator is skillful, and/or the surroundings to be sampled are accurately known and compliant, the tasks of positioning and sealing the soil sampler from the soil to be sampled can be easily achieved.

However, it is envisioned that the manipulator and operator would encounter uncertainties due to the nature of the remote and unstructured surroundings. If the soil

hardness is high, or if knowledge about the surroundings is lacking, or if there are uncertainties regarding the composition of the soil surface (such as soil with rocks), it becomes more difficult for the manipulator to position and seal the soil sampler with the result of the leakage of argon gas from the ablation cell.

Taking into account the problems described above, a compliant motion control is necessary for the manipulator controller. The sampling task of the manipulator requires interactions with the harsh and unstructured surroundings, along with accurate maneuvering in free and unconstrained space. In constrained maneuvering, the interaction forces must be accommodated rather than resisted to comply with the natural constraints. Both force and position control are required to accomplish successfully the sampling task involving compliant motion in hazardous waste sites. The compliant motion control [28-30] is based on the mechanical impedance of the manipulator end effector and the dynamic relationship between the end effector/environment interaction forces and end effector position. In this method, the end effector position is controlled and its relationship with the interaction forces is specified so that the appropriate contact forces are maintained to enable the manipulator to maneuver in constrained space. These compliant motion control techniques require an adequate dynamic model and known parameter values of the manipulator.

5.2 Overview of remote manipulator

The remote robot manipulator consists of a base link, and upper arm and forearm links, which are connected through prismatic, revolute and revolute joints in sequence. Figure 5.1 shows the manipulator with a soil sampler as mounted on the trailer and Figure 5.2 shows the workspace of the manipulator. Vertical translation of the arm allows arbitrary positioning of the end effector with respect to the ground over a stroke of 30 inches. Rotation of the upper

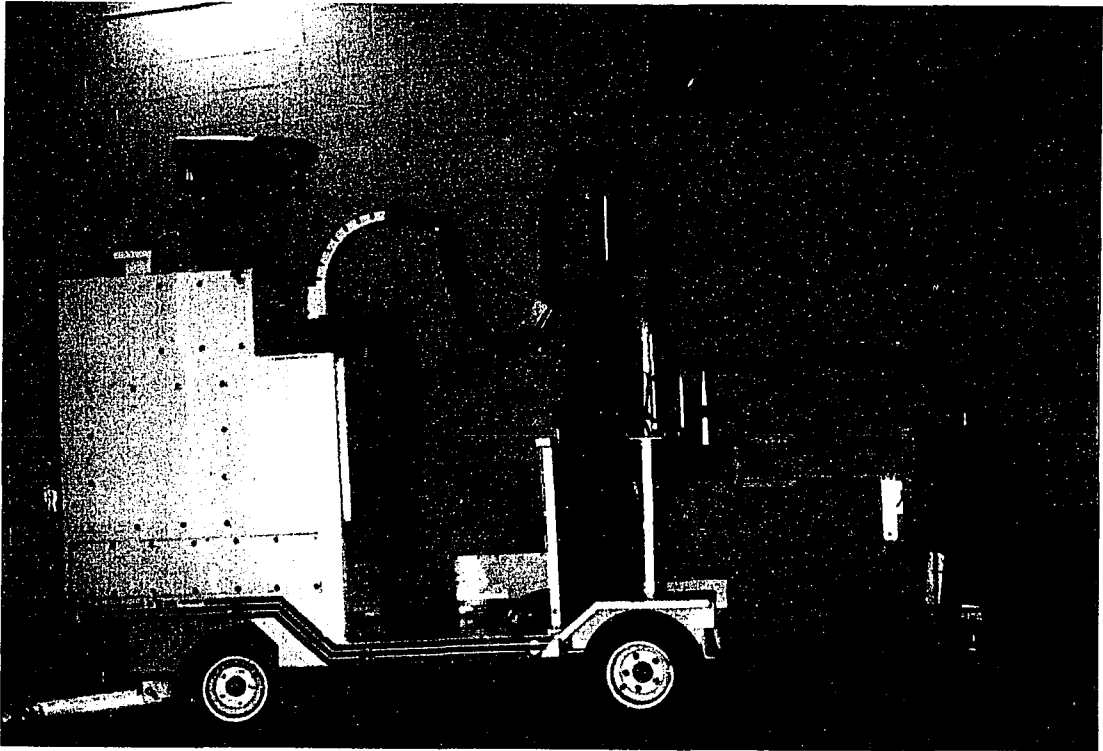
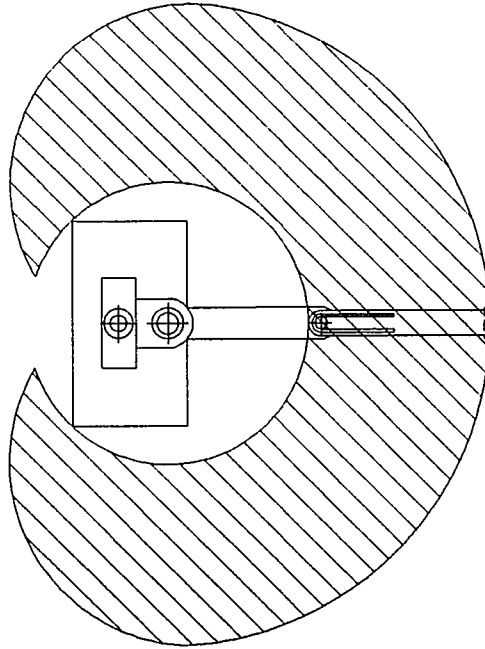
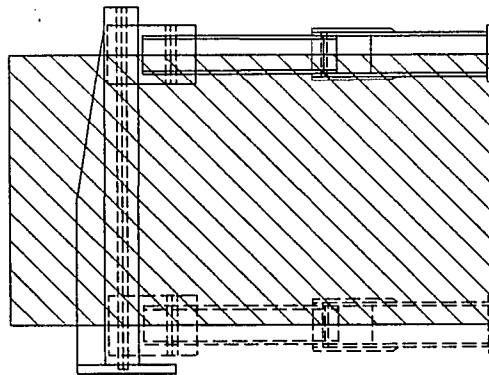


Figure 5.1: Remote manipulator located on the trailer



a) Top view



b) Side view

Figure 5.2: Workspace of the manipulator located on the trailer

arm and forearm over 90° and 260° , respectively, enable the horizontal positioning of the end effector. The manipulator has a capacity of carrying 50 lbs load at the end of the forearm.

The upper arm and forearm of the manipulator were constructed with structural aluminum alloy (Aluminum 6061-T6). A low carbon steel was used to construct the base of the manipulator. A one inch diameter Thompson ball screw (Lead of 0.25 in./rev.) and ball nut were used to raise and lower the arm. Harmonic drives as speed reducers (100 : 1) were used in power transmission to the revolute joints for the upper arm and forearm. The output flexspline of the harmonic drive was directly connected to the joint for the upper arm. A timing belt and pulley were used to transmit the torque from the output flexspline to the forearm.

DC servomotors (Robbins & Meyers/Electrocraft) were used to drive each joint. Incremental encoders (100 pulses/rev) as position sensors were built onto the back of each servomotor. Proximity switches (Baumer Electric) were used to indicate the maximum and minimum positions of each axis.

A Master/Slave controller coupled with a PID controller was employed to control the manipulator. The remote manipulator (slave) was controlled by the master controller which was a scaled replica of the manipulator (slave). The replica utilized potentiometers to generate desired signals. Analog signals generated were converted into digital signals through Analog to Digital Converters (ADC), sent to the controller, and then delivered to the motors to create the motion.

5.3 Kinematics of remote manipulator

The kinematics of the manipulator motion are characterized by specifying the positions, velocities, and accelerations of the links of a robot manipulator without considering the forces

or torques causing the resulting motion. The kinematic equations for the manipulator describe the geometrical configuration of the kinematic chain that is formed with links and joints, as a function of time relative to a fixed universal coordinate frame. As will be presented in the next chapter, the dynamics of the remote manipulator describe the relationship between the forces and torques required to actuate the manipulator. Thus, the study of kinematics and dynamics of the manipulator is essential for the control of the manipulator.

5.3.1 Coordinate frame assignment

By the modified Denavit-Hartenberg notation [12] (for details, see Appendix A), the link coordinate frames are assigned to links of the remote manipulator, as shown in Figure 5.3. Figure 5.4 shows the kinematic parameters and coordinate frame assignments. Figures 5.3 and 5.4 are drawn with joint 1 position variable d_1 at a positive value. The base frame {0} is attached to the base of the robot and is coincident with the frame {1} when d_1 is zero. Frames {2} and {3} are attached to links 2 and 3, respectively, with their z -axes along the axes of joints 2 and 3. The Denavit-Hartenberg (D-H) parameters where a_{i-1} and α_{i-1} are link lengths and twists, and where d_i and θ_i are joint offsets and angles, are given in Table 5.1.

5.3.2 Forward kinematics

Given the values of the joint variables of the manipulator, the forward (direct) kinematic problem is to compute the position and orientation of the end effector with respect to the base frame in terms of the joint variables.

Using equation A.2, the transformation matrices describing the link frames for the manipulator are as follows:

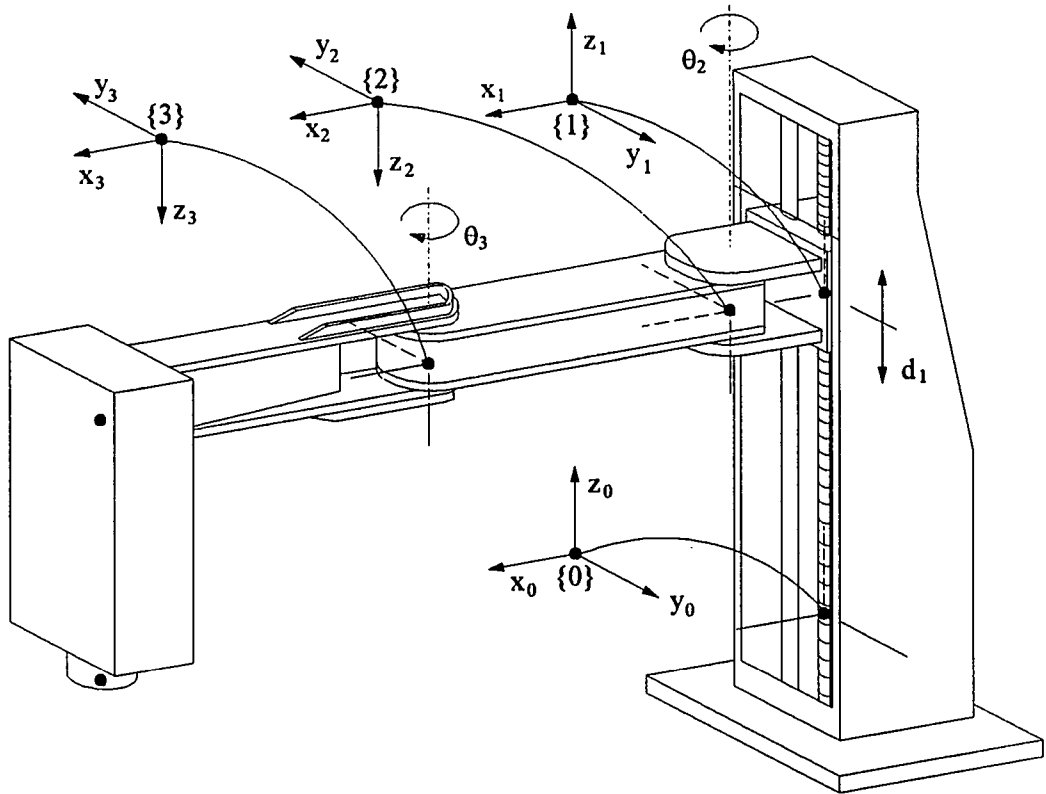


Figure 5.3: Schematic of the three DOF manipulator located on the trailer

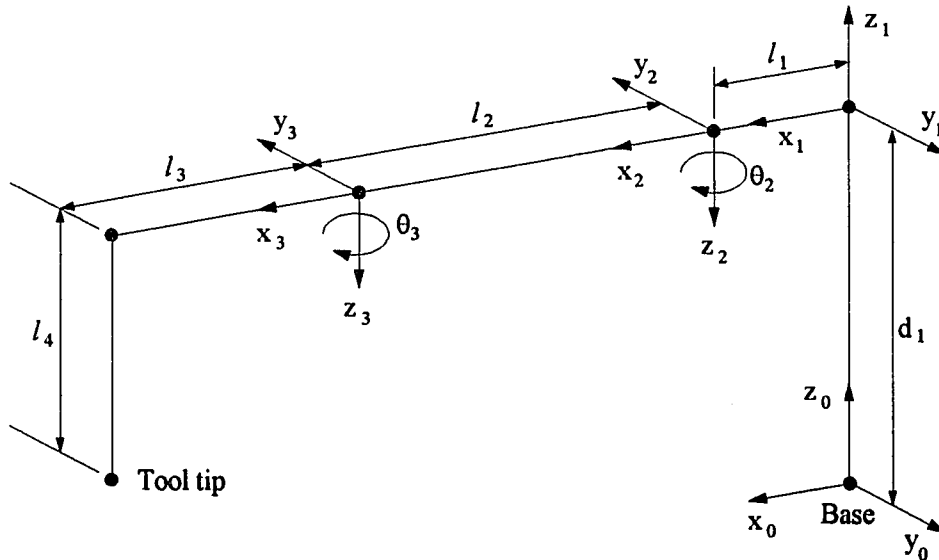


Figure 5.4: Link coordinate frame assignments of the manipulator located on the trailer

Table 5.1: D-H parameters for the manipulator located on the trailer

i	a_{i-1}	α_{i-1}	d_i	θ_i
1	0	0	d_1	0
2	l_1	180°	0	θ_2
3	l_2	0	0	θ_3

$${}^0_1T = \begin{pmatrix} 1 & 0 & 0 & 0 \\ 0 & 1 & 0 & 0 \\ 0 & 0 & 1 & d_1 \\ 0 & 0 & 0 & 1 \end{pmatrix} \quad (5.1)$$

$${}^1_2T = \begin{pmatrix} C_2 & -S_2 & 0 & l_1 \\ -S_2 & -C_2 & 0 & 0 \\ 0 & 0 & -1 & 0 \\ 0 & 0 & 0 & 1 \end{pmatrix} \quad (5.2)$$

$${}^2_3T = \begin{pmatrix} C_3 & -S_3 & 0 & l_2 \\ S_3 & C_3 & 0 & 0 \\ 0 & 0 & 1 & 0 \\ 0 & 0 & 0 & 1 \end{pmatrix} \quad (5.3)$$

where $S_i \equiv \text{Sin}(\theta_i)$ and $C_i \equiv \text{Cos}(\theta_i)$ for $i = 2, 3$.

The description of the position and orientation of frame {3} relative to the base frame {0} is computed using equation (A.4):

$${}^0_3T = {}^0_1T {}^1_2T {}^2_3T \quad (5.4)$$

$${}^0_3T = \begin{pmatrix} C_{23} & -S_{23} & 0 & l_1 + l_2 C_2 \\ -S_{23} & -C_{23} & 0 & -l_2 S_2 \\ 0 & 0 & -1 & d_1 \\ 0 & 0 & 0 & 1 \end{pmatrix} \quad (5.5)$$

where $S_{23} \equiv \text{Sin}(\theta_2 + \theta_3)$ and $C_{23} \equiv \text{Cos}(\theta_2 + \theta_3)$. The position of the tool tip relative to the frame {3} (see Figure 5.4) is expressed by

$${}^3P_{\text{tooltip}} = [l_3 \ 0 \ l_4]^T \quad (5.6)$$

and its position relative to the base frame {0} is thus given by

$${}^0P_{tooltip} = {}^0T^3 {}^3P_{tooltip} \quad (5.7)$$

$${}^0P_{tooltip} = \begin{bmatrix} l_1 + l_2 C_2 + l_3 C_{23} \\ -l_2 S_2 - l_3 S_{23} \\ -l_4 + d_1 \end{bmatrix} \quad (5.8)$$

5.3.3 Inverse kinematics

Given the position in Cartesian space for the tool tip of the manipulator, the inverse kinematics problem is to find the values for the joint variables, d_1 , θ_2 , and θ_3 . Let the desired position of the tool tip with respect to the base frame $\{0\}$ be

$${}^0P_{tooltip} = \begin{bmatrix} P_x \\ P_y \\ P_z \end{bmatrix} \quad (5.9)$$

Multiplying each side of equation (5.7) by the inverse transformation matrix $({}^0T^3)^{-1}$, we obtain

$$({}^0T^3)^{-1} {}^0P_{tooltip} = {}^1T^3 {}^3P_{tooltip} \quad (5.10)$$

Computing equation (5.10), we have

$$P_x = l_1 + l_2 C_2 + l_3 C_{23} \quad (5.11)$$

$$P_y = -l_2 S_2 - l_3 S_{23} \quad (5.12)$$

$$P_z - d_1 = -l_4 \quad (5.13)$$

From equation (5.13), we obtain

$$d_1 = P_z + l_4 \quad (5.14)$$

Summing the squares of equations (5.11) and (5.12), we obtain

$$P_x^2 + P_y^2 + l_1^2 - 2P_x l_1 = l_2^2 + l_3^2 + 2l_2 l_3 C_3 \quad (5.15)$$

Thus, θ_3 is expressed by

$$\theta_3 = \pm A \tan 2(g_1, g_2) \quad (5.16)$$

where

$$g_1 = \{4l_2^2 l_3^2 - (P_x^2 + P_y^2 + l_1^2 - l_2^2 - l_3^2 - 2P_x l_1)^2\}^{\frac{1}{2}} \quad (5.17)$$

and

$$g_2 = P_x^2 + P_y^2 + l_1^2 - l_2^2 - l_3^2 - 2P_x l_1 \quad (5.18)$$

For the computation of joint variable θ_2 , equations (5.11) and (5.12) can be rewritten as

$$P_x - l_1 = q_1 C_2 - q_2 S_2 \quad (5.19)$$

$$P_y = -q_1 S_2 - q_2 C_2 \quad (5.20)$$

where

$$q_1 = l_2 + l_3 C_3 \quad (5.21)$$

$$q_2 = l_3 S_3$$

Working with coefficients q_1 and q_2 ,

$$u = (q_1^2 + q_2^2)^{\frac{1}{2}} \quad (u > 0) \quad (5.22)$$

and

$$\beta = A \tan 2(q_2, q_1) \quad (5.23)$$

then

$$q_1 = u \cos \beta \quad (5.24)$$

$$q_2 = u \sin \beta$$

Equations (5.19) and (5.20) can be expressed by

$$\frac{P_x - l_1}{u} = \cos(\beta + \theta_2) \quad (5.25)$$

$$\frac{-P_y}{u} = \text{Sin}(\beta + \theta_2) \quad (5.26)$$

Hence, we obtain

$$\theta_2 = A \tan 2(-P_y, P_x - l_1) - A \tan 2(q_2, q_1) \quad (5.27)$$

5.3.4 Manipulator Jacobian matrix

The manipulator Jacobian relates the joint rates to the velocity of the tool tip of the manipulator. The Jacobian allows the computation of a differential changes in the location of the tool tip caused by differential changes in the joint variables. The Jacobian for the manipulator can be computed by propagating the velocities from the base of the manipulator to the tool tip, or by differentiating the position vector of the tool tip.

The Cartesian velocity of the tool tip and the joint rates of the manipulator are related by the Jacobian matrix as

$$\mathbf{V} = \mathbf{J} \dot{\boldsymbol{\theta}} \quad (5.28)$$

where \mathbf{V} is a column vector of Cartesian velocity components, \mathbf{J} is a Jacobian matrix as a function of the joint variables, and $\dot{\boldsymbol{\theta}}$ is a column vector of the joint rates. The inverse Jacobian is used to solve for the joint rates from the Cartesian velocity vector as

$$\dot{\boldsymbol{\theta}} = \mathbf{J}^{-1} \mathbf{V} \quad (5.29)$$

The singularities of the manipulator are found where the inverse Jacobian matrix \mathbf{J}^{-1} fails to exist.

The external forces and joint torques/forces (static loading case) are expressed by

$$\boldsymbol{\tau} = \mathbf{J}^T \mathbf{F} \quad (5.30)$$

where τ is a column vector of the joint torques, J^T is the transpose of the Jacobian, and F is the external Cartesian force vector acting on the tool tip of the manipulator.

For the three-axis remote manipulator, the Jacobian matrix 0J written in the base frame {0} is given by

$${}^0J = \begin{pmatrix} 0 & -l_2S_2 - l_3S_{23} & -l_3S_{23} \\ 0 & -l_2C_2 - l_3C_{23} & -l_3C_{23} \\ 1 & 0 & 0 \end{pmatrix} \quad (5.31)$$

The Jacobian J written in terms of a tool frame located at the tool tip and having same orientation as frame {3} is given by

$$J = {}^3_0R {}^0J \quad (5.32)$$

$$J = \begin{pmatrix} 0 & l_2S_3 & 0 \\ 0 & l_3 + l_2C_3 & l_3 \\ -1 & 0 & 0 \end{pmatrix}$$

6. DYNAMICS OF REMOTE ROBOT MANIPULATOR

The dynamics of the manipulator describe the relationship between the forces and torques required to actuate the manipulator. The analysis of the dynamic characteristics of a manipulator is necessary to simulate and control it as well as to evaluate and improve its performance. Newton-Euler and Lagrangian formulations are well adapted in developing the dynamic equations of motion of a robotic arm.

In Section 6.1, the dynamic equations of motion for the remote manipulator located on the trailer are presented by the Newton-Euler and Lagrangian formulation [31,32]. Motor dynamics are derived in Section 6.2. The integrated dynamic model for an actuator-transmission-link with friction is developed in Section 6.3.

6.1 Dynamics of manipulator

Two methods were used in developing the dynamic model for the motion of the three-axis remote manipulator located on the trailer: the Newton-Euler and the Lagrangian formulations (for details, see Appendices B and C). The equations of motion obtained by the Lagrangian formulation are the same form as given by the Newton-Euler formulation.

For the case which the manipulator is moving freely in its workspace, the joint driving torques given in equations (B.22) through (B.24) can be written as

$$\tau = M(q)\ddot{q} + H(q)\left[\dot{q}^2\right] + D(q)\left[\dot{q}\dot{q}\right] + G \quad (6.1)$$

where

$\tau = [\tau_1 \ \tau_2 \ \tau_3]^T$ is the 3 x 1 vector of the actuator torques,

q is the vector of generalized coordinates (or position variables),

$q_1 = d_1, q_2 = \theta_2, \text{ and } q_3 = \theta_3,$

$M(q)$ is the mass matrix which is symmetric and positive definite,

$H(q)$ is the centrifugal acceleration coefficients matrix,

$D(q)$ is the Coriolis acceleration coefficients matrix,

G is the gravity force vector which is independent of joint variables,

and where

$$\ddot{q} = [\ddot{d}_1 \ \ddot{\theta}_2 \ \ddot{\theta}_3]^T, [\dot{q} \ \dot{q}] = [\dot{d}_1 \dot{\theta}_2 \ \dot{d}_1 \dot{\theta}_3 \ \dot{\theta}_2 \dot{\theta}_3]^T, \text{ and } [\dot{q}^2] = [\dot{d}_1^2 \ \dot{\theta}_2^2 \ \dot{\theta}_3^2]^T.$$

The elements of the terms $M(q)$, $H(q)$, $D(q)$ and G are as follows:

$$M(q) = \begin{bmatrix} M_{11} & 0 & 0 \\ 0 & M_{22} & M_{23} \\ 0 & M_{23} & M_{33} \end{bmatrix}, \quad (6.2)$$

$$M_{11} = m_1 + m_2 + m_3$$

$$M_{22} = m_2(x_{c2}^2 + y_{c2}^2) + m_3(x_{c3}^2 + 2l_2x_{c3}C_3 - 2l_2y_{c3}S_3 + y_{c3}^2 + l_2^2) + I_{2,33} + I_{3,33}$$

$$M_{23} = m_3(x_{c3}^2 + l_2x_{c3}C_3 - l_2y_{c3}S_3 + y_{c3}^2) + I_{3,33}$$

$$M_{33} = m_3(x_{c3}^2 + y_{c3}^2) + I_{3,33}$$

$$H(q) = \begin{bmatrix} 0 & 0 & 0 \\ 0 & 0 & -H_{23} \\ 0 & H_{23} & 0 \end{bmatrix}, \quad H_{23} = m_3l_2[x_{c3}S_3 + y_{c3}C_3] \quad (6.3)$$

$$D(q) = \begin{bmatrix} 0 & 0 & 0 \\ 0 & 0 & 0 \\ 0 & 0 & D_{33} \end{bmatrix}, \quad D_{33} = -2H_{23} \quad (6.4)$$

$$G = [G_{11} \ 0 \ 0]^T, \quad G_{11} = (m_1 + m_2 + m_3)g \quad (6.5)$$

For the case in which the external force vector $F = [F_x \ F_y \ F_z]^T$ is exerted by the environment on the end of the soil sampler (end-effector), equation (6.1) can be expressed as

$$\tau = M(q)\ddot{q} + H(q)\left[\dot{q}^2\right] + D(q)\left[\dot{q}\dot{q}\right] + G + J(q)^T F \quad (6.6)$$

where $J(q)$ is the Jacobian for the manipulator as written in equation (5.32), and where F is described in the tool frame. It is also assumed that F is actuating at the tool tip of the soil sampler.

6.2 Motor dynamics

One of the common actuators employed in a control system of a robot joint is the direct current (DC) servomotor which is armature-controlled with a fixed permanent field magnet. The servomotor is the one whose driving signal is a function of servo error, that is, the difference between the desired position and or velocity and the measured actual position and or velocity. Since the field current is constant over the large variations of armature current, the non-turning part of the motor(stator) has no dynamic effects caused by the field. Armature controlled dc motors have some advantages for robotic applications such as reduced cooling requirements, self-induced damping by back eletromotive force (emf), high stall torque, compactness and lighter weight, and linear characteristics of the speed-torque curve.

An electric circuit of an armature controlled dc servomotor [33] is well known, as shown in Figure 6.1. The differential equation for the armature circuit is given by

$$V_a(t) = L_a \frac{dI_a(t)}{dt} + R_a I_a(t) + E_b(t) \quad (6.7)$$

where $V_a(t)$ is the voltage applied to the armature terminals, L_a is the armature winding inductance, $I_a(t)$ is the armature current, R_a is the armature resistance, and $E_b(t)$ is the back

emf. For a constant field current, the torque $\tau_m(t)$ generated by the motor is proportional to the armature current $I_a(t)$. Thus,

$$\tau_m(t) = K_m I_a(t) \quad (6.8)$$

where K_m is the motor torque constant. The back emf $E_b(t)$ is proportional to the angular velocity $d\theta_m / dt$ of the motor shaft so that

$$E_b(t) = K_b \frac{d\theta_m(t)}{dt} \quad (6.9)$$

where K_b is the back emf constant. Combining equations (6.7) through (6.9), the motor dynamics are expressed by a first order differential equation given by

$$V_a(t) = K_b \frac{d\theta_m(t)}{dt} + \frac{R_a}{K_m} \tau_m(t) + \frac{L_a}{K_m} \frac{d\tau_m(t)}{dt} \quad (6.10)$$

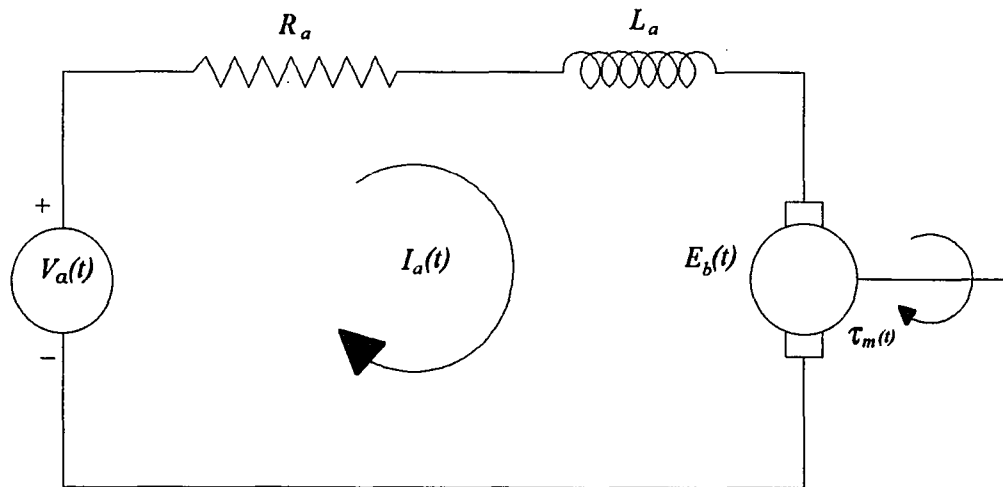


Figure 6.1: Armature circuit model of a dc servomotor

For the simplicity, the armature inductance is usually small and can be neglected [33]. Equation (6.10) is then reduced to

$$V_a(t) = K_b \frac{d\theta_m}{dt} + \frac{R_a}{K_m} \tau_m(t) \quad (6.11)$$

For joint i of the manipulator, the equation above can be rewritten as

$$V_{ai} = K_{bi} \dot{\theta}_{mi} + \frac{R_{ai}}{K_{mi}} \tau_{mi} \quad (6.12)$$

6.3 Dynamics of actuator-transmission-load system

The dynamic equations of motion for the integrated actuator-transmission-load system are derived with the assumption that the manipulator is a jointed rigid body. In addition, the elasticity of the transmission systems for joints is neglected. The effects of friction (viscous friction and combined Coulomb friction and stiction) are fully taken into account in the derivation of the integrated dynamics equations of motion for the manipulator.

6.3.1 Actuator-transmission-load system

A ball screw is used as the transmission element to raise and lower the link 1 as shown in Figure 6.2. The motor shaft is rigidly connected to the screw end.

The equation of the motion of the screw-mass system is expressed by

$$\tau_{m1} = I_{m1} \ddot{\theta}_{m1} + \tau_s \quad (6.13)$$

where τ_{m1} is the torque generated by the motor 1, I_{m1} is the combined moment of inertia of the motor assembly and screw, τ_s is the load torque, θ_{m1} is the angular displacement of the motor shaft and is equal to the angular displacement of screw. For the linear motion of the load on the screw, the work done W is given by

$$W = F_s d_1 \quad (6.14)$$

where F_s is the output force imparted by the screw and d_1 is the displacement of the payload.

Corresponding this work is given by

$$W = \tau_s \theta_{m1} \quad (6.15)$$

Thus, from equations (6.14) and (6.15) , we obtain

$$\tau_s = \frac{d_1}{\theta_{m1}} F_s \quad (6.16)$$

The relationship between the lead L_s (in./rev.) of the screw and the angular displacement of the screw is expressed by

$$d_1 = L_s \theta_{m1} \quad (6.17)$$

Substituting equations (6.16) and (6.17) into equation (6.13), the torque τ_{m1} generated by the motor 1 is given by

$$\tau_{m1} = I_{m1} \ddot{\theta}_{m1} + L_s F_s \quad (6.18)$$

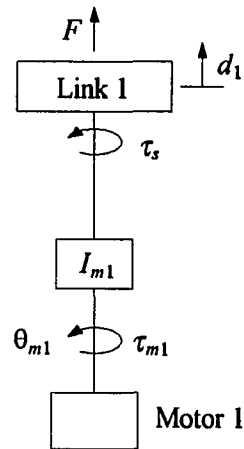


Figure 6.2: Schematic of actuator-transmission-load for link 1

For integration of the dynamic equations later, equation (6.18) above can be rewritten as

$$\tau_{m1} = I_{c1} \ddot{\theta}_{m1} + TR_1 \tau_1 \quad (6.19)$$

where $I_{c1} = I_{m1}$, $TR_1 = L_s$ and $\tau_1 = F_s$.

The transmission systems for joints 2 and 3, employ harmonic drives which are used as speed reducers with a speed reduction of 100 : 1. Motor shafts for joints 2 and 3 are connected to the input wave generators of the harmonic drives. In the case of joint 2, the output flexspline is directly connected to link 2. For joint 3 a timing belt and pulley are used to transmit the torque from the output flexspline of the harmonic drive to link 3. Figure 6.3 shows the schematic for joints 2 and 3. In this system, for $i = 2, 3$,

I_{mi} is the combined moments of inertia of the armature and motor shaft i

I_{wgi} is the moment of inertia of the input wave generator of harmonic drive i

$\dot{\tau}_i$ is the load torque at the input wave generator of harmonic drive i

τ_{mi} is the torque generated by motor i

τ_i is the load torque at the load side for link i

θ_{mi} is the angular displacement at motor shaft i

θ_i is the angular displacement for link shaft i

$N_i (N_i = 100)$ is the gear ratio of the harmonic drive for link i

Applying D'Alembert's principle to the model, we obtain

$$(I_{mi} + I_{wgi}) \ddot{\theta}_{mi} = \tau_{mi} - \dot{\tau}_i \quad (6.20)$$

The torque $\dot{\tau}_i$ and τ_i are related by

$$\frac{\dot{\tau}_i}{\tau_i} = \frac{\theta_i}{\theta_{mi}} = \frac{1}{N_i} = n_i \leq 1 \quad (6.21)$$

Substituting equation (6.21) into equation (6.20), the torque τ_{mi} generated by the motor i is expressed by

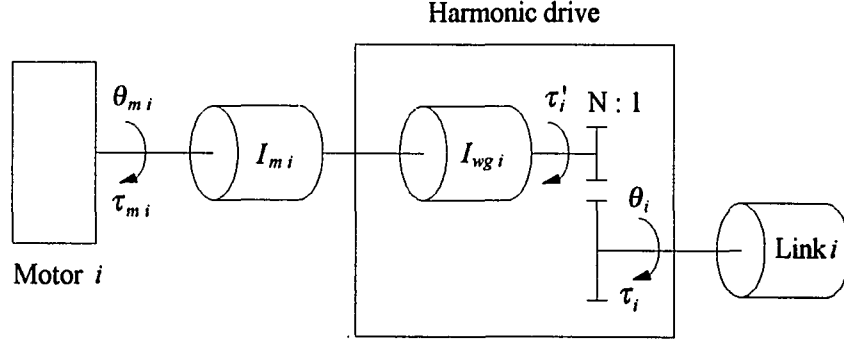


Figure 6.3: Schematic of motor-harmonic drive joint i , ($i = 2, 3$)

$$\tau_{mi} = (I_{mi} + I_{wgi})\ddot{\theta}_{mi} + n_i\tau_i \quad (6.22)$$

Equation (6.22) above can be rewritten as

$$\tau_{mi} = I_{ci}\ddot{\theta}_{mi} + TR_i\tau_i \quad \text{for } i = 2, 3 \quad (6.23)$$

where $I_{ci} = I_{mi} + I_{wgi}$, and $TR_i = n_i$.

Rewriting equations (6.19) and (6.23), the motor torque τ_{mi} reflected to the motor shaft for link i is given by

$$\tau_{mi} = I_{ci}\ddot{\theta}_{mi} + TR_i\tau_i \quad \text{for } i = 1, 2, 3 \quad (6.24)$$

6.3.2 Dynamic model with friction

The joint driving torques developed in section 6.1 for the case which the sampling manipulator is moving freely in its workspace can be written as

$$\tau = M(q)[\ddot{q}] + h[q, \dot{q}] + G \quad (6.25)$$

where $h[q, \dot{q}]$ is the 3×1 centrifugal and Coriolis force vector, and the joint variables are $[q_1 \ q_2 \ q_3]^T = [d_1 \ \theta_2 \ \theta_3]^T$.

The load torque τ_i at joint i can be expressed by

$$\tau_i = \tau_{fi} + \tau_{exi} + G_i \quad \text{for } i = 1, 2, 3 \quad (6.26)$$

where the inertia torque $\tau_{fi} = M_{ii}(q)[\ddot{q}_i]$, $M_{ii}(q)$ denotes the i th diagonal element of $M(q)$, G_i denotes the i th element of column vector G , and the explicit load torque τ_{exi} is a combination of coupling torques and centrifugal and Coriolis forces given by

$$\tau_{exi} = \sum_{\substack{j=1 \\ j \neq i}}^3 M_{ij}(q)[\ddot{q}_j] + h_i[q, \dot{q}] \quad (6.27)$$

where $M_{ij}(q)$ is the (i, j) th element of $M(q)$ and $h_i[q, \dot{q}]$ denotes the i th element of column vector of $h[q, \dot{q}]$.

The motors must overcome the friction torques as well as the torques identical in equation (6.26). The frictional force η_{FVi} for joint i is given by

$$\eta_{FVi} = \eta_{vsi} \dot{\theta}_{mi} + \eta_{fsi} \quad (6.28)$$

where η_{vsi} is the combined viscous damping coefficient for the joint, motor, and transmission system reflected to the motor shaft, and where η_{fsi} denotes the combined Coulomb friction and stiction.

Thus, from equations (6.24), (6.26), and (6.28), the required motor torque τ_{mi} reflected to the motor shaft for link i is given by

$$\tau_{mi} = I_{eqi} \ddot{\theta}_{mi} + \eta_{vsi} \dot{\theta}_{mi} + TR_i G_i + TR_i \tau_{exi} + \eta_{fsi} \quad \text{for } i = 1, 2, 3 \quad (6.29)$$

where $I_{eqi} = (I_{ci} + TR_i^2 M_{ii})$ is the equivalent inertia reflected to the motor shaft for link i .

Using the generalized coordinates $q_m = [q_{m1} \ q_{m2} \ \dots \ q_{mn}]$, equation (6.29) can be rewritten as

$$\tau_{mi} = I_{eqi} \ddot{q}_{mi} + \eta_{vsi} \dot{q}_{mi} + TR_i G_i + TR_i \tau_{exi} + \eta_{fsi} \quad \text{for } i = 1, 2, 3 \quad (6.30)$$

where $q_{mi} = \theta_{mi}$.

6.3.3 Integrated dynamic model

The motor dynamics were derived in Section 6.2. The dynamic equations for the actuator-transmission-load system were derived in the previous section, including the effect of friction. For the case which the sampling manipulator is moving freely in its workspace, the integrated dynamic equation of motion for link i is obtained by substituting equation (6.30) into (6.12).

$$I_{eqi} \ddot{q}_{mi} + \left[\eta_{vsi} + \frac{K_{bi} K_{mi}}{R_{ai}} \right] \dot{q}_{mi} = \frac{K_{mi}}{R_{ai}} V_{ai} - TR_i G_i - TR_i \tau_{exi} - \eta_{fsi} \quad \text{for } i = 1, 2, 3 \quad (6.31)$$

Eliminating the subscript i in equation (6.31), the integrated dynamic equations of motion for each joint of the manipulator can be simplified as

$$I_{eq} \ddot{q}_m + \left[\eta_{vs} + \frac{K_b K_m}{R_a} \right] \dot{q}_m = \frac{K_m}{R_a} V_a - TR G - TR \tau_{ex} - \eta_{fs} \quad (6.32)$$

where I_{eq} is the equivalent moment of inertia referred to the motor shaft, η_{vs} is the combined viscous damping coefficient referred to the motor shaft, TR is the reduction ratio, G is the gravitational force, τ_{ex} is the disturbance due to centrifugal, Coriolis and coupled inertia forces, and η_{fs} is the non-linear friction force.

7. PARAMETER IDENTIFICATION OF MANIPULATOR DYNAMICS

Existence of non-linearities in the manipulator joint drive generates serious problems due to the inaccuracies of motion planning and the difficulties of control system design. Friction is the major source of these non-linearities and causes steady state errors, undesired oscillations, and tracking errors. For accurate position and force control, the friction model must be added to the dynamic equations of motion of the manipulator. The dynamic parameters in the dynamic equations must be evaluated so that non-linearities are compensated in the control system. The velocity-dependent friction coefficients were evaluated from the experimental results. In addition, the gravity torque was evaluated.

In Section 7.1, experimental apparatus, setup, and procedures are presented. Section 7.2 demonstrates the experimental results for each drive joint: steady state velocity vs. input voltage. Section 7.3 presents the mathematical model for the identification of friction and gravitational torque. Identification results are presented in Section 7.4.

7.1 Experimental description

7.1.1 Experimental setup

Experiments were performed on a three degree of freedom remote robot manipulator developed at Iowa State University (described in Chapter 5). The first joint (prismatic joint) is driven by a DC servomotor through the ball screw (lead of 0.25 inch /rev) to lower and raise

the second and third arm. The second and last joints (rotary joints) are driven by DC servomotors through the harmonic drive gears (gear reduction of 100). An optical encoder (100 pulses /rev) as a position sensor is built on the back of each DC servomotor and provides the load angular positions.

Figure 7.1 shows the general experimental setup and apparatus used to obtain the angular displacements of the motor shafts for the given step input. A DC power supply (Electro-Craft, 50 V/ 25 Amps) was used to provide the step input to the DC servomotor according to the motor specifications, instead of supplying the step input from the robot controller through the PWM amplifier. To allow data acquisition of angular displacement signals from the encoder during the motion, an MIO-16 counter/timer (National Instruments, model MC-MIO-16 board) was used. Two out of three counters are used to count the number of pulses at each period of pulses generated by the encoder: one for pulses from the encoder, one for the source time base. The maximum resolution of the MIO-16 counter is 1- μ sec (in this work, 100- μ sec resolution was used). Data acquisition was conducted by an I/O controlled program.

7.1.2 Experimental procedures

An experiment was performed to measure the angular displacements of the motor shaft for joints of the sampling manipulator. Averaged velocities for the given step input voltages in steady state were obtained. A steady state velocity as a function of input voltage curve was used for evaluation of the dynamic parameters of the system. The experimental procedures are summarized as follows:

1. Lock the joints for the shoulder and upper arm at their desired locations except the joint for the forearm to be tested so that the effects due to the joint coupling can be neglected.
2. Apply step inputs of increasing values and measure the angular positions for each rotation

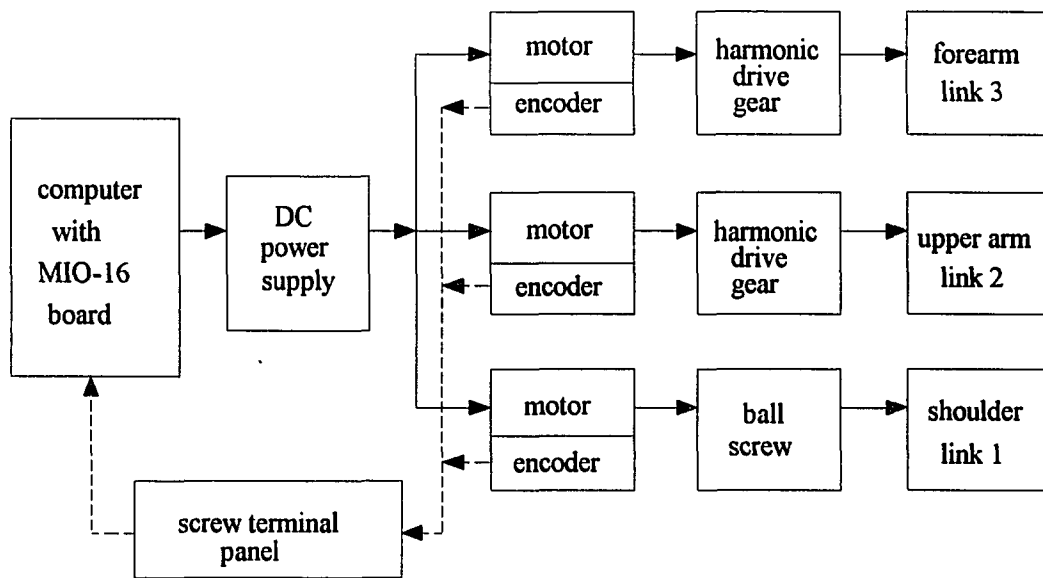


Figure 7.1: Schematic of measurement system for the three DOF manipulator located on the trailer

sense.

3. Calculate the averaged velocity in steady state for each step input.
4. Repeat step 1 through 3 by locking other joints except the joint to be tested until the shoulder joint is tested in sequence.
5. Use the steady state velocities obtained from the applied input voltages in order to evaluate the dynamic parameters from the integrated dynamic model (developed in previous chapter).

7.2 Experimental results

Experimental results were used to evaluate the dynamic parameters in the dynamic equations of motion for the three-axis sampling manipulator. A step input was applied to a motor to drive a joint to be tested. The angular position of the motor shaft was measured using an optical encoder. Its output was processed by a data acquisition system and stored in the direct memory of the computer while the joint was tested. A file storing data was created after moving the joint. An averaged velocity to a given step input was calculated in the steady state. Tests were repeated three times for each rotation sense at the same test conditions. Then, an averaged velocity to a given step input was obtained from the three test results.

Figures 7.2, 7.3, and 7.4 show the steady state velocity vs. input voltage curve of joints 3 (forearm), 2 (upper arm), and 1 (shoulder), respectively. In the figures, symbols denote the experimental data, and the solid lines denote the regression line drawn at the 95 % confidence level and extrapolated to the null velocity. The change of sign denotes the change of rotation of the motor (positive for clockwise and negative for counterclockwise). Non-linearities of the manipulator joints are demonstrated by the dead band shown in Figures 7.2, 7.3, and 7.4. The minimum input voltages to move the motor initially at rest are different for each rotation sense. The minimum inputs for joint 1 have the same sign regardless of the directional change of the motor. This implies that the sufficiently-positive control input must be provided to the

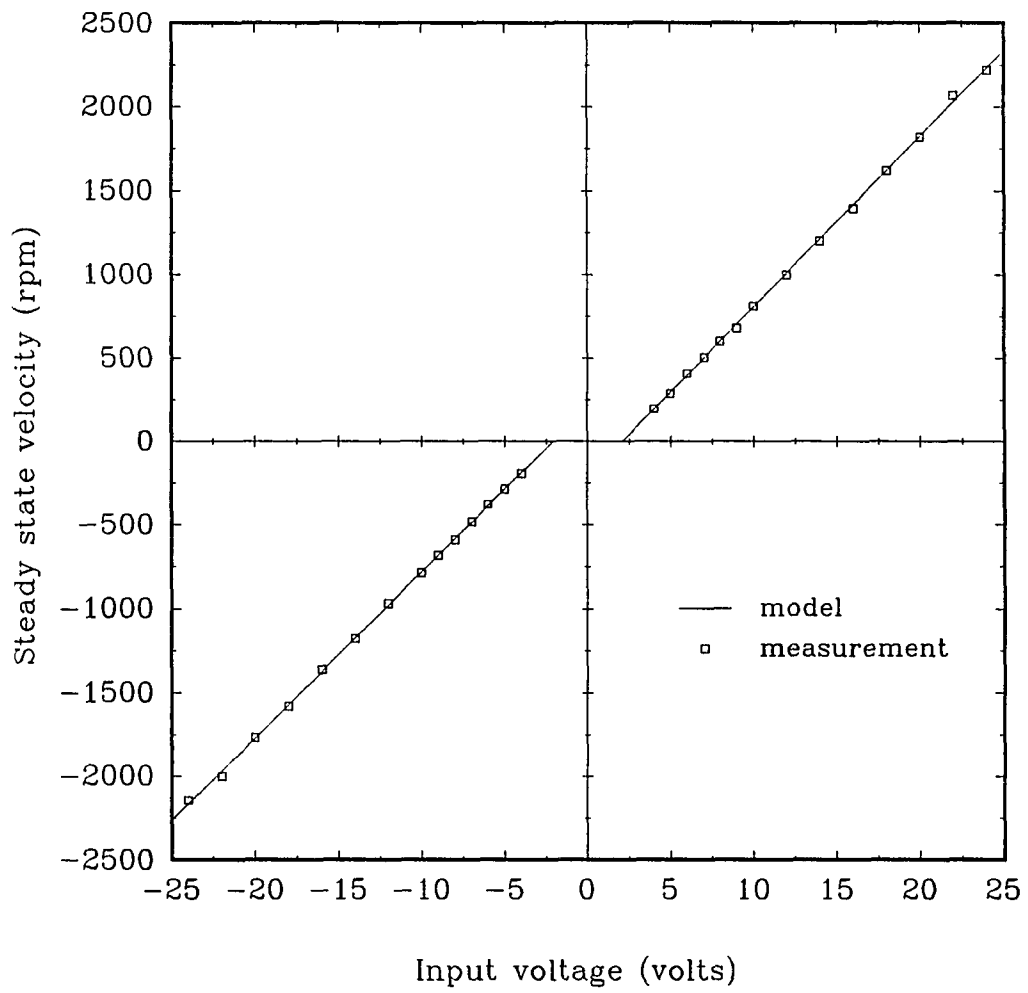


Figure 7.2: Steady state velocity vs. input voltage for joint of forearm

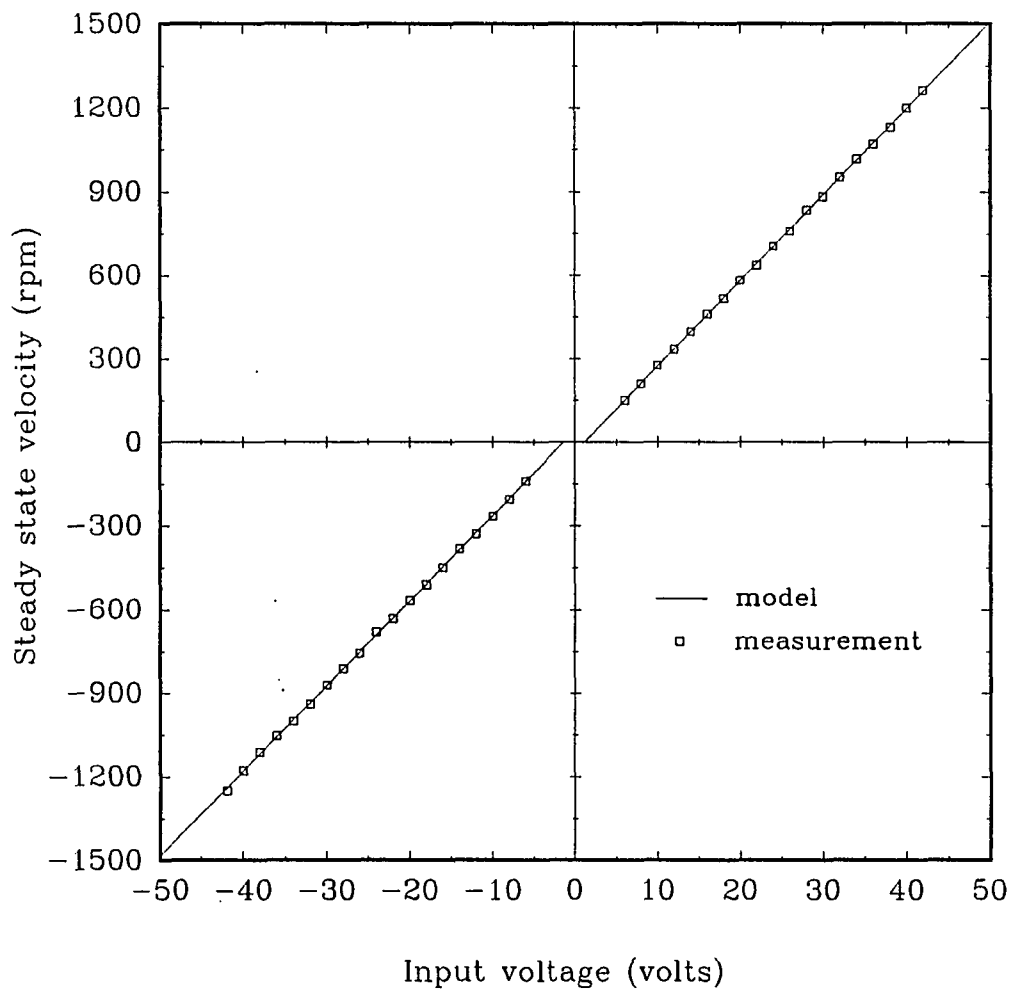


Figure 7.3: Steady state velocity vs. input voltage for joint of upper arm

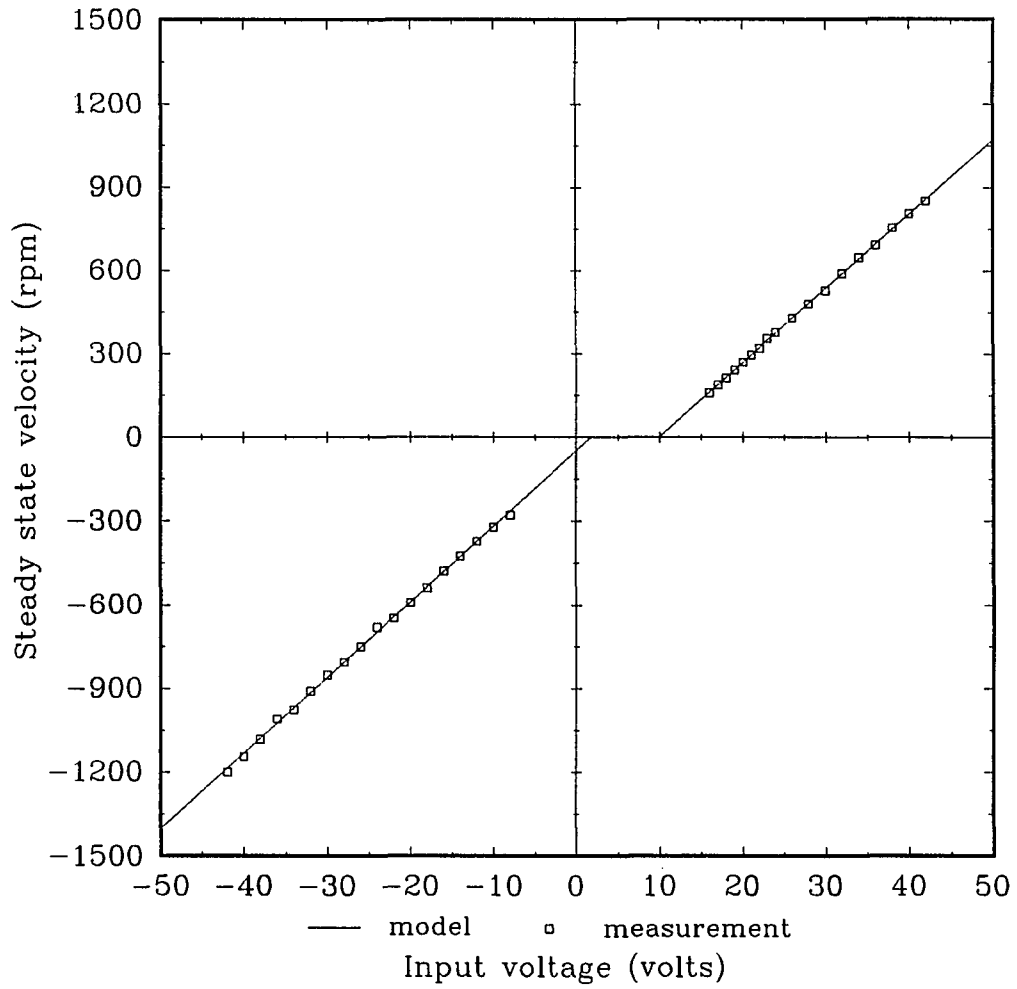


Figure 7.4: Steady state velocity vs. input voltage for joint of shoulder

motor in order to prevent the shoulder from descending due to gravity under the static equilibrium. Inspection of the steady state velocity vs. input voltage curve obtained from the experiment motivated the use of the friction model with combined viscous, dry, and static friction.

7.3 Mathematical model for identification

For parameter identification, only one joint to be tested is driven while the other joints are locked at their desired locations. Thus, the centrifugal and Coriolis accelerations due to the joint coupling vanish in the dynamic equation (6.36) derived in previous chapter. The dynamic equations for parameter identification can be written as

$$I_{eq} \ddot{q}_m + \left[\eta_{vs} + \frac{K_b K_m}{R_a} \right] \dot{q}_m = \frac{K_m}{R_a} V_a - TR G - \eta_{fs} \quad (7.1)$$

where q_m is the angular displacement of the motor shaft. Figure 7.5 shows the block diagram of the parameter identification system. Letting $\dot{q}_m = v$, equation (7.1) becomes

$$I_{eq} \dot{v} + \left[\eta_{vs} + \frac{K_b K_m}{R_a} \right] v = \frac{K_m}{R_a} V_a - TR G - \eta_{fs} \quad (7.2)$$

where \dot{v} is the time derivative of v .

The drive joints for the upper arm (joint 2) and forearm (joint 3) have no gravity effect since these arms have motion in the horizontal plane. Equation (7.2) can be simplified and rewritten as:

$$I_{eq} \dot{v} + \left[\eta_{vs} + \frac{K_b K_m}{R_a} \right] v = \frac{K_m}{R_a} V_a - \eta_{fs} \quad (7.3)$$

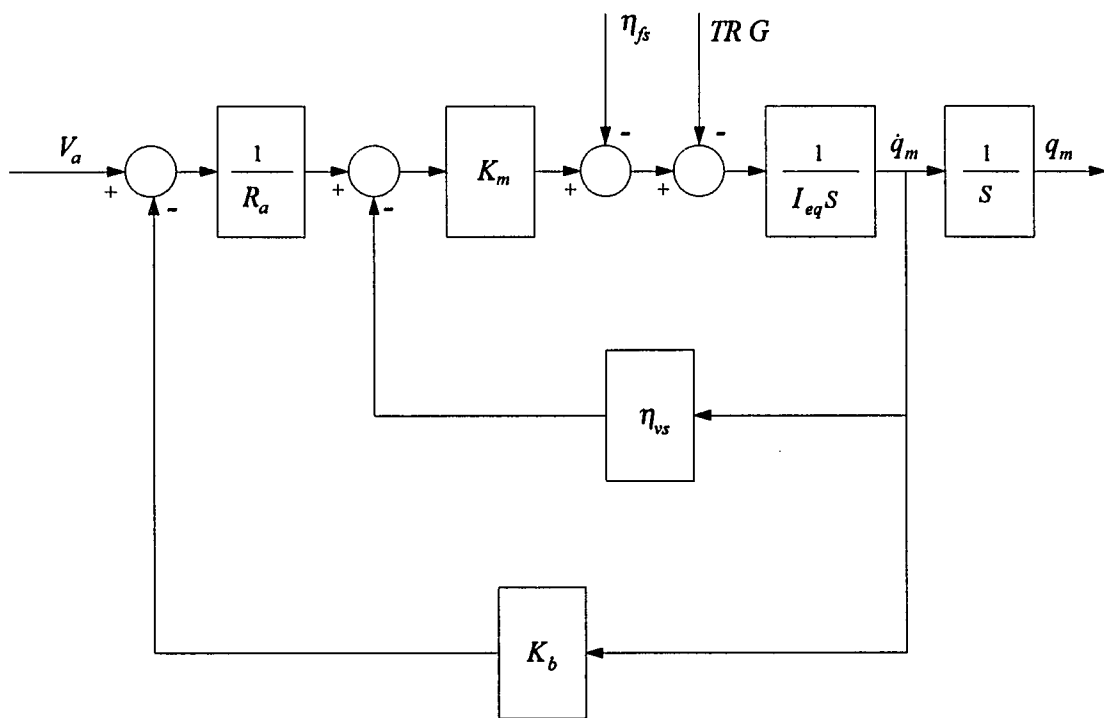


Figure 7.5: Block diagram of system model for parameter identification

Inspection of equation (7.3) reveals that the control input must increase and reach a sufficient value of static friction in order for the motor to begin to move from rest. From equation (7.3), we obtain the velocity dependent friction in the following:

$$\eta_{fs} = \frac{K_m}{R_a} V_A \quad (7.4)$$

where V_A is the minimum input voltage needed to move the motor initially at rest for each rotation sense and is shown in Figures 7.2 and 7.3 as a positive or negative value of dead band width .

The viscous damping coefficient η_{vs} can be determined from the steady state velocity vs. step input voltage. At steady state, equation (7.3) can be simplified and written as:

$$\eta_{vs} = \frac{1}{v_{ss}} \left[(V_a - K_b v_{ss}) \frac{K_m}{R_a} - \eta_{fs} \right] \quad (7.5)$$

Substituting equation (7.4) into (7.5), we obtain

$$\eta_{vs} = \frac{1}{v_{ss}} \left[(V_a - K_b v_{ss} - V_A) \frac{K_m}{R_a} \right] \quad (7.6)$$

Equation (7.6) can be simplified in terms of slope obtained from the steady state velocity vs. input voltage and written as:

$$\eta_{vs} = \left(\frac{1}{slope} - K_b \right) \frac{K_m}{R_a} \quad (7.7)$$

$$slope = \frac{V_a - V_A}{v_{ss}}$$

where *slope* is obtained from Figures (7.2), (7.3), and (7.4).

The drive joint 1 for the shoulder is affected by gravity. For the case of raising the shoulder, the control input must increase sufficiently to overcome the combined stiction and

gravitational force to move the motor initially at rest. For the case of lowering the shoulder, a positive control input must be provided to the motor to keep the static equilibrium condition. Otherwise, the shoulder will descend due to the gravity. Similarly, from equation (7.2), the combined non-linear friction and gravity torque for joint 1 can be derived as:

$$\eta_{fs} + TR G = \frac{K_m}{R_a} V_A \quad (7.8)$$

where V_A is the minimum input ($V_{A,up}$) needed to move the motor initially at rest for upward movement, or the positive input ($V_{A,down}$) needed to keep the static equilibrium condition for lower movement, as shown in Figure 7.4 for each rotation sense. The friction itself can be extracted from equation (7.8) by assuming that the magnitude of the friction is equal but has a change of sign for each rotation sense. The velocity dependent friction for joint 1 can be written as:

$$\eta_{fs} = \frac{1}{2} \Delta(V_A) \frac{K_m}{R_a} \quad (7.9)$$

$$\Delta(V_A) = V_{A,up} - V_{A,down}$$

where $\Delta(V_A)$ is the dead band width, as shown in Figure 7.4. Viscous damping coefficient for joint 1 is the same form as in the equation (7.7). From equation (7.8), the gravity torque for drive joint 1 can be written as:

$$TR G = \frac{1}{2} (V_{A,up} + V_{A,down}) \frac{K_m}{R_a} \quad (7.10)$$

where TR is the lead of the screw.

Although the friction and gravity torques can be identified separately from equations (7.9) and (7.10), it is not necessary to separate the friction from the combined left-side term in equation (7.10) since the friction and gravitational torque act as a disturbance to the dynamic

equations of motion for the manipulator. In this work, the stiction is taken as the average of Coulomb friction for each drive joint.

7.4 Identification results

Motor specifications (Appendix D) such as the armature winding resistance R_a , back emf K_b , and motor torque constant K_m are available from manufacturers. For each drive joint, the minimum input voltages needed to move the motor initially at rest, and the steady state velocity as function of input voltage are given from the experimental results. Thus, we can identify the dynamic parameters such as friction and gravity torque for each drive joint from (7.4), (7.7), (7.9), and (7.10). The identification results are summarized in Table 7.1 and the velocity dependent friction model for joint i can be written as:

$$\eta_{FVi} = \eta_{fsi} + \eta_{vsi} \dot{q}_{mi}$$

$$\eta_{FVi} = \begin{cases} \eta_{fpi} + \eta_{vpi} \dot{q}_{mi} & (\dot{q}_{mi} > 0) \\ \frac{\eta_{fpi} - \eta_{fni}}{2} \operatorname{sgn}(V_a) & (\dot{q}_{mi} = 0) \\ \eta_{fni} + \eta_{vni} \dot{q}_{mi} & (\dot{q}_{mi} < 0) \end{cases} \quad \text{for } i = 1, 2, 3 \quad (7.11)$$

where s may be p or n depending on the positive or negative velocity, respectively.

Table 7.1: Friction and gravity torque parameters for the manipulator
located on the trailer (number of joint, $i = 1, 2, 3$)

	Parameter	Joint 1 shoulder	Joint 2 upper arm	Joint 3 forearm
Coulomb friction (oz-in)	η_{fpi}	119.9266	33.5834	73.8532
	η_{fmi}	-119.9266	-39.5694	-73.0379
Viscous damping coefficient (oz-in-sec/rad)	η_{vpi}	1.39339	0.01148	0.36471
	η_{vmi}	1.25032	0.10179	0.47155
Stiction (oz-in)	$\frac{\eta_{fpi} - \eta_{fmi}}{2}$	119.9266	36.5764	73.4455
Gravity torque (oz-in)	$TR_i G_i$	171.1379	-----	-----

8. MOBILE ROBOTIC SAMPLING SYSTEM

A mobile robotic sampling system which eliminates human exposure to a hostile working environment will be used to take soil samples in the hazardous waste site and bring them to the field laboratory for contaminant analysis. A mobile robotic sampling system consists of a remote-controlled guide vehicle, robotic arm, sampling tools and soil recovery fixture. The remote-controlled guide vehicle is described in Chapters 3 and 4. The robotic arm, sampling tool and soil recovery fixture for a mobile robotic sampling system to be mounted on the remote-controlled guide vehicle are described in this Chapter.

In Section 8.1, the design concepts of the robotic arm, sampling tool, and soil recovery fixture are presented. Their configurations are presented in Section 8.2. The kinematic and dynamic analyses of the robotic arm of the guide vehicle are presented in Section 8.3 and 8.4, respectively. Section 8.5 presents the integrated dynamic model of the robotic arm for controller design. Finally, the overall work is summarized in Section 8.6.

8.1 Design considerations and specifications

The design considerations for the robotic arm of the remote-controlled guide vehicle include robot specification and configuration that is applicable to the vehicle. The robot specification and configuration include workspace and load capacity of the robot, number of degree of freedom, range of joint travel, and joint drive configuration. The design

considerations of the sampling tool and soil recovery fixture include configuration of the sampling tool to be connected to the end effector of the robot and the number of the sampling tools to be carried on the vehicle.

The workspace of the robotic arm of the guide vehicle must be determined by the payload space available to the vehicle. The workspace of the manipulator is constrained by the range of joint travel of the robotic arm. The mobile robotic sampling system must be capable of taking at least three samples per trip up to a maximum depth of 5.5 in (140 mm) below the ground. The manipulator must have a load capacity of 20 lbs (9.0 kg) in order to handle the sampling tool containing soil samples.

Configuration of the manipulator must be determined by motion, structural requirements, and control. The manipulator must have linear motion for positioning and continuous angular motion for sampling. Prismatic joints and rotary joints should be used for linear motion and angular motion, respectively. The manipulator must also have a rigid structure. The end of the manipulator arm must be able to pick up the sampling tools. Remote control should be employed to remotely control the manipulator due to the nature of the sampling task in the hazardous working environment. The manipulator needs to have simple kinematics and control equations. Simplified kinematics will allow the desired positions of the links for any end effector motion to be computed easily and quickly. Simplified control equations will reduce the burden of designing the controller for both accurate positioning of the end effector of the manipulator and compliant contact between the end effector and the environment.

The manipulator must be cost-effective and have at least three DOF in order to pick up the sampling tool and move it to a sampling location that is within the workspace of the arm. The manipulator, as configured (designed), must have maximum horizontal travel of 14.6 in. (370 mm) and maximum vertical travel of 13.0 in. (330 mm). Joints of the manipulator must

be driven by DC servomotors to have closed loop position and force control. In addition, guiding surfaces of prismatic joints must be covered to prevent the ingress of dust.

Sampling tools must be capable of taking soil samples as well as recovering samples of loose augered soils in a liner without losing the sample. These tools must be designed to be connected to the end of the robotic arm of the guide vehicle for sampling. The number of the sampling tools to be carried on the vehicle is limited by the workspace of the manipulator on the vehicle. The tool holder must be capable of holding the sampling tools when the vehicle is in motion.

Experiments were performed to measure the torque and thrust force required to take soil samples. For dry normal soil the torque required was about 15 lb-in (1.7 N-m). The measured torque was about 45 lb-in (5.1 N-m) for dry normal soil with rocks. The thrust force of about 10 lbs was required to penetrate the sampling tool into the soil. These torque and force values must be considered in selecting the motors for each drive joint.

8.2 Mechanical structure

8.2.1 Robotic arm on remote-controlled guide vehicle

Configuration of Cartesian type manipulator was selected based on the design considerations and specifications described in previous section. The robotic arm designed for the guide vehicle has two prismatic joints and one revolute joint in sequence. One DOF of each joint-link pair makes the robotic mechanism a three DOF manipulator. Figure 8.1 shows the three DOF manipulator for the vehicle along with covers. The first two prismatic joints of the manipulator have straight line motions in directions parallel to the Cartesian axes. Its prismatic orthogonal axes make it easy and quick to calculate the desired positions of the links because of the simple kinematic model and straightforward inverse kinematic solution. The

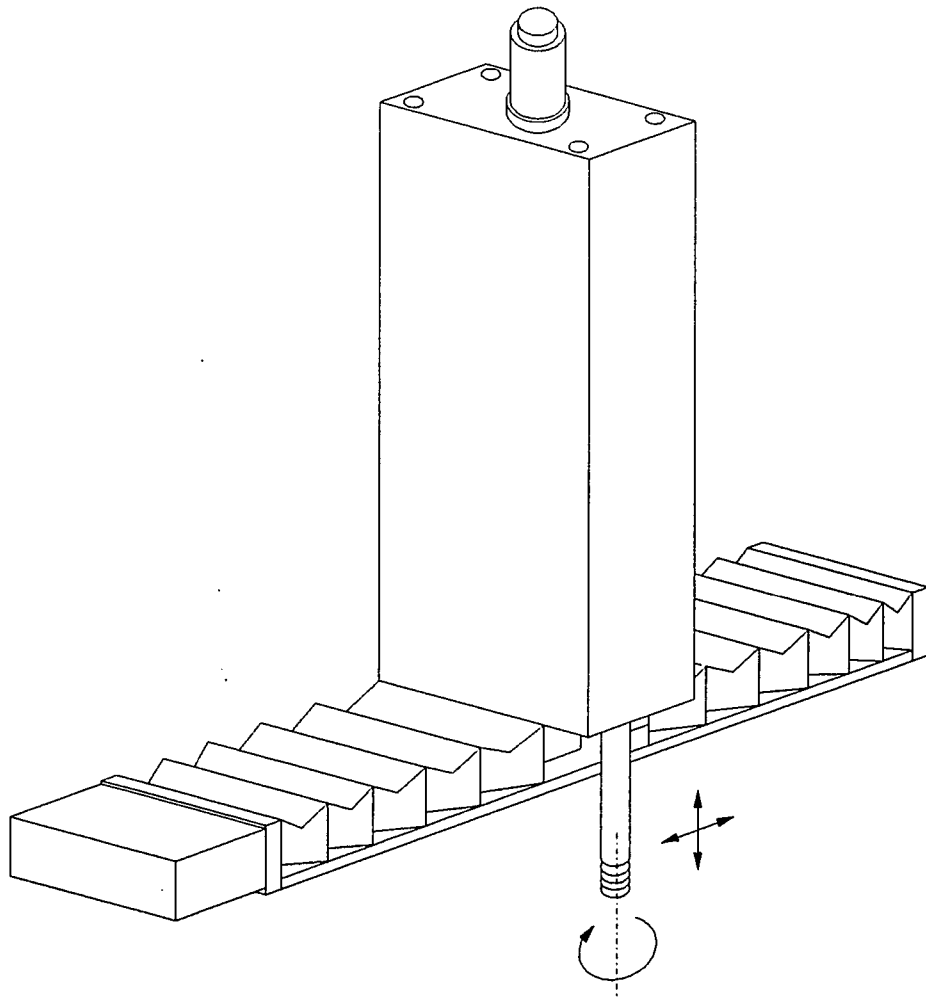
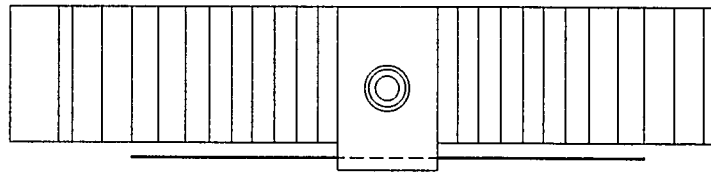


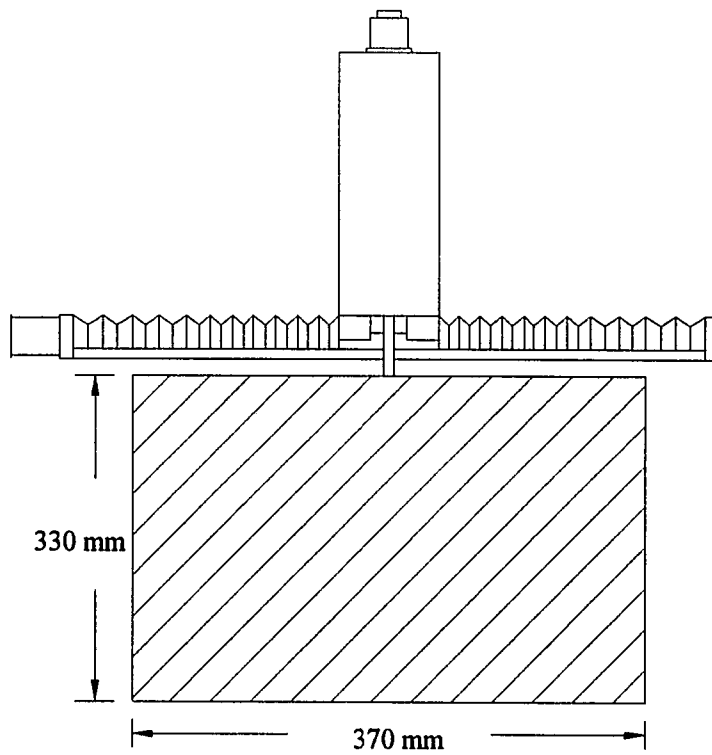
Figure 8.1: Manipulator on the guide vehicle

last revolute joint has rotational motion. The manipulator has the simple control equations since all its motion axes are dynamically decoupled (see equation (8.11)). The workspace of the manipulator is shown in Figure 8.2. The horizontal stroke was designed so that the end effector could accommodate three sampling tools. The vertical stroke was designed so that the sampling tool could reach the level 5.5 in (14 mm) below the ground during operation.

Figure 8.3 shows major mechanical components of the manipulator. Various parts in the figure have been numbered to achieve convenience in the description below. Detailed specifications of the mechanical components are provided in Appendix E. Shaft support rails (4) are used to support the guide shafts (5) on which linear bearings (6) for link 1 (1) are placed to prevent the guide shafts from bending under load. They are made out of aluminum alloy and provide high rigidity. The ball screw drives (7) capable of converting rotary motion produced by the servomotor to linear motion is used to move links 1 and 2 (2). The ball screw assembly comprises a ball screw shaft and ball nut. Linear bearings (6 and 8) are used to allow the translational motions of links 1 and 2. A cylindrical pair bearing (9) is used to allow combined translational and rotary motion of link 3 (3). Bellows (10) are used to prevent the ball screw drive system and guide shafts for link 1 from the ingress of dust. The arm end (11) of the manipulator has screw-type configuration so that it can pick up the sampling tool which has a nut-type configuration at its top. DC servomotors (12) are used to drive each joint of the manipulator. The motor shafts for joints 1 and 2 are directly connected to the screw end. The motor shaft for joint 3 is connected to the shaft end through a harmonic drive gear (13) to produce a high torque. Incremental encoders (14) are used to provide linear or angular positions of the links of the manipulator. These are mounted on the back of each DC servomotor.



a) Top view



b) Front view

Figure 8.2: Workspace of the manipulator on the guide vehicle

8.2.2 Sampling tool and soil recovery fixture

An auger type sampling tool was selected to take the soil samples. A commercially available wood drill bit (one inch in diameter, IRWIN Co.) was modified for the robotic soil sampling. Figure 8.4 shows the modified sampling tool and soil recovery fixture. Various parts in the figure have been numbered to achieve convenience for its description below. The soil recovery fixture made of aluminum holds the sampling tools and soil recovery liners (9). The blade (1) of the wood drill bit was enlarged by a sharpened metallic piece welded to the drill. Standard aluminum tubing (3) is mounted on the body of the wood drill bit in order to hold the soil within the grooves of the drill bit. The end (6) of the auger type sampling tool has internal threads which help in connecting to the end of the robotic end effector which has threads (11, in Figure 8.3). However, the connection requires rotation of the end effector, whereas the sampling tool should be stationary. This is achieved by inserting a cylindrical shaft (5) through the sampling tool as shown in Figure 8.4 (a). This shaft is held in place by a cavity (7) made for it in the soil recovery fixture as shown in Figure 8.4 (b).

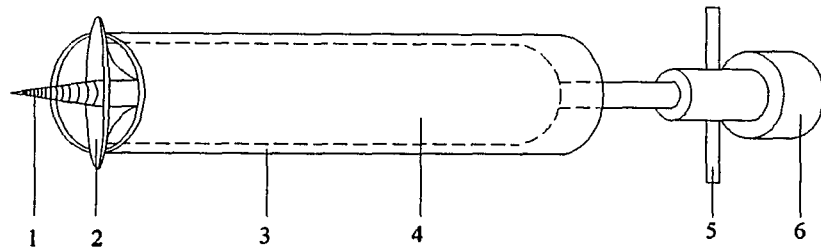
8.3 Analysis of robotic arm on remote-controlled guide vehicle

8.3.1 Coordinate frame assignment

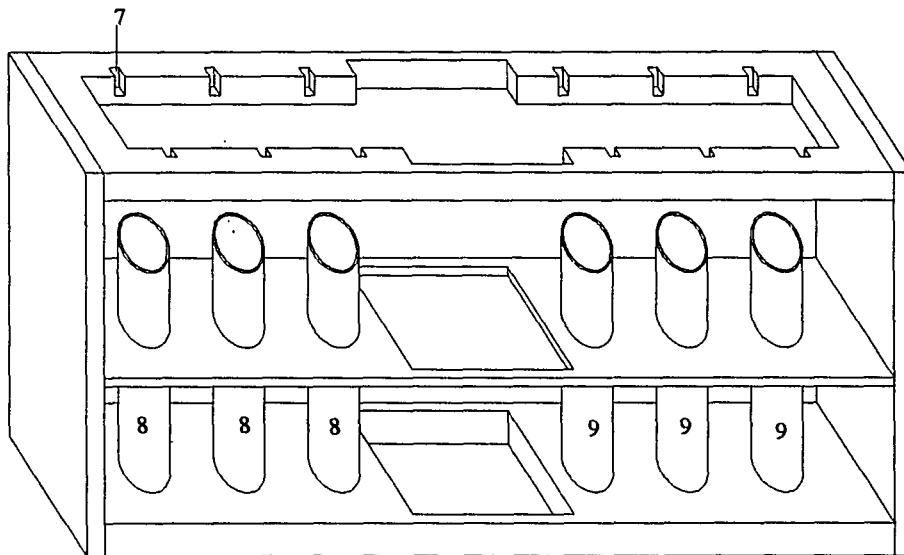
The link coordinate frames are assigned to links of the manipulator of the remote-controlled guide vehicle by the modified Denavit-Hartenberg notation (refer to Appendix A), as shown in Figure 8.5. Figure 8.6 shows the kinematic parameters and coordinate frame assignments. The D-H parameters are given in Table 8.1.

8.3.2 Forward kinematics

The transformation matrices describing the link frames for the manipulator are as follows:



a) Sampling tool



b) Soil recovery fixture

1: Pilot 2: Blade 3: Tube 4: Wood drill bit 5: Cylindrical shaft
 6: Nut-type end 7: Cavity 8: Tool holder 9: Soil recovery liner

Figure 8.4: Sampling tool and soil recovery fixture

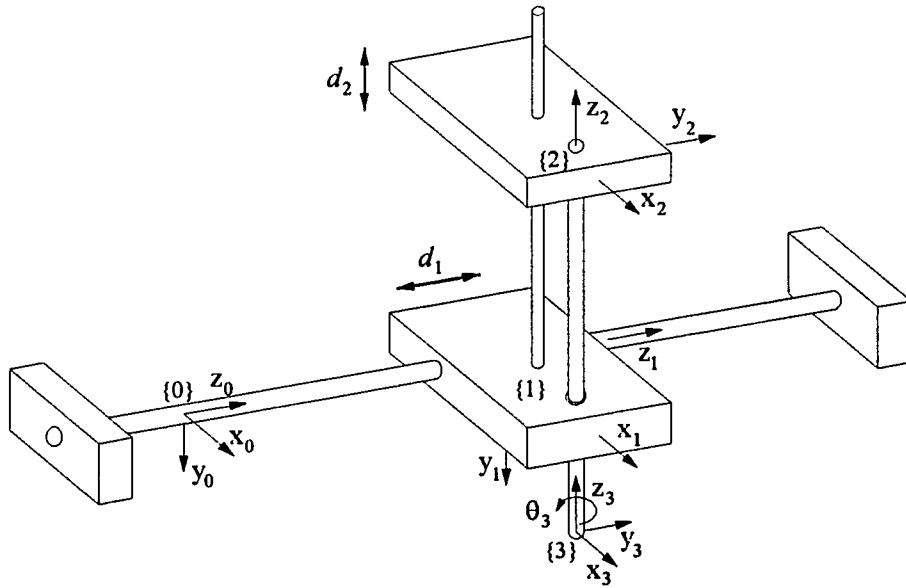


Figure 8.5: Schematic of the three DOF manipulator on the guide vehicle

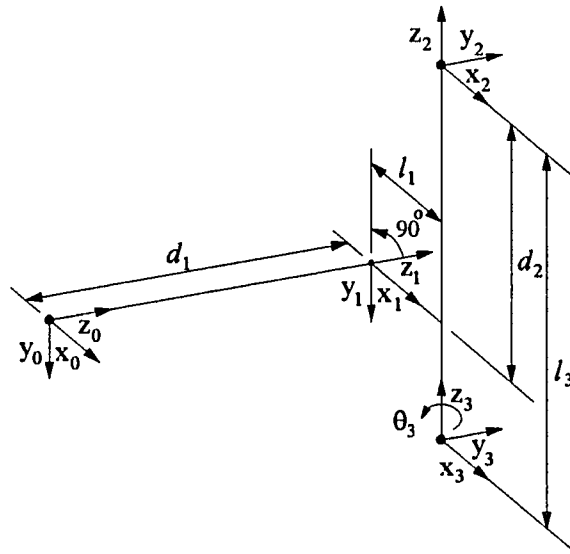


Figure 8.6: Link coordinate frame assignments of the manipulator on the guide vehicle

Table 8.1: D-H parameters for the manipulator on the guide vehicle

i	a_{i-1}	α_{i-1}	d_i	θ_i
1	0	0	d_1	0
2	l_1	90°	d_2	0
3	0	0	$-l_3$	θ_3

$${}^0T_1 = \begin{pmatrix} 1 & 0 & 0 & 0 \\ 0 & 1 & 0 & 0 \\ 0 & 0 & 1 & d_1 \\ 0 & 0 & 0 & 1 \end{pmatrix} \quad (8.1)$$

$${}^1T_2 = \begin{pmatrix} 1 & 0 & 0 & l_1 \\ 0 & 0 & -1 & -d_2 \\ 0 & 1 & 0 & 0 \\ 0 & 0 & 0 & 1 \end{pmatrix} \quad (8.2)$$

$${}^2T_3 = \begin{pmatrix} C_3 & -S_3 & 0 & 0 \\ S_3 & C_3 & 0 & 0 \\ 0 & 0 & 1 & -l_3 \\ 0 & 0 & 0 & 1 \end{pmatrix} \quad (8.3)$$

where $S_3 \equiv \text{Sin}(\theta_3)$ and $C_3 \equiv \text{Cos}(\theta_3)$.

The description of the position and orientation of frame $\{3\}$ relative to the base frame $\{0\}$ is given by

$${}^0_3T = \begin{bmatrix} C_3 & -S_3 & 0 & l_1 \\ 0 & 0 & -1 & l_3 - d_2 \\ S_3 & C_3 & 0 & d_1 \\ 0 & 0 & 0 & 1 \end{bmatrix} \quad (8.4)$$

From equation (8.4), the end point position of the manipulator relative to the base frame $\{0\}$ is given by

$${}^0_3P = [l_1 \ l_3 - d_2 \ d_1]^T \quad (8.5)$$

Given the position of the sampling tool tip relative to the frame $\{3\}$ as ${}^3P_{\text{tool tip}} = [0 \ 0 \ -l_4]^T$, the position of the tool tip relative to the base frame $\{0\}$ is expressed by

$${}^0P_{\text{tool tip}} = [l_1 \ l_3 + l_4 - d_2 \ d_1]^T \quad (8.6)$$

8.3.3 Inverse kinematics

The joint variables ($d_1, d_2,$ and θ_3) for the given position and orientation 0_3T of the manipulator end point are determined by the following equations:

$${}^0_3T = \begin{bmatrix} r_{11} & r_{12} & r_{13} & P_x \\ r_{21} & r_{22} & r_{23} & P_y \\ r_{31} & r_{32} & r_{33} & P_z \\ 0 & 0 & 0 & 1 \end{bmatrix} \quad (8.7)$$

$$d_1 = P_z$$

$$d_2 = l_3 - P_y \quad (8.8)$$

$$\theta_3 = A \tan(r_{31}, r_{32})$$

8.3.4 Jacobians

The manipulator jacobian is used to analyze the motion of the manipulator. For the manipulator of the guide vehicle, the Jacobian matrix 0J written in the base frame $\{0\}$ is given by

$${}^0J = \begin{bmatrix} 0 & -1 \\ 1 & 0 \end{bmatrix} \quad (8.9)$$

The Jacobian 3J written in terms of frame $\{3\}$ is given by

$${}^3J = \begin{bmatrix} S_3 & 0 & 0 \\ C_3 & 0 & 0 \\ 0 & 1 & 0 \end{bmatrix} \quad (8.10)$$

8.3.5 Dynamics

For the case which the manipulator on the guide vehicle is moving freely in its workspace, the dynamic behavior of the manipulator can be described by the following equation (refer to Appendix B.1):

$$\tau = M\ddot{q} + G \quad (8.11)$$

where

$\tau = [\tau_1, \tau_2, \tau_3]^T$ is the 3 x 1 vector of the actuator torques,

q is the generalized coordinates (or position variables),

$q_1 = d_1, q_2 = d_2, q_3 = \theta_3$, and $\ddot{q} = [\ddot{d}_1 \ \ddot{\theta}_2 \ \ddot{\theta}_3]^T$,

M is the mass matrix which is symmetric and positive definite,

G is the gravity force vector which is independent of joint variables,

and where

$$M = \begin{bmatrix} m_1 + m_2 + m_3 & 0 & 0 \\ 0 & m_2 + m_3 & 0 \\ 0 & 0 & I_{3,33} \end{bmatrix} \quad (8.12)$$

$$G = [0 \ (m_2 + m_3)g \ 0]^T \quad (8.13)$$

The dynamic equations of motion of the manipulator of the guide vehicle are simplified since all its motion axes are dynamically decoupled, as described in equation (8.11). Centrifugal and Coriolis acceleration forces due to joint coupling disappear.

For the case in which the external force $F = [f_x \ f_y \ f_z]^T$ is exerted by the environment on the arm end of the manipulator, equation (8.11) can be expressed as

$$\tau = M\ddot{q} + G + {}^3J^T F \quad (8.14)$$

where 3J is the Jacobian for the manipulator as written in equation (8.10).

8.4 Integrated dynamic model

8.4.1 Dynamics of actuator-transmission-load system

The dynamic equations of motion for the integrated actuator-transmission-load system are derived with the assumption that the manipulator is a jointed rigid body. In addition, the joint elasticity of the transmission systems is not taken into account.

Ball screws are used as the transmission elements for links 1 and 2 and a harmonic drive as speed reducer for joint 3. Referring to Section 6.3.1, the motor torque reflected to the motor shaft for link i is expressed by

$$\tau_{mi} = I_{eqi} \ddot{q}_{mi} + TR_i G_i \quad \text{for } i = 1, 2, 3 \quad (8.15)$$

and

$$\begin{aligned}
d_1 &= TR_1 q_{m1} \\
d_2 &= TR_2 q_{m2} \\
q_3 &= TR_3 q_{m3}
\end{aligned} \tag{8.16}$$

where

$$\begin{aligned}
I_{eq1} &= I_{m1} + TR_1^2 M_{11} \\
I_{eq2} &= I_{m2} + TR_2^2 M_{22} \\
I_{eq3} &= I_{m3} + I_{wg} + TR_3^2 M_{33}
\end{aligned} \tag{8.17}$$

and where

τ_{mi} is the torque generated by motor i ,

q_{mi} is the angular displacement at motor shaft i ,

I_{eqi} is the equivalent moment of inertia referred to motor shaft i ,

I_{mi} is the combined moments of inertia of the armature and motor shaft i ,

I_{wg} is the moment of inertia of the input wave generator of harmonic drive,

TR_1 and TR_2 are the lead of the screw for links 1 and 2, respectively,

TR_3 is the gear ratio of the harmonic drive for link 3,

M_{ii} denotes the i th diagonal element of M ,

G_i denotes the i th element of column vector G .

The motor must overcome the friction torque as well as the inertia torque and gravitational torque. The frictional force η_{Fi} for joint i is given by

$$\eta_{Fi} = \eta_{fvi} \dot{q}_{mi} + \eta_{fni} \tag{8.18}$$

where the first term denotes the viscous friction where η_{vsi} is the combined viscous damping coefficient of joint, motor, and transmission element reflected to the motor shaft, and where

the second term denotes the non-linear friction. Including the friction force, equation (8.15) can be written as

$$\tau_{mi} = I_{eqi} \ddot{q}_{mi} + \eta_{fvi} \dot{q}_{mi} + TR_i G_i + \eta_{fni} \quad \text{for } i = 1, 2, 3 \quad (8.19)$$

8.4.2 Integrated dynamics

Combining the motor dynamics equation (6.15) derived in Section 6.2 into equation (8.19), we obtain the integrated dynamic model of the robotic arm of the guide vehicle in the following form:

$$I_{eqi} \ddot{q}_{mi} + \left[\eta_{fvi} + \frac{K_{bi} K_{mi}}{R_{ai}} \right] \dot{q}_{mi} = \frac{K_{mi}}{R_{ai}} V_{ai} - TR_i G_i - \eta_{fni} \quad \text{for } i = 1, 2, 3 \quad (8.20)$$

where V_{ai} is the applied voltage to the armature terminals of the motor i , R_{ai} is the armature winding resistance, K_{mi} is the motor torque constant, and K_{bi} is the back emf constant.

8.5 Summary

The robotic arm of the guide vehicle, sampling tool, and soil recovery fixture for the mobile robotic sampling system have been designed and specified in this chapter. The kinematic and dynamic analyses of the manipulator mounted on the guide vehicle have been described. The integrated dynamic model of the manipulator including the motors, transmission elements, and friction, has been derived. This integrated dynamic model should be used to design the controller of the manipulator. The dynamic parameters in the dynamic equations can be identified using the similar method described in Chapter 7. The number of soil samples per trip of the vehicle could be increased by adding one more DOF to the manipulator at the cost of increased production expenses.

9. CONCLUSIONS AND FUTURE WORK

The primary justification for this research was to provide a means of eliminating or significantly reducing worker exposure to the hazardous working environment in taking soil samples for contaminant analysis from hazardous waste sites. The objectives of this research were to design and construct the remote-controlled guide vehicle to move the robotic sampling unit (a trailer) into the contaminated field to assist in obtaining soil samples at the desired locations, to develop the integrated dynamic model of the remote manipulator located on the trailer, to develop the identification method of determining the dynamic parameters in the integrated dynamic model, and to design and analyze the mobile robotic sampling system for the guide vehicle. The conclusions of this study and recommendations for future work are summarized in this chapter.

9.1 Conclusions

The remote-controlled guide vehicle was designed, constructed, and demonstrated to be operable by either radio control or umbilical cable. The vehicle has a 700 pounds payload capacity, an 8.4 horsepower capability, and a 12 square foot platform for sampling equipment and other payload. The lateral and turning stability of the remote-controlled vehicle can be ensured by adjusting the center of mass of the vehicle. This can be easily accomplished by arranging the equipment and ballast on the double platform specifically designed into the vehicle. The field test with the teleoperated control demonstrated that the vehicle may

encounter difficulties in returning to the base site due to entanglement with the umbilical cables or in performing tasks due to the possible damage of the cables. The radio control designed for the vehicle solved the problems associated with the teleoperated control and improved the operating range of the vehicle. The field test results verify that the remote-controlled guide vehicle is capable of successfully performing the tasks of guiding the robotic sampling system (a trailer) into the desired sampling site, or carrying a separate onboard robotic sampling system for obtaining soil samples (a mobile robotic sampling system).

The forward kinematics, inverse kinematics, Jacobians, and dynamics of the remote manipulator located on a trailer and pulled by the guide vehicle were analyzed. The integrated dynamic model for the manipulator and its drive system was developed to reduce modeling error in the robotic system. An identification method, based on measurements of the steady state velocity to a given step input for each joint of the manipulator, was developed to experimentally determine the friction and gravitational torque parameters in the integrated dynamic model. The dynamic parameters such as velocity-dependent friction and torque effect due to gravity were determined. The integrated dynamic model with its known parameter values will be useful for developing a manipulator control system capable of performing the sampling tasks involving soil sampler positioning and compliant contact between the soil sampler and the soil surface.

The mobile robotic sampling system utilizing the remote-controlled guide vehicle was designed to take soil samples in the hazardous waste sites and bring them to the field laboratory, independent of the manipulator on the trailer. The robotic arm, sampling tool, and soil recovery fixture for the mobile robotic sampling system was designed to be mounted on the remote-controlled guide vehicle. All motion axes of the robotic arm designed were dynamically decoupled to eliminate the effect of joint coupling, resulting simple kinematics and control equations. The kinematics and dynamics of the robotic arm were analyzed. The

integrated dynamic model for the robotic arm and its drive system was also developed for the control system. The auger-type soil sampling tool was designed to be connected to the end of the robotic arm and to have sufficient torque to adequately sample a variety of soils varying from sod to rock/soil mixtures.. The soil recovery fixture was designed to hold the sampling tools as well as retain any loose soil sample in the soil recovery liner.

9.2 Recommendations for future work

As a result of this research, several issues have been encountered which must be investigated and solved to successfully accomplish the sampling task in hazardous waste sites by eliminating or reducing worker exposure to the hazardous environment. The recommendations for future work are summarized below.

- A video system is recommended to remotely monitor and control the operations of the remote-controlled guide vehicle from a distance. This includes the installation of appropriate cameras on the vehicle.
- The remote-controlled guide vehicle controlled by the operator should be modified to be an automated guided vehicle (AGV) to be autonomously controlled. To achieve higher performance of the sampling task the AGV can be used to tow or carry a sampling system with a robot. This research should include the development of a real-time control system for AGV direction, speed, path planning and decision with use of appropriate sensory devices.
- The robot described in this dissertation and used for the soil sampling is required to perform complex tasks involving soil sampler (end effector) positioning, and compliant contact between the soil sampler and the soil to be sampled. Using the integrated dynamic model and its known parameter values, design and implementation of the compliant motion control system for the robot is recommended. This will be necessary for the robot

to successfully accomplish the sampling task in the face of uncertainties and variations in its work environment.

- The mobile robotic sampling system (designed and described in this dissertation) utilizing the remote-controlled vehicle or AGV is recommended to be constructed to obtain soil samples for the contaminated soil analysis. The three DOF robotic arm designed for the mobile robotic sampling system is recommended to be redesigned to increase the number of soil samples per sampling mission to increase the efficiency of each mission.

BIBLIOGRAPHY

- [1] Engineering News Record, "EPA proposes 22 new Superfund sites." Vol. 9, No. 6, p.5, 1991.
- [2] Jenkins, T. "Hazardous Waste Cleanup: How Much and Who will Pay?" Walker's Estimating and Construction Journal, pp. 6-7, Fall 1989.
- [3] Anderson, M. S., Jaselskis, E. J. "Mobile Instrumentation Platform and Robotic Accessory for Real-Time Screening of Hazardous Waste." SPECTRUM '92, International Tropical Meeting, Nuclear and hazardous Waste Management, Boise, Idaho, Vol. 1, pp. 81-85, August, 1992.
- [4] Vannette, M. W. "The Design of a SCARA Robotic Arm for Hazardous Waste Surface Sampling." Master's Thesis, Iowa State University, 1992.
- [5] Fassel, V. A. "Simultaneous or Sequential Determination of the Elements at all Concentration Levels - the Renaissance of an Old Approach." Analytical Chemistry ICP-AES, pp. 60-63, November 1979.
- [6] Kim, K., Soni, R., You, S., and Hall, J. L. "Automated Guided Vehicle for Robotic Sampling in Hazardous Waste Sites." Twenty-ninth Annual Power Affiliate Report, ISU-ERI-Ames 92108, Iowa State University, May 1992.
- [7] Kim, K., You, S., and Hall, J. L. "Remote-Controlled Vehicle for Robotic Sampling in Hazardous Waste Sites." Thirtieth Annual Power Affiliate Report, ISU-ERI-Ames 93087, Iowa Sate University, May 1993.

- [8] Zollinger, W. T. and Dyches, G. M. "Surface Decontamination Using a Teleoperated Vehicle and Kelly Spray/Vacuum System." 5th Int. Symposium on Ceramics in Nuclear and Hazardous Waste Management, Cincinnati, OH, April 28-May 2, 1991.
- [9] Fogle, R. F. and Heckendorn, F. M. "Teleoperated Equipment for Emergency Response Applications at the Savannah River Site." *Journal of Robotics Systems*, pp. 169-185, vol. 9, March 1992.
- [10] Goldenberg, A. A., Wiercienski, J., Kuzan, P., Szymczy, C., Fenton, R. G., and Shaver, B. "A Remote Manipulator for Forestry Operations." *Proceedings of the 1992 IEEE, International Conference on Robotics and Automation, Nice, France*, pp. 2792-2794, May 1992.
- [11] Smith, F. M., Backman, D. K., and Jacobsen, S. C. "Telerobotic Manipulator for Hazardous Environments." *Journal of Robotic Systems*, pp. 251-260, vol. 9, March 1992.
- [12] Craig, J. J. "Introduction to Robotics: Mechanics and Control." Addison Wesley Publishing Company, Reading, MA, 1989.
- [13] Gomes, S. C. P., and Chetien, J. P. "Dynamic Modelling and Friction Compensated Control of a Robot Manipulator Arm." *Proceedings of the 1992 IEEE, International Conference on Robotics and Automation, Nice, France*, pp. 1429-1435, May 1992.
- [14] Armstrong-Helouvry, B. "Stick-Slip Arising from Stribeck Friction." *Proceedings of the 1990 IEEE, International Conference on Robotics and Automation, Cincinnati, OH*, pp. 1377-1382, May 1990.
- [15] Armstrong-Helouvry, B. "Frictional Lag and Stick-Slip." *Proceedings of the 1992 IEEE, International Conference on Robotics and Automation, Nice, France*, pp. 1448-1453, 1992.

- [16] Dupont, P. E. "Friction Modeling in Dynamic Robot Simulation." Proceedings of the 1990 IEEE, International Conference on Robotics and Automation, Cincinnati, OH, pp. 1370-1376, May 1990.
- [17] Dupont, P. E. "Avoiding Stick-Slip in Position and Force Control through Feedback." Proceedings of the 1991 IEEE, International Conference on Robotics and Automation, Sacramento, CA, pp. 1470-1475, April 1991.
- [18] Rajan, V. T., Burrige, R., and Schwartz, J. T. "Dynamics of a Rigid Body in Frictional Contact with Rigid Walls: Motion in Two Dimensions." Proceedings of the 1987 IEEE, International Conference on Robotics and Automation, Raleigh, NC, pp. 671-677, 1987
- [19] Mason, M. T., and Wang, Y. "On the Inconsistency of Rigid-Body Frictional Planar Mechanics." Proceedings of the 1988 IEEE, International Conference on Robotics and Automation, Philadelphia, PA, pp. 524-528, April 1988.
- [20] Dupont, P. E. "The Effect of Coulomb Friction on the Existence and Uniqueness of the Forward Dynamic Problem." Proceedings of the 1992 IEEE, International Conference on Robotics and Automation, Nice, France, pp. 1470-1475, May 1992.
- [21] Armstrong, B. "Friction: Experimental Determination, Modeling and Compensation." Proceedings of the 1988 IEEE, International Conference on Robotics and Automation, Philadelphia, PA, pp. 1422-1427, April 1988.
- [22] Kubo, T., Anwar, G., and Tomizuka, M. "Application of Nonlinear Friction Compensation to Robot Arm Control." IEEE Trans., Robotics and Automation, pp. 722-727, San Francisco, CA, April 1986.
- [23] Donath, M. and Gogoussis, A. "Coulomb Friction Effects on the Dynamics of Bearing and Transmissions in Precision Robot Mechanism." Proceedings of the 1988 IEEE, International Conference on Robotics and Automation, Philadelphia, PA, pp. 1440-1446, April 1988.

- [24] Townsend, W. T. and Sailsbury, J. K. "The Effect of Coulomb Friction and Stiction on Force Control." Proceedings of the 1987 IEEE, International Conference on Robotics and Automation, Raleigh, NC, pp. 883-889, 1987.
- [25] Donath, M. and Gogoussis, A. "Coulomb Friction Joint and Drive Effects in Robot Mechanisms." Proceedings of the 1987 IEEE, International Conference on Robotics and Automation, Raleigh, NC, pp. 828-836, 1987.
- [26] Huston, J. C. and Graves, B. "Three Wheeled Vehicle Dynamics." Dynamics of Recreational Vehicles SP-509, Society of Automotive Engineers, Feb. 1982.
- [27] Ellis, J. R. "Vehicle Dynamics." Business Books, London, 1969.
- [28] Kazerrooni, H., Sheridan, T., and Houpt, P. K. "Design Method for Robust Compliant Motion for Robot Manipulators." IEEE Journal on Robotics and Automation, pp. 93-105, June, 1986.
- [29] Hogan, N. "Impedance Control: An Approach to Manipulation, Part 1: Theory, Part 2: Implementation, Part 3: Application." ASME Journal of Dynamic Systems, Measurement, and Control, vol. 107, pp. 1-24, March, 1985.
- [30] Salisbury, K. J. "Active Stiffness Control of Manipulator in Cartesian Coordinates." Proceedings of the 19th IEEE Conference on Decision and Control, Albuquerque, New Mexico, pp. 95-100, 1980.
- [31] Yoshikawa, T. "Foundations of robotics: Analysis and Control." The MIT Press, Cambridge, Massachusetts, 1990.
- [32] Koivo, A. J. "Fundamentals for Control of Robotic Manipulators." John Wiley & Sons, New York, NY, 1989.
- [33] Klafter, R. D., Chmielewski, T. H., and Negin, M. "Robotic Engineering." Prentice Hall, Englewood Cliffs, NJ, 1989.

- [34] Luh, J. Y. S. "Conventional Controller Design for Industrial Robots - A Tutorial." IEEE Transactions on Systems, Man, and Cybernetics, vol. SMC-13, no. 3, pp. 298-316, 1983.

APPENDIX A. KINEMATIC DESCRIPTION OF MANIPULATOR

The study of kinematics provides information on the overall geometrical configuration of the robotic mechanism. The positions and orientations between the links represent a convenient means for describing the overall positions and orientations of the manipulator. Provided the angle or displacement of each joint, the configuration of the robot can be calculated through transformation between each joint and expressed in terms of joint variables. Given the desired location in Cartesian space for the end effector of the robot, the required angle or displacement of each joint can be computed through the inverse transformation and expressed in terms of the Cartesian description. The calculated value of each joint is used to create the manipulator's motion and control the actuator connected to each joint for the trajectory of the end effector.

A robotic manipulator is a series of links connected through joints, which form an open loop kinematic chain. There are two types of joints commonly used in robotic manipulators: revolute (rotary) joints, and prismatic (sliding) joints which provide one degree of rotation and translation, respectively. Motion of each joint is produced independently by the joint actuator. The link connected by the joints represents a relative relationship between the joints at its ends. Generally, each joint axis represents one degree of freedom (DOF) so that the total number of DOFs of the robotic mechanism is equal to the number of joint axes through which motion can occur. Figure A.1 shows the numbering of the n -links and joints of the open loop kinematic chain. Joints would be either revolute or prismatic. The links are numbered

sequentially starting from the base side (link 0) to the last (link n). The joints are numbered $1, \dots, n$, so that the joint i connects the links $i-1$ and i . Link 0 is connected to link 1 by joint 1. No joint is specified at the end of the last link n .

Any link of the robot can be characterized kinematically by four link parameters. The assignment of the coordinate frames of the links in the manipulator is described by the notation developed by Denavit and Hartenberg. In the kinematic analysis of the soil sampling manipulator, Craig convention [8] is used for numbering the coordinates frames. Figure A.2 shows the link parameters and the assignment of coordinate frames $\{i-1\}$ and $\{i\}$ for a general link $i-1$. The size and shape of the link i is described by two variables: the link length a_i and twist angle α_i .

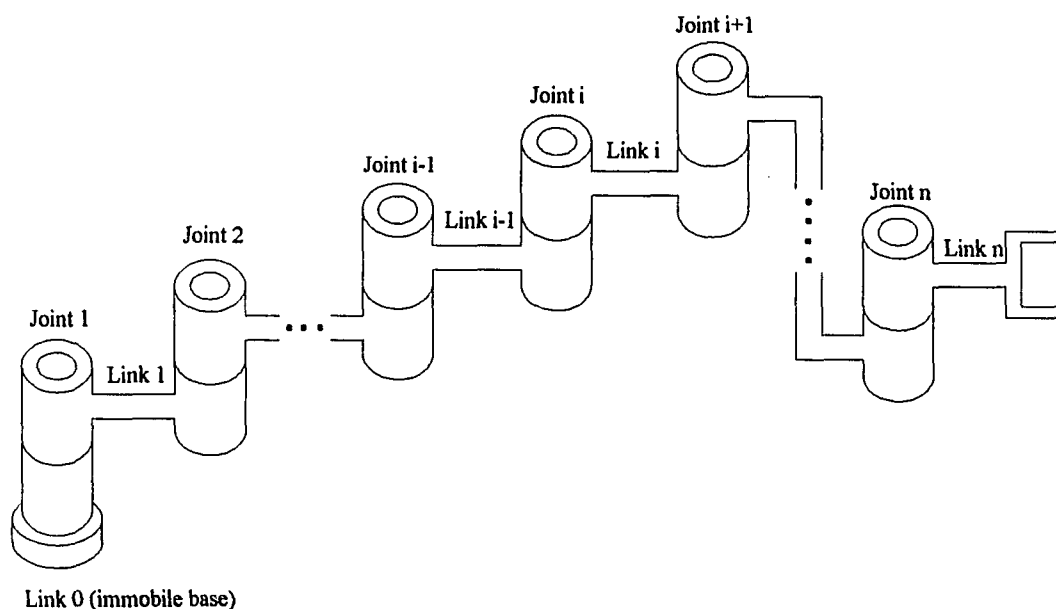


Figure A.1: Numbering of links and joints for n -link manipulator

The relative positional relation of the links $i-1$ and i at joint i is described by two variables called the joint variables: the link offset d_i for the prismatic joints and joint angle θ_i for the revolute joints. The geometric configuration of robot motion can be described by assigning a Cartesian (rectangular right-handed) coordinate system to each link (joint) in a n links manipulator connected serially by n joints. The Z axis, denoted Z_i , of the coordinate frame $\{i\}$ of the link i is aligned with the joint axis i . The X axis of the frame $\{i\}$, X_i , is selected so that it points along a_i in the direction from joint i to joint $i+1$. The direction of Y axis, Y_i , is found by the right-hand rule. According to Denavit-Hartenberg notation, the four link parameters described above are expressed as follows: link length a_i = the distance measured along the X_i axis from Z_i to Z_{i+1} , twist angle α_i = the angle between Z_i and Z_{i+1} measured about the X_i axis, link offset d_i = the distance measured along the Z_i axis from X_{i-1} to X_i , and joint angle θ_i = the angle between X_{i-1} and X_i measured about the Z_i axis.

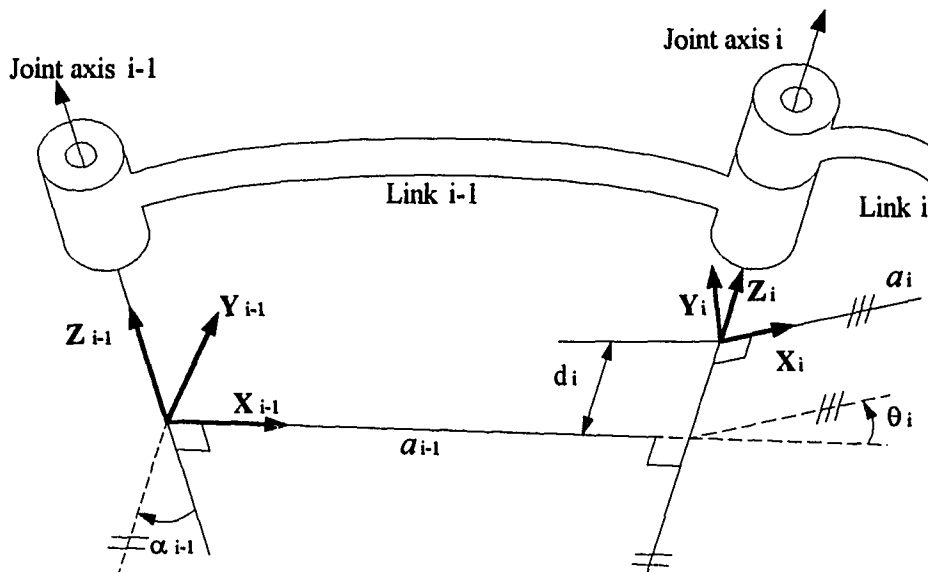


Figure A.2: Link parameters and coordinate frames for link with revolute joints

The homogeneous transformation represents the relation between the neighboring coordinate frames. The 4 x 4 homogeneous transformation matrix ${}^{i-1}T$ that describes the rotation and position of the coordinate frame $\{i\}$ relative to the coordinate frame $\{i-1\}$ is

$${}^{i-1}T = Trans(X_{i-1}, a_{i-1})Rot(X_{i-1}, \alpha_{i-1})Trans(Z_i, d_i)Rot(Z_i, \theta_i) \quad (A.1)$$

where $Trans(X_{i-1}, a_{i-1})$ denotes a translation of the origin of frame $\{i-1\}$ along X_{i-1} axis for a distance a_{i-1} , $Rot(X_{i-1}, \alpha_{i-1})$ denotes a rotation of the origin of frame $\{i-1\}$ about X_{i-1} axis for a angle α_{i-1} , $Trans(Z_i, d_i)$ denotes a translation of the origin of frame $\{i\}$ along X_{i-1} axis for a distance a_{i-1} , and $Rot(Z_i, \theta_i)$ denotes a rotation of the origin of frame $\{i\}$ about Z_i axis for a angle θ_i . Multiplying the right-hand side of equation 1, we obtain

$${}^{i-1}T = \begin{pmatrix} \cos \theta_i & -\sin \theta_i & 0 & a_{i-1} \\ \cos \alpha_{i-1} \sin \theta_i & \cos \alpha_{i-1} \cos \theta_i & -\sin \alpha_{i-1} & -\sin \alpha_{i-1} d_i \\ \sin \alpha_{i-1} \sin \theta_i & \sin \alpha_{i-1} \cos \theta_i & \cos \alpha_{i-1} & \cos \alpha_{i-1} d_i \\ 0 & 0 & 0 & 1 \end{pmatrix} \quad (A.2)$$

The equation above can be rewritten in the form of

$${}^{i-1}T = \begin{bmatrix} {}^{i-1}R & {}^{i-1}P \\ \mathbf{0} & \mathbf{1} \end{bmatrix} \quad (A.3)$$

where ${}^{i-1}R$ is the 3 x 3 rotation matrix that describes the rotation of the origin of frame $\{i\}$ relative to frame $\{i-1\}$, ${}^{i-1}P$ is the 3 x 1 position vector that represents the origin of frame $\{i\}$ relative to frame $\{i-1\}$, " $\mathbf{0}$ " is the 1 x 3 perspective transformation with the entries of "0", and " $\mathbf{1}$ " is the 1 x 1 scaling factor with the entry of '1'. The homogeneous transformation

that describes the Cartesian orientation and position of the end frame $\{n\}$ with respect to the base frame $\{0\}$ attached to the base of robot can be expressed in the form of

$${}^0T_n = {}^0T_1 {}^1T_2 \dots {}^{n-1}T_n \quad (\text{A.4})$$

Given the values of all link parameters, this transformation 0T_n is a function of all n joint variables only.

APPENDIX B. DERIVATION OF DYNAMIC MODEL BASED ON NEWTON-EULER FORMULATION

The Newton-Euler formulation is based on the balance of the forces and the torques acting between the links. The Newton-Euler formulation describes the dynamic characteristics of one link in the form of a set of differential equations relative to the neighboring links in a serial link robotic arm.

B.1 Recursive Newton-Euler formulation

The velocities and accelerations of the links are iteratively computed in the forward direction from link 1 to link n . The general force (torque) relations are determined recursively in the backward direction from link n to 1. The derivation of dynamics equations for a serial link n -joint manipulator is summarized in the following [8].

1. Recursive forward relations of link i (iteration, $i:1 \rightarrow n$)

a. Velocity and acceleration of the i th link

$${}^i\omega_i = {}_{i-1}^iR {}^{i-1}\omega_{i-1} + \dot{\theta}_i {}^i\hat{Z}_i \quad \text{if R} \tag{B.1}$$

$${}^i\omega_i = {}_{i-1}^iR {}^{i-1}\omega_{i-1} \quad \text{if P}$$

$${}^i\alpha_i = {}_{i-1}^iR {}^{i-1}\alpha_{i-1} + {}_{i-1}^iR {}^{i-1}\omega_{i-1} \times \dot{\theta}_i {}^i\hat{Z}_i + \ddot{\theta}_i {}^i\hat{Z}_i \quad \text{if R} \tag{B.2}$$

$${}^i\alpha_i = {}_{i-1}^iR {}^{i-1}\alpha_{i-1} \quad \text{if P}$$

$$\begin{aligned}
{}^i a_i &= {}_{i-1}^i R ({}^{i-1} \alpha_{i-1} \times {}^{i-1} P_i + {}^{i-1} \omega_{i-1} \times ({}^{i-1} \omega_{i-1} \times {}^{i-1} P_i) + {}^{i-1} a_{i-1}) & \text{if R} \\
{}^i a_i &= {}_{i-1}^i R ({}^{i-1} \alpha_{i-1} \times {}^{i-1} P_i + {}^{i-1} \omega_{i-1} \times ({}^{i-1} \omega_{i-1} \times {}^{i-1} P_i) + {}^{i-1} a_{i-1}) & \text{if P} \\
&+ 2 {}^i \omega_i \times \dot{d}_i {}^i \hat{Z}_i + \ddot{d}_i {}^i \hat{Z}_i
\end{aligned} \tag{B.3}$$

$${}^i a_{c,i} = {}^i \alpha_i \times {}^i P_{c,i} + {}^i \omega_i \times ({}^i \omega_i \times {}^i P_{c,i}) + {}^i a_i \tag{B.4}$$

b. Force and torque acting at the center of mass for the i th link

$${}^i F_i = m_i {}^i a_{c,i} \tag{B.5}$$

$${}^i N_i = {}^i I_{c,i} {}^i \alpha_i + {}^i \omega_i \times {}^i I_{c,i} {}^i \omega_i \tag{B.6}$$

2. Recursive backward relations of link i (iteration, $i:n \rightarrow 1$)

a. Force and torque (moment) relations for the i th link

$${}^i f_i = {}_{i+1}^i R {}^{i+1} f_{i+1} + {}^i F_i \tag{B.7}$$

$${}^i n_i = {}^i N_i + {}_{i+1}^i R {}^{i+1} n_{i+1} + {}^i P_{c,i} \times {}^i F_i + {}^i P_{i+1} \times {}_{i+1}^i R {}^{i+1} f_{i+1} \tag{B.8}$$

b. Torque (force) produced by the actuator at the joint i

$$\tau_i = {}^i n_i^T {}^i \hat{Z}_i \quad \text{if R} \tag{B.9}$$

$$\tau_i = {}^i f_i^T {}^i \hat{Z}_i \quad \text{if P}$$

In the derivation of the manipulator dynamics equations,

i denotes the number of the i th link joint of the manipulator,

${}^{i-1} P_i$ is the position vector locating the origin of frame $\{i\}$ with respect to frame $\{i-1\}$,

${}^i P_{c,i}$ is the position vector locating the center of mass for link i relative to frame $\{i\}$,

${}^i_{i+1}R$ is the rotation matrix describing frame $\{i+1\}$ with respect to frame $\{i\}$,

${}^i\omega_i$ is the angular velocity of link i written in frame $\{i\}$,

${}^i\alpha_i$ is the angular acceleration of link i written in frame $\{i\}$,

${}^i a_i$ is the linear acceleration of frame $\{i\}$,

${}^i a_{c,i}$ is the linear acceleration of the center of mass for link i written in frame $\{i\}$,

$\dot{\theta}_i$ and $\ddot{\theta}_i$ are the rotational velocity and acceleration of joint i , respectively,

\dot{d}_i and \ddot{d}_i are the translational velocity and acceleration of joint i , respectively,

m_i is the total mass of link i ,

${}^i F_i$ is the force acting at the center of mass for link i ,

${}^i N_i$ is the torque (moment) acting at the center of mass for link i ,

${}^i f_i$ is the force exerted by link $i-1$ on link i ,

${}^i n_i$ is the torque (moment) exerted by link $i-1$ on link i ,

${}^i I_{c,i}$ is the second inertial moment of link i about the center of mass and described in terms of frame $\{c_i\}$ which has same orientation as frame $\{i\}$,

τ_i is the joint driving torque (force) at joint i ,

${}^i \hat{Z}_i$ is the unit vector in Z-direction of frame $\{i\}$ (${}^i \hat{Z}_i = [0 \ 0 \ 1]^T$),

R and P denote the revolute and prismatic joints of the arm, respectively.

The position, velocity, and acceleration of link i ($i = 1, \dots, n$) in the forward iterations are computed by setting the initial conditions (${}^0\omega_0 = {}^0\alpha_0 = 0$, and ${}^0v_0 = {}^0a_0 = 0$) for the base frame $\{0\}$. If the effect of gravity on the links is considered, we only have to set ${}^0a_0 = -\hat{g} = -[g_x \ g_y \ g_z]^T$. The joint driving torque for link i ($i = n, n-1, \dots, 1$) in the backward iterations is computed by knowing the contact force ${}^{n+1}f_{n+1}$ and torque ${}^{n+1}n_{n+1}$ exerted by the environment on the end-effector.

B.2 Dynamic model of remote robot manipulator

The remote robot manipulator located on the trailer for soil sampling consists of three joints and four links (prismatic-revolute-revolute joints in sequence). The soil sampler (a total mass of 50 lbs) as the end-effector is rigidly mounted to the end of the last link. With the assumption that the three-axis remote manipulator is a jointed rigid body, the dynamic model for the motion is developed systematically using the Newton-Euler formulation described in Appendix B.1.

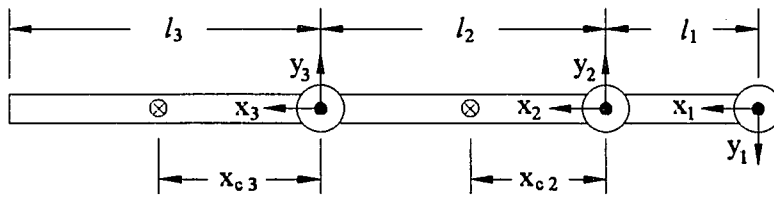
The link parameters and the link coordinate frame assignments are described by Denavit-Hartenberg notation in Appendix A. Figure B.2.1 shows the schematic view of the remote manipulator. From the homogeneous transformation matrices associated with the coordinates frames we have

$${}^0R_1 = \begin{bmatrix} 1 & 0 & 0 \\ 0 & 1 & 0 \\ 0 & 0 & 1 \end{bmatrix}, {}^1R_2 = \begin{bmatrix} C_2 & -S_2 & 0 \\ -S_2 & -C_2 & 0 \\ 0 & 0 & -1 \end{bmatrix}, {}^2R_3 = \begin{bmatrix} C_3 & -S_3 & 0 \\ S_3 & C_3 & 0 \\ 0 & 0 & 1 \end{bmatrix} \quad (\text{B.10})$$

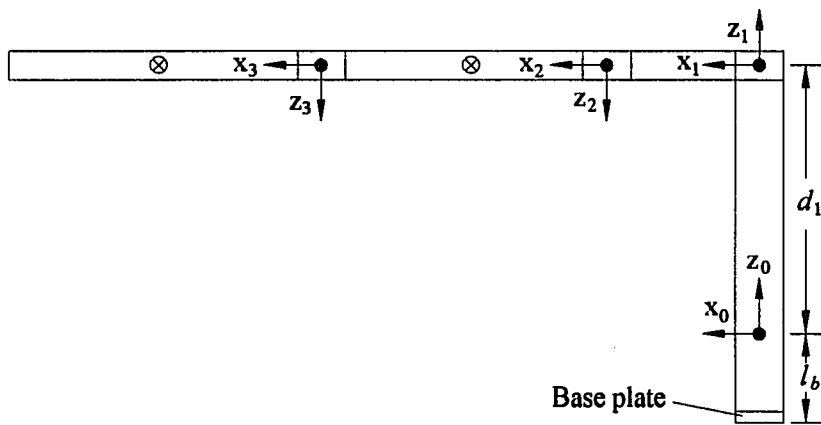
$${}^0P_1 = \begin{bmatrix} 0 \\ 0 \\ d_1 \end{bmatrix}, {}^1P_2 = \begin{bmatrix} l_1 \\ 0 \\ 0 \end{bmatrix}, {}^2P_3 = \begin{bmatrix} l_2 \\ 0 \\ 0 \end{bmatrix}, {}^3P_e = \begin{bmatrix} l_3 \\ 0 \\ l_4 \end{bmatrix} \quad (\text{B.11})$$

$${}^iP_{c,i} = \begin{bmatrix} x_{ci} \\ y_{ci} \\ z_{ci} \end{bmatrix}, \quad i = 1, 2, 3 \quad (\text{B.12})$$

$${}^iI_{c,i} = \begin{bmatrix} I_{i,11} & I_{i,12} & I_{i,13} \\ I_{i,21} & I_{i,22} & I_{i,23} \\ I_{i,31} & I_{i,32} & I_{i,33} \end{bmatrix}, \quad i = 1, 2, 3 \quad (\text{B.13})$$



a) Top view



b) Side view

Figure B.1: Schematic of the manipulator located on the trailer

For the forward iterations ($i = 1, 2, 3$) considering the effect of gravity on the links, the initial conditions are

$${}^0\omega_0 = {}^0\alpha_0 = \mathbf{0}, \quad {}^0a_0 = -[0 \ 0 \ -g]^T \quad (\text{B.14})$$

For the case in which the manipulator is moving in free space, the starting conditions for the backward iterations ($i = 3, 2, 1$) are that the force and couple applied at the end effector are zero. From equations B.1 through B.6 for the link 1 we obtain

$${}^1F_1 = \begin{bmatrix} 0 \\ 0 \\ m_1g + m_1\ddot{d}_1 \end{bmatrix}, \quad {}^1N_1 = \mathbf{0} \quad (\text{B.15})$$

For the links 2 and 3 we obtain

$${}^2F_2 = \begin{bmatrix} -m_2 y_{c2} \ddot{\theta}_2 - m_2 x_{c2} \dot{\theta}_2^2 \\ m_2 x_{c2} \ddot{\theta}_2 - m_2 y_{c2} \dot{\theta}_2^2 \\ -m_2 \ddot{d}_1 - m_2 g \end{bmatrix}, \quad {}^2N_2 = \begin{bmatrix} I_{2,13} \ddot{\theta}_2 - I_{2,23} \dot{\theta}_2^2 \\ I_{2,23} \ddot{\theta}_2 + I_{2,13} \dot{\theta}_2^2 \\ I_{2,33} \ddot{\theta}_2 \end{bmatrix} \quad (\text{B.16})$$

$${}^3F_3 = \begin{bmatrix} m_3(l_2S_3 - y_{c3})\ddot{\theta}_2 - m_3y_{c3}\ddot{\theta}_3 + m_3(-x_{c3} - l_2C_3)\dot{\theta}_2^2 - m_3x_{c3}\dot{\theta}_3^2 - 2m_3x_{c3}\dot{\theta}_2\dot{\theta}_3 \\ m_3(l_2C_3 + x_{c3})\ddot{\theta}_2 + m_3x_{c3}\ddot{\theta}_3 + m_3(-y_{c3} + l_2S_3)\dot{\theta}_2^2 - m_3y_{c3}\dot{\theta}_3^2 - 2m_3y_{c3}\dot{\theta}_2\dot{\theta}_3 \\ -m_3\ddot{d}_1 - m_3g \end{bmatrix} \quad (\text{B.17})$$

$${}^3N_3 = \begin{bmatrix} I_{3,13}(\ddot{\theta}_2 + \ddot{\theta}_3) - I_{3,23}(\dot{\theta}_2 + \dot{\theta}_3)^2 \\ I_{3,23}(\ddot{\theta}_2 + \ddot{\theta}_3) + I_{3,13}(\dot{\theta}_2 + \dot{\theta}_3)^2 \\ I_{3,33}(\ddot{\theta}_2 + \ddot{\theta}_3) \end{bmatrix} \quad (\text{B.18})$$

From equations B.7 and B.8 for the backward iterations, we obtain

$${}^3f_3 = \begin{bmatrix} F_{31} \\ F_{32} \\ F_{33} \end{bmatrix}, \quad {}^3n_3 = \begin{bmatrix} N_{31} - z_{c3}F_{32} + y_{c3}F_{33} \\ N_{32} + z_{c3}F_{31} - x_{c3}F_{33} \\ N_{33} - y_{c3}F_{31} + x_{c3}F_{32} \end{bmatrix} \quad (\text{B.19})$$

$${}^2f_2 = \begin{bmatrix} F_{21} + C_3F_{31} - S_3F_{32} \\ F_{22} + S_3F_{31} + C_3F_{32} \\ F_{23} + F_{33} \end{bmatrix}, \quad (B.20)$$

$${}^2n_2 = \begin{bmatrix} N_{21} + C_3n_{31} - S_3n_{32} - z_{c2}F_{22} + y_{c2}F_{23} \\ N_{22} + S_3n_{31} + C_3n_{32} - l_2F_{33} + z_{c2}F_{21} - x_{c2}F_{23} \\ N_{23} + n_{33} - y_{c2}F_{21} + x_{c2}F_{22} + l_2(S_3F_{31} + C_3F_{32}) \end{bmatrix}$$

$${}^1f_1 = \begin{bmatrix} C_2f_{21} - S_2f_{22} \\ -S_2f_{21} - C_2f_{22} \\ (m_1 + m_2 + m_3)\ddot{d}_1 + (m_1 + m_2 + m_3)g \end{bmatrix} \quad (B.21)$$

where

$F_{i1}, F_{i2},$ and F_{i3} are the elements of iF_i for link i ,

$N_{i1}, N_{i2},$ and N_{i3} are the elements of iN_i for link i ,

$n_{21}, n_{22},$ and n_{23} are the elements of 2n_2 ,

$n_{31}, n_{32},$ and n_{33} are the elements of 3n_3 ,

$f_{21}, f_{22},$ and f_{23} are the elements of 2f_2 .

From equation B.9 the joint driving torques or forces are given by

$$\tau_1 = (m_1 + m_2 + m_3)\ddot{d}_1 + (m_1 + m_2 + m_3)g \quad (B.22)$$

$$\begin{aligned} \tau_2 = & [m_2(x_{c2}^2 + y_{c2}^2) + m_3(x_{c3}^2 + 2l_2x_{c3}C_3 - 2l_2y_{c3}S_3 + y_{c3}^2 + l_2^2) + I_{2,33} + I_{3,33}]\ddot{\theta}_2 \\ & + [m_3(x_{c3}^2 + l_2x_{c3}C_3 - l_2y_{c3}S_3 + y_{c3}^2) + I_{3,33}]\ddot{\theta}_3 - 2m_3l_2[x_{c3}S_3 + y_{c3}C_3]\dot{\theta}_2\dot{\theta}_3 \quad (B.23) \\ & - m_3l_2[x_{c3}S_3 + y_{c3}C_3]\dot{\theta}_3^2 \end{aligned}$$

$$\begin{aligned} \tau_3 = & [m_3(x_{c3}^2 + l_2x_{c3}C_3 - l_2y_{c3}S_3 + y_{c3}^2) + I_{3,33}]\ddot{\theta}_2 + [m_3(x_{c3}^2 + y_{c3}^2) + I_{3,33}]\ddot{\theta}_3 \\ & + m_3l_2[x_{c3}S_3 + y_{c3}C_3]\dot{\theta}_2^2 \quad (B.24) \end{aligned}$$

APPENDIX C. DERIVATION OF DYNAMIC MODEL BASED ON LAGRANGIAN FORMULATION

The dynamic equations of a n -link manipulator can be determined by first developing the expressions for the kinetic and potential energy for the Lagrangian function. Lagrange's equation of motion can then be formed to describe the dynamics of the manipulator.

The total kinetic energy K of the manipulator is obtained by first determining the kinetic energy of the i th link, K_i , and then summing the kinetic energy of all links. The total kinetic energy associated with n links can be expressed as

$$\begin{aligned}
 K &= \sum_{i=1}^n K_i \\
 &= \frac{1}{2} \sum_{i=1}^n [m_i {}^0v_{c,i}^T {}^0v_{c,i} + {}^i\omega_i^T {}^iI_{c,i} {}^i\omega_i]
 \end{aligned} \tag{C.1}$$

where ${}^0v_{c,i}$ is the linear velocity of the center of mass for link i with respect to frame $\{0\}$.

Similarly, the total potential energy associated with n links can be expressed as

$$\begin{aligned}
 V &= \sum_{i=1}^n V_i \\
 &= - \sum_{i=1}^n m_i {}^0g^T {}^0P_{c,i}
 \end{aligned} \tag{C.2}$$

where the gravitational vector, ${}^0g = [g_x \ g_y \ g_z]^T$.

The Lagrangian function L can be defined as

$$L(q, \dot{q}) = K(q, \dot{q}) - V(q) \quad (C.3)$$

where the generalized coordinate $q(t)$ chosen to describe the manipulator with n joints is $q(t) = [q_1(t) \ q_2(t) \ \cdots \ q_n(t)]$. Lagrange's equations of motion for the manipulator are given by

$$\tau_i = \frac{d}{dt} \left[\frac{\partial L(q, \dot{q})}{\partial \dot{q}_i} \right] - \frac{\partial L(q, \dot{q})}{\partial q_i} \quad (C.4)$$

where $i = 1, 2, \dots, n$, and τ_i is the actuator torque at joint i . From equations (C.3) and (C.4), we have the convenient alternative form:

$$\tau_i = \frac{d}{dt} \left[\frac{\partial K(q, \dot{q})}{\partial \dot{q}_i} \right] - \frac{\partial K(q, \dot{q})}{\partial q_i} + \frac{\partial V(q)}{\partial q_i} \quad (C.5)$$

From the homogeneous transformation matrices associated with the coordinate frames for the remote manipulator located on the trailer we have

$${}^0P_{c,1} = \begin{bmatrix} x_{c1} \\ y_{c1} \\ z_{c1} + d_1 \end{bmatrix}, {}^0P_{c,2} = \begin{bmatrix} x_{c2}C_2 - y_{c2}S_2 + l_1 \\ -x_{c2}S_2 - y_{c2}C_2 \\ -z_{c2} + d_1 \end{bmatrix}, {}^0P_{c,3} = \begin{bmatrix} x_{c3}C_{23} - y_{c3}S_{23} + l_2C_2 + l_1 \\ -x_{c3}S_{23} - y_{c3}C_{23} - l_2S_2 \\ -z_{c3} + d_1 \end{bmatrix} \quad (C.6)$$

The effect of gravity on the links is considered as ${}^0g = [0 \ 0 \ -g]^T$. The generalized coordinates for the sampling manipulator are $q_1 = d_1$, $q_2 = \theta_2$, and $q_3 = \theta_3$. The kinetic energy expressions for the links 1, 2, and 3, respectively, obtained from equation (C.1) are

$$K_1 = \frac{1}{2} m_1 \dot{d}_1^2 \quad (C.7)$$

$$K_2 = \frac{1}{2} m_2 \dot{d}_1^2 + \frac{1}{2} [m_2 (x_{c2}^2 + y_{c2}^2) + I_{2,33}] \dot{\theta}_2^2 \quad (C.8)$$

$$\begin{aligned}
K_3 = & \frac{1}{2} m_3 \dot{d}_1^2 + \frac{1}{2} [m_3 (x_{c3}^2 + y_{c3}^2 + l_2^2 - 2l_2 y_{c3} S_3 + 2l_2 x_{c3} C_3) + I_{3,33}] \dot{\theta}_2^2 \\
& + \frac{1}{2} [m_3 (x_{c3}^2 + y_{c3}^2) + I_{3,33}] \dot{\theta}_3^2 + [x_{c3}^2 + y_{c3}^2 + l_2 x_{c3} C_3 - l_2 y_{c3} S_3 + I_{3,33}] \dot{\theta}_2 \dot{\theta}_3
\end{aligned} \tag{C.9}$$

The potential energy expressions for the links 1,2, and 3, respectively, from equation (C.2) are

$$V_1 = m_1 g d_1 + m_1 z_{c1} g \tag{C.10}$$

$$V_2 = m_2 g d_1 - m_2 z_{c2} g \tag{C.11}$$

$$V_3 = m_3 g d_1 - m_3 z_{c3} g \tag{C.12}$$

Calculating the total kinetic energy, $K = K_1 + K_2 + K_3$, and the total potential energy, $V = V_1 + V_2 + V_3$, and taking their partial derivatives yields

$$\frac{\partial K}{\partial \dot{d}_1} = [m_1 + m_2 + m_3] \dot{d}_1 \tag{C.13}$$

$$\begin{aligned}
\frac{\partial K}{\partial \dot{\theta}_2} = & [m_2 (x_{c2}^2 + y_{c2}^2) + m_3 (x_{c3}^2 + y_{c3}^2 + l_2^2 2l_2 x_{c3} S_3 - 2l_2 y_{c3} C_3) + I_{2,33} + I_{3,33}] \dot{\theta}_2 \\
& + [m_3 (x_{c3}^2 + y_{c3}^2 + l_2 x_{c3} C_3 - l_2 y_{c3} S_3) + I_{3,33}] \dot{\theta}_3
\end{aligned} \tag{C.14}$$

$$\frac{\partial K}{\partial \dot{\theta}_3} = [m_3 (x_{c3}^2 + y_{c3}^2 + l_2 x_{c3} C_3 - l_2 y_{c3} S_3) + I_{3,33}] \dot{\theta}_2 + [m_3 (x_{c3}^2 + y_{c3}^2) + I_{3,33}] \dot{\theta}_3 \tag{C.15}$$

$$\frac{\partial K}{\partial d_1} = 0, \quad \frac{\partial K}{\partial \theta_2} = 0, \quad \frac{\partial K}{\partial \theta_3} = -m_3 l_2 [x_{c3} S_3 + y_{c3} C_3] \dot{\theta}_2 \dot{\theta}_3 - m_3 l_2 [x_{c3} S_3 + y_{c3} C_3] \dot{\theta}_2^2 \tag{C.16}$$

$$\frac{\partial V}{\partial d_1} = [m_1 + m_2 + m_3] g, \quad \frac{\partial V}{\partial \theta_2} = 0, \quad \frac{\partial V}{\partial \theta_3} = 0 \tag{C.17}$$

Substituting equations (C.13) through (C.17) into (C.5) we obtain the joint driving torques:

$$\tau_1 = (m_1 + m_2 + m_3) \ddot{d}_1 + (m_1 + m_2 + m_3) g \tag{C.18}$$

$$\begin{aligned}
\tau_2 = & [m_2(x_{c2}^2 + y_{c2}^2) + m_3(x_{c3}^2 + 2l_2x_{c3}C_3 - 2l_2y_{c3}S_3 + y_{c3}^2 + l_2^2) + I_{2,33} + I_{3,33}] \ddot{\theta}_2 \\
& + [m_3(x_{c3}^2 + l_2x_{c3}C_3 - l_2y_{c3}S_3 + y_{c3}^2) + I_{3,33}] \ddot{\theta}_3 - 2m_3l_2[x_{c3}S_3 + y_{c3}C_3] \dot{\theta}_2 \dot{\theta}_3 \quad (\text{C.19}) \\
& - m_3l_2[x_{c3}S_3 + y_{c3}C_3] \dot{\theta}_3^2
\end{aligned}$$

$$\begin{aligned}
\tau_3 = & [m_3(x_{c3}^2 + l_2x_{c3}C_3 - l_2y_{c3}S_3 + y_{c3}^2) + I_{3,33}] \ddot{\theta}_2 + [m_3(x_{c3}^2 + y_{c3}^2) + I_{3,33}] \ddot{\theta}_3 \\
& + m_3l_2[x_{c3}S_3 + y_{c3}C_3] \dot{\theta}_2^2 \quad (\text{C.20})
\end{aligned}$$

The equations of motion obtained by the Lagrangian formulation are seen to be in the same form as equations (B.22) through (B.24) given by the Newton-Euler formulation for the three-axis sampling manipulator.

APPENDIX D. DESCRIPTION OF HARDWARE

D.1 Remote-controlled guide vehicle

Table D.1: Linear actuators specifications for the guide vehicle

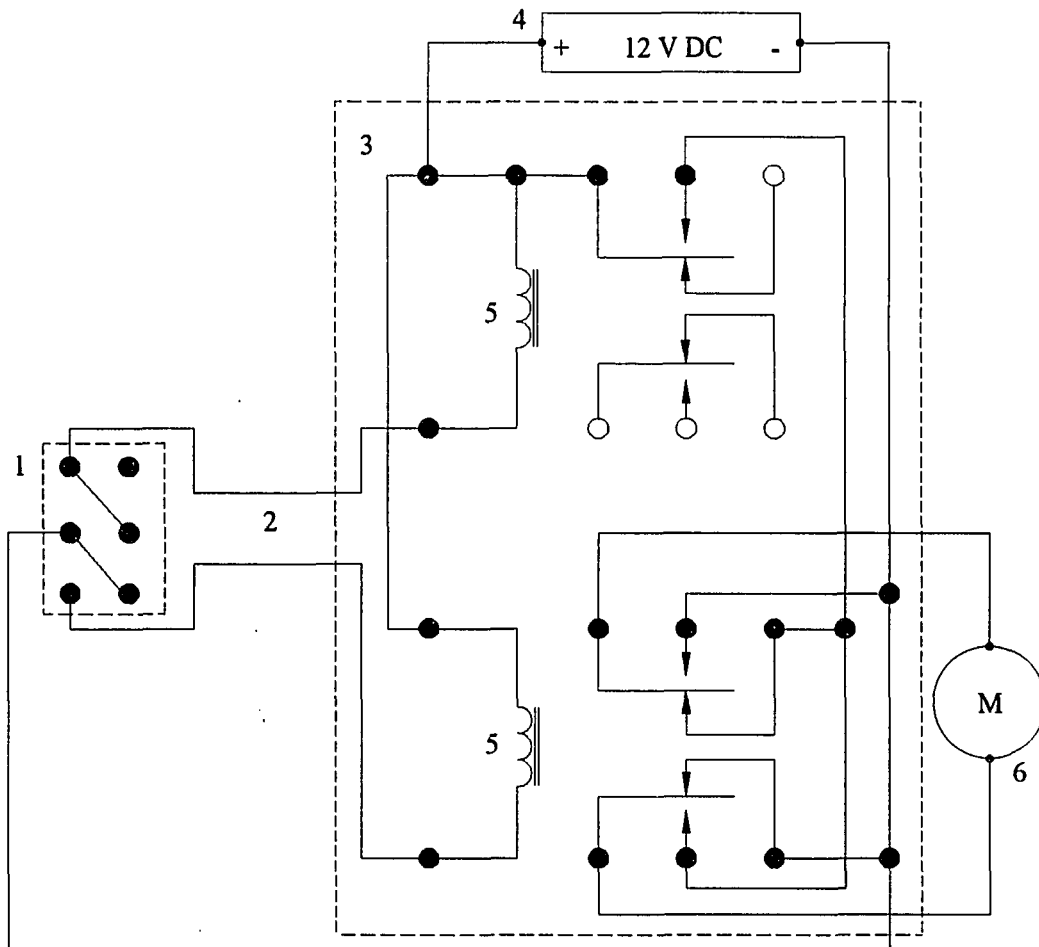
	Transmission	Throttle	Brake	Steering
Model (Ball drive actuator w/ rod end, Motion Systems Corp.)	85151	85151	85257	85199
Dynamic Load capacity (lbs)	500	500	50	1000
Maximum stroke (inch)	6.0	2.0	2.0	14.0
Gear reducer (Worm gear)	Yes	Yes	Yes	Yes
Gear ratio	20:1	20:1	1:1	20:1
Stroke speed (inch/sec.)	.35	.35	7.0	.58
Motor (Permanent Magnet Brush)	12 VDC	12 VDC	12 VDC	12 VDC
Max. operating speed w/ no load (rpm)	3000	3000	3000	3000
Weight of 6 in. stroke (lbs)	6.2	6.2	5.7	8.4
Ball drive (Epicyclic Ball Screw)	Yes	Yes	Yes	Yes

Table D.2: Servo specifications for the guide vehicle

Model	Airtronics 94102	Motor	Standard 3 pole
Servo	Precision heavy duty servo	Weight (oz.)	1.59
Dimensions (inch)	1.54 (L) x .79 (W) x 1.42 (H)	Torque (oz.-in.)	50
Transit time (sec) for 60° rotation	.22	Deadband (μ sec.)	60

*: Servo has injection molded case and vibration isolators.
Same servos are used to remotely control the brake, transmission, throttle, and steering of the vehicle.

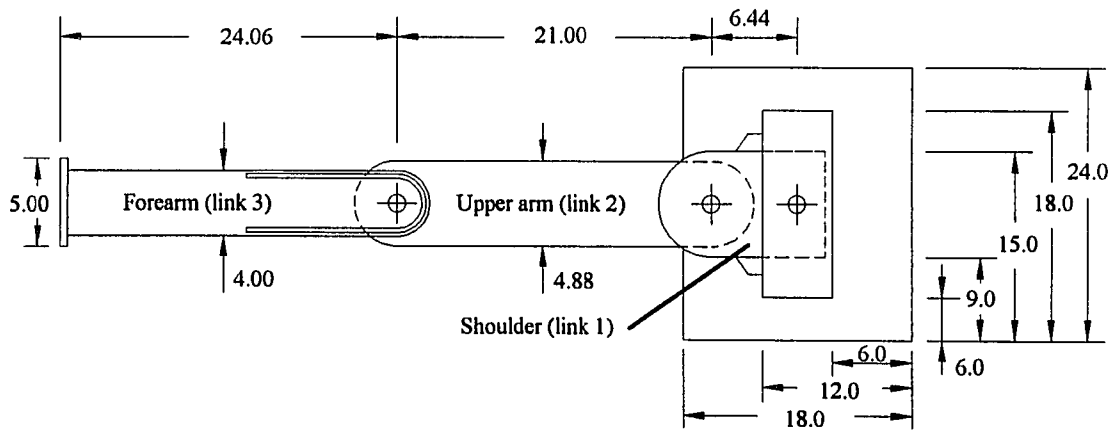
Figure D.1 shows the circuit diagram of switch-relay-linear actuator motor to control the brake, throttle, transmission, and steering system of the vehicle. Two relays and one double pole double throw switch are used to control each linear actuator using a 12 VDC auto battery as a power source. Only one relay is turned on when the switch is activated. Both relays are turned off when the switch is turned off.



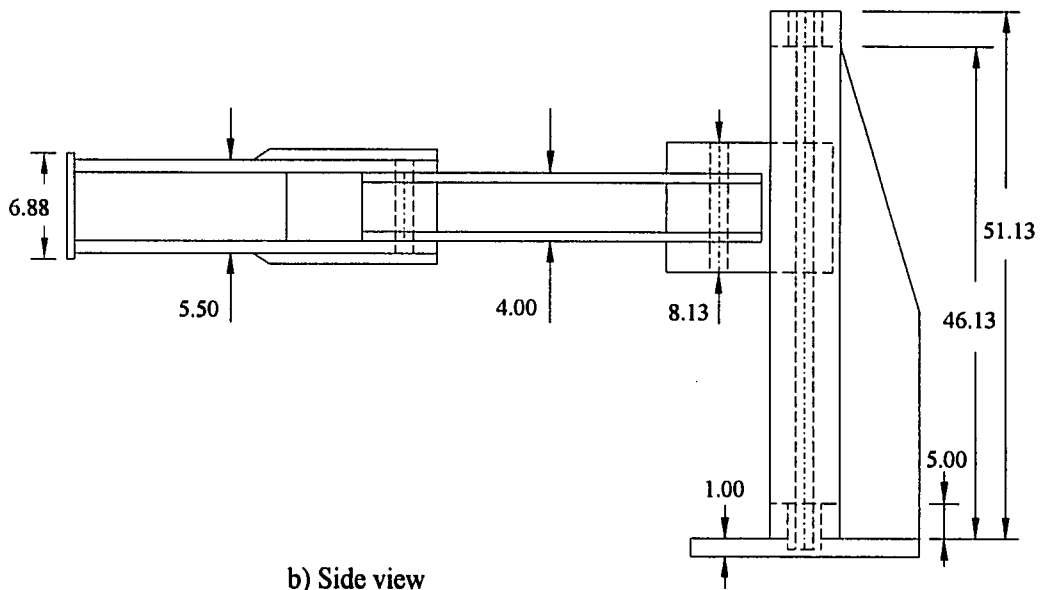
- 1: Double-pole-double-throw switch
 2: 100 ft wires for teleoperated control and 1 ft wire for radio control
 3: Two relays 4: Auto battery 5: Inductor
 6: 12 V DC permanent magnet brush type motor of linear actuator

Figure D.1: Circuit diagram of controlling a motor of linear actuator.

D.2 Remote manipulator located on trailer



a) Top view



b) Side view

Figure D.2: Schematic of links of the manipulator located on the trailer

Table D.3: Motor specifications for the manipulator located on the trailer

Drive joint	Shoulder	Upper arm	Forearm
Model (Electro-Craft)	E-0644	E-0644	E-0642
Continuous stall torque (oz-in)	192	192	94
Peak Torque (oz-in)	960	960	480
Max. terminal voltage (V)	60	60	60
Max. operating speed w/ no load (rpm)	1850	1850	4800
Armature moment of inertia (oz-in-sec ²)	.0368	.0368	.0142
Damping constant (oz-in/krpm)	2.56	2.56	1.6
Torque constant, K_m (oz-in/amp)	43.84	43.84	11.84
Voltage constant, K_b (V/krpm)	32.4	32.4	8.7
Winding resistance, R_a @25C (ohm)	1.5	1.5	.34
Max. pulse current (A)	22	22	40
Weight (lbs)	11.5	11.5	7.5

APPENDIX E. ROBOTIC ARM ON GUIDE VEHICLE

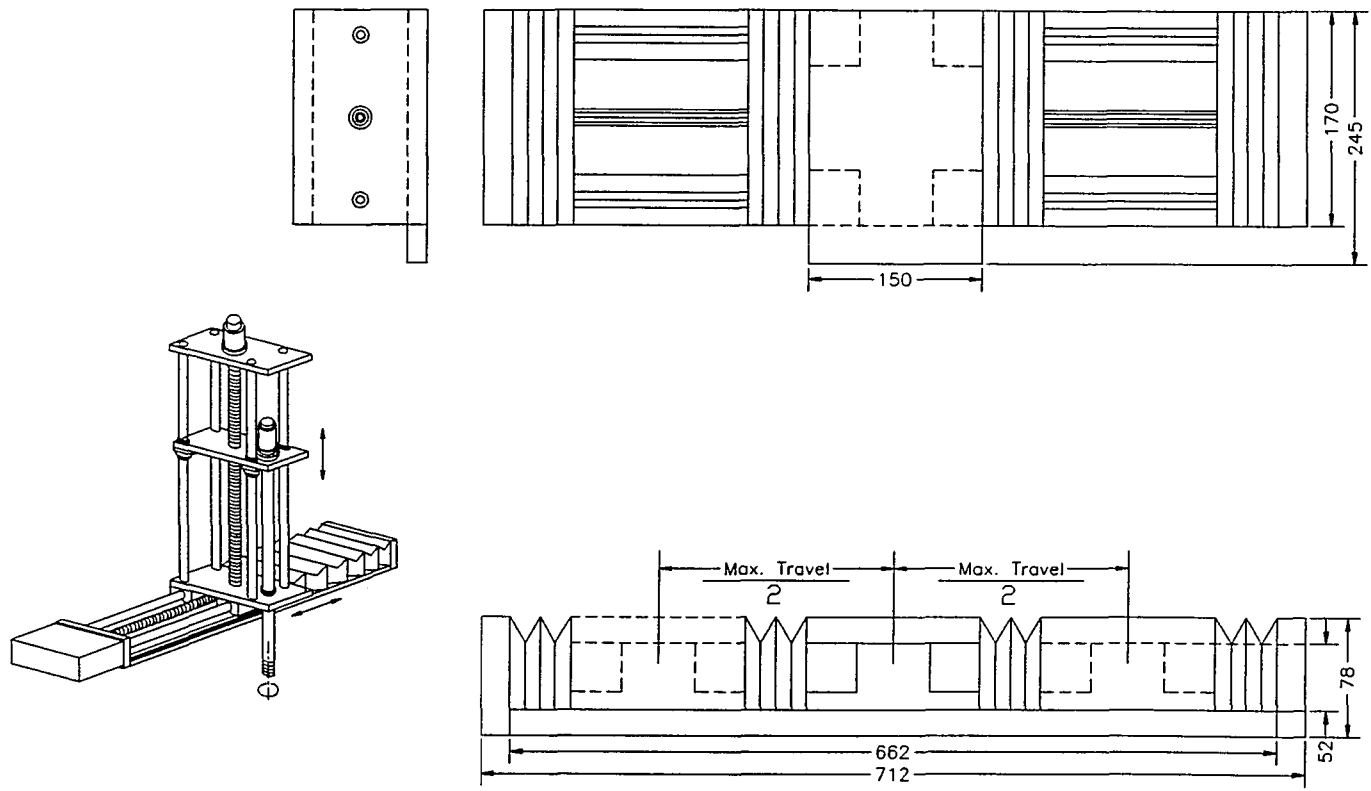


Figure E.1: Horizontal axis of the manipulator on the guide vehicle

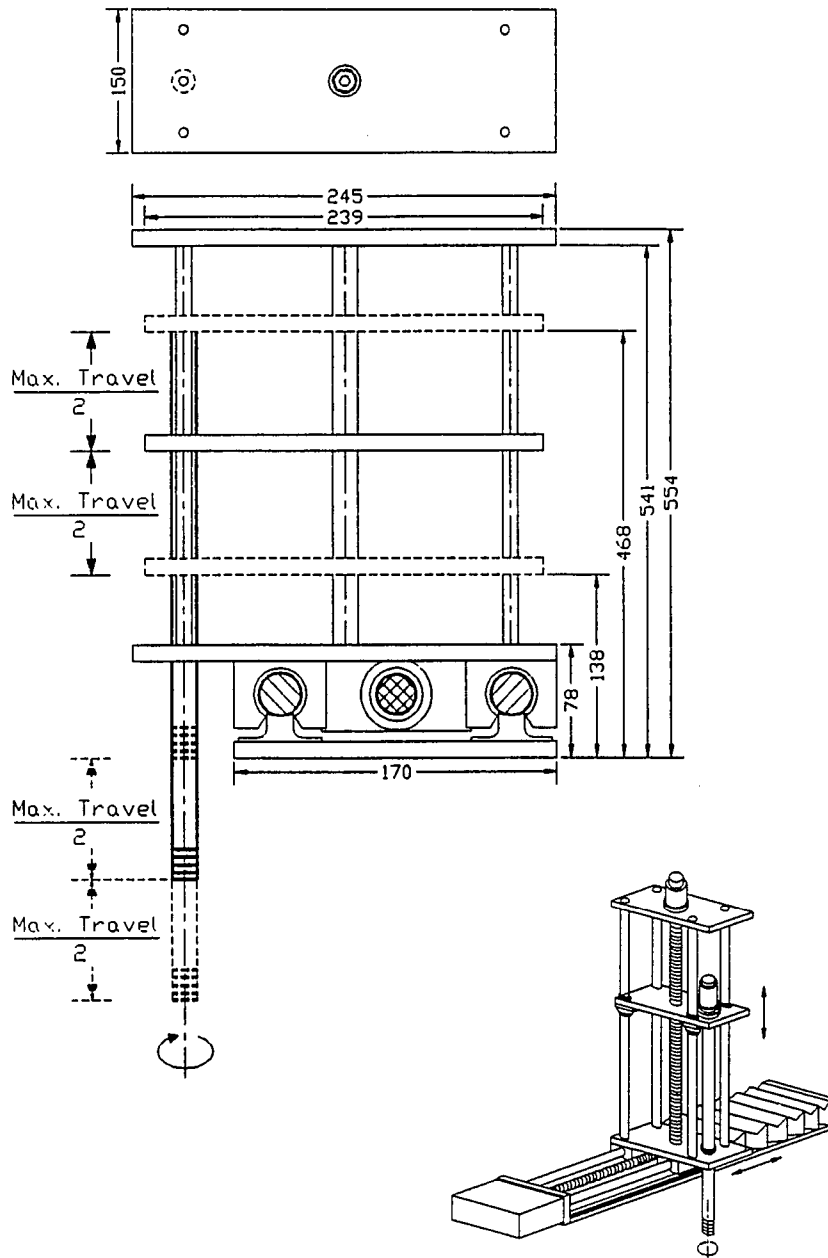


Figure E.2: Vertical and rotational axes of the manipulator on the guide vehicle

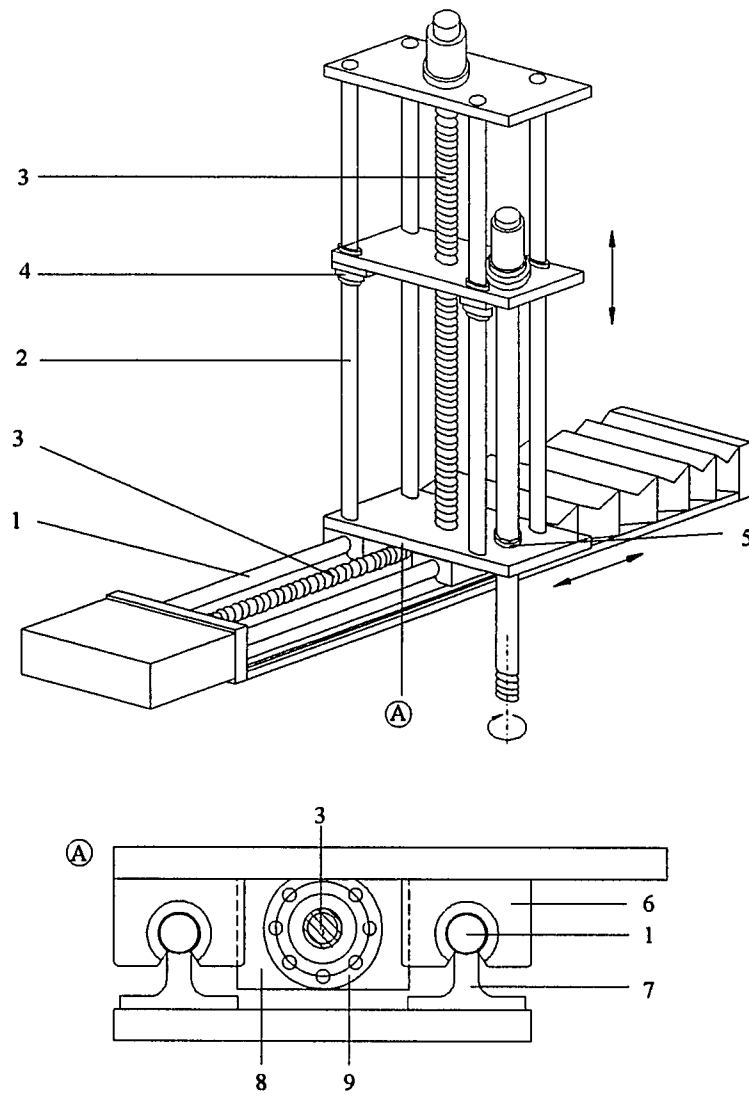
E.2 Mechanical components for motion assembly

Figure E.3: Mechanical components for motion assembly of the manipulator on the guide vehicle

Table E.1: List of mechanical components for the manipulator on the guide vehicle

ITEM	QTY	PART	MODEL	DESCRIPTION
1	2	Solid shaft	16 mm in dia.	692 mm in length
2	4	Solid shaft	12 mm in dia.	476 mm in length
3	1	Ball screw	16 mm in dia.	Precision-rolled thread, lead of 5 mm, 722 mm in length
4	1	Ball screw	16 mm in dia.	Precision - rolled thread, lead of 5 mm, 494 mm in length
5	4	Linear bearing	1801-2 12-00	Flanged linear set with 2 integral seals
6	1	Cylindrical bearing	0663-216-00	Linear bearing for combined linear and rotary motion
7	4	Linear bearing	1038-616-00	Adjustable linear set with 2 seals
8	2	Shaft support rail	1050-716-00	705 mm in length
9	1	Ball nut	1512-0-1055	Adjustable-preload single nut with flange
10	1	Nut housing	1506-0010	Housing for flanged nut
	3	End bearing	1590-1-1000	Screw end for fixed end with angular contact thrust ball bearing
	2	End bearing	1590-6-1000	Screw end for floating-bearing end with deep-groove ball bearing

* Items are numbered in Figure E.1.

* All components are manufactured from STAR LINEAR SYSTEMS.